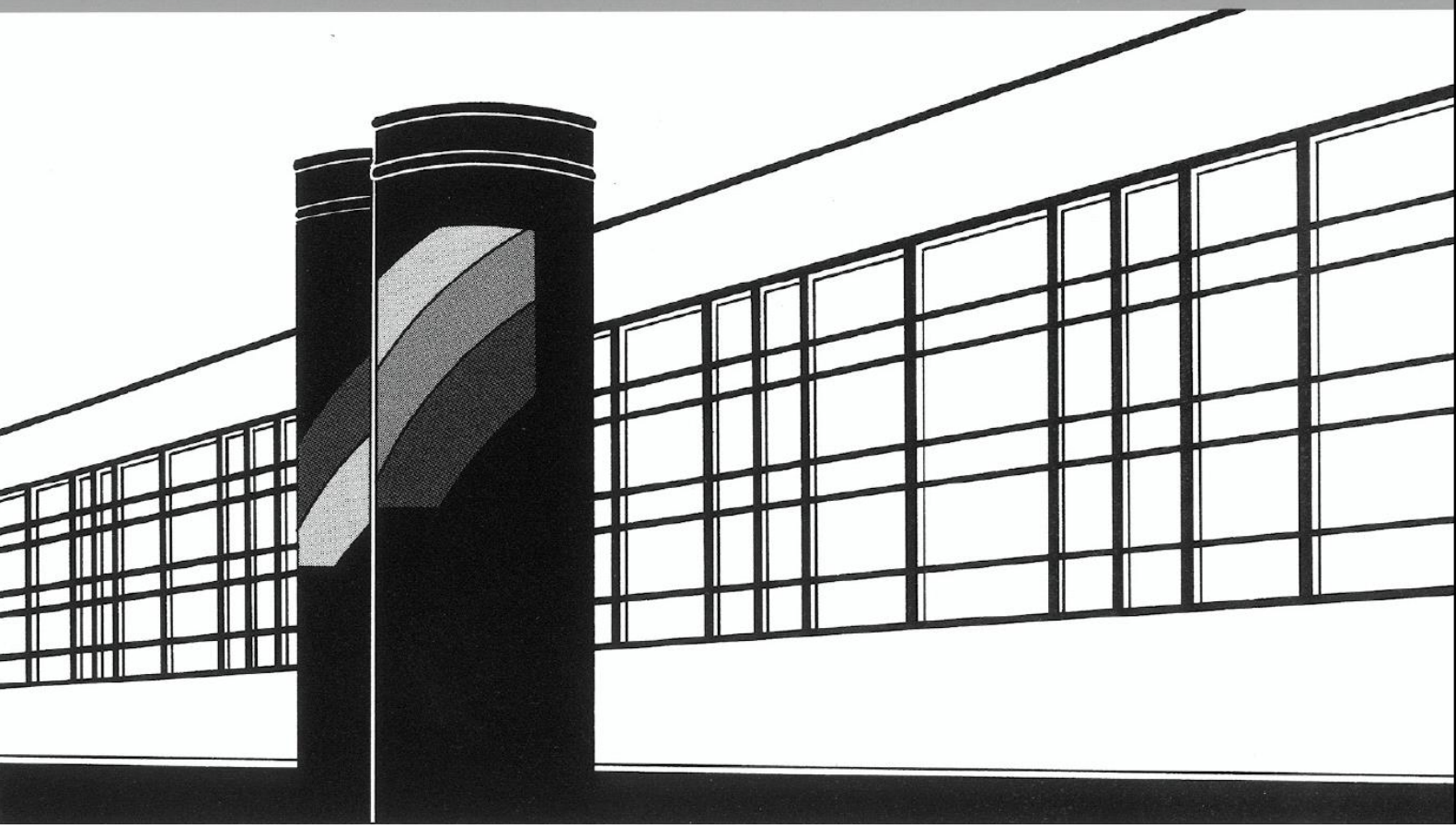


Universität Stuttgart



Institut für Wasser- und Umweltsystemmodellierung

Mitteilungen



Heft 281 Sina Ackermann

A multi-scale approach for drop/porous-
medium interaction

A multi-scale approach for drop/porous-medium interaction

von der Fakultät Bau- und Umweltingenieurwissenschaften der
Universität Stuttgart zur Erlangung der Würde einer
Doktor-Ingenieurin (Dr.-Ing.) genehmigte Abhandlung

vorgelegt von

Sina Ackermann

aus Stuttgart, Deutschland

Hauptberichter:

Prof. Dr.-Ing. Rainer Helmig

Mitberichter:

Prof. Dr.-Ing. Bernhard Weigand

Prof. Dr. Maurizio Santini

Tag der mündlichen Prüfung: 19.06.2020

Institut für Wasser- und Umweltsystemmodellierung
der Universität Stuttgart
2021

Heft 281 **A multi-scale approach for
drop/porous-medium
interaction**

von
Dr.-Ing.
Sina Ackermann

Eigenverlag des Instituts für Wasser- und Umweltsystemmodellierung
der Universität Stuttgart

D93 A multi-scale approach for drop/porous-medium interaction

Bibliografische Information der Deutschen Nationalbibliothek

Die Deutsche Nationalbibliothek verzeichnet diese Publikation in der Deutschen Nationalbibliografie; detaillierte bibliografische Daten sind im Internet über <http://www.d-nb.de> abrufbar

Ackermann, Sina:

A multi-scale approach for drop/porous-medium interaction, Universität Stuttgart. - Stuttgart: Institut für Wasser- und Umweltsystemmodellierung, 2021

(Mitteilungen Institut für Wasser- und Umweltsystemmodellierung, Universität Stuttgart: H. 281)

Zugl.: Stuttgart, Univ., Diss., 2021

ISBN 978-3-942036-85-6

NE: Institut für Wasser- und Umweltsystemmodellierung <Stuttgart>: Mitteilungen

Gegen Vervielfältigung und Übersetzung bestehen keine Einwände, es wird lediglich um Quellenangabe gebeten.

Herausgegeben 2021 vom Eigenverlag des Instituts für Wasser- und Umweltsystemmodellierung

Druck: DCC Kästl e.K., Ostfildern

Contents

List of Figures	XI
List of Tables	XV
Nomenclature	XVII
Abstract	XXIII
Zusammenfassung	XXV
1 Introduction	1
1.1 State of the art	3
1.2 Outline	7
2 Fundamentals	11
2.1 Fluid properties	12
2.2 REV-scale averaging approach	20
3 Free flow and flow in porous media	25
3.1 Free flow	25
3.1.1 Assumptions	26
3.1.2 Balance equations	26
3.1.3 Boundaries and boundary layers	27
3.2 Flow in porous media	28
3.2.1 Assumptions	29
3.2.2 Balance equations	29
3.2.3 Additional relations	30
4 Coupling concept without drops	33
4.1 Pore-scale considerations	33

4.2	Macro-scale coupling concept	37
4.2.1	Mechanical equilibrium	38
4.2.2	Thermal equilibrium	40
4.2.3	Chemical equilibrium	40
4.3	Numerical model	41
4.3.1	Discretization	42
4.3.2	Solving the nonlinear system	45
4.3.3	Implementation	46
5	Drops	49
5.1	Geometry of drops	50
5.2	Drop dynamics	51
5.3	Balance equations for a single drop	57
6	Coupling concept with drops in a lower-dimensional interface domain	61
6.1	Pore-scale considerations	63
6.2	Transfer from the pore- to the REV-scale	67
6.3	Full-dimensional interface domain	70
6.3.1	Assumptions	70
6.3.2	Balance equations	71
6.4	Lower-dimensional interface domain	74
6.5	Coupling concept with lower-dimensional interface domain	76
6.6	Numerical model	77
6.6.1	Pressure gradients and resulting fluxes	77
6.6.2	Upscaling	80
6.6.3	Extrusion factors	80
6.6.4	Workflow	81
7	Coupling concept with drops in a phase-field model domain	85
7.1	Phase-field model	86
7.2	Model compatibility	88
7.3	Coupling concept with phase-field model	90
7.4	Numerical model	91
8	Simulation results	93
8.1	Comparison with experiment	94
8.1.1	Experimental set-up	94

8.1.2	Simulation set-up	95
8.1.3	Results	96
8.1.4	Discussion	97
8.2	Formation, growth and detachment (Lower-dimensional interface) . . .	99
8.2.1	Model domain set-up and parameter values	99
8.2.2	Isothermal reference case	101
8.2.3	Nonisothermal reference case	104
8.2.4	Different pore sizes	106
8.2.5	Parameter study	106
8.2.6	Discussion	110
8.3	Merging	110
8.3.1	Results	111
8.3.2	Discussion	112
8.4	Film flow	112
8.4.1	Isothermal test case	113
8.4.2	Nonisothermal test case	113
8.4.3	Discussion	117
8.5	Comparison with simple coupling concept	117
8.5.1	Different numbers of drops	118
8.5.2	Reference case	119
8.5.3	Discussion	124
8.6	Formation, growth and detachment (Phase-field model)	124
8.6.1	Set-up	124
8.6.2	Phase-field model	125
8.6.3	Influence on macro-scale flow	127
8.6.4	Discussion	127
9	Summary	131
9.1	Conclusions	133
9.2	Outlook	134
	Bibliography	135

List of Figures

1.1	Different coupling concepts for free-flow/porous-medium-flow systems which are referred to or explained in this work.	8
2.1	Two fluids (gas and liquid) are present in the three compartments which represent free flow, flow in a porous medium and the common interface in between.	11
2.2	Surface tensions acting on the three-phase contact line	16
2.3	Contact angles for hydrophilic, hydrophobic and superhydrophobic surfaces	17
2.4	Wetting regimes on rough surfaces: a) homogeneous (Wenzel model), b) heterogeneous (Cassie-Baxter model)	18
2.5	Definition of the size of a representative elementary volume (REV) (adapted from Helmig [1997] and Baber [2014])	21
4.1	Continuity of fluxes and force balance for the gas phase in a single pore	34
4.2	Exemplary model domain Ω with the respective primary variables and normal vectors for Ω^{ff} and Ω^{pm}	38
4.3	Spatial discretization schemes	44
4.4	Schematic representation of the Jacobian matrix for the coupled system	46
5.1	Geometry of a drop	50
5.2	Forces acting on a sessile drop surrounded by a gaseous free flow	55
5.3	Mass balance for a single drop	59
5.4	Force balance at the drop surface A_{drop}°	60
6.1	Schematic overview of the three-domain approach with a lower-dimensional interface domain to include the droplet-related pore-scale processes in a macroscopic coupled free-flow/porous-medium-flow description	62

6.2	Three pore scenarios for two-phase flow between free flow and porous medium	63
6.3	A model domain with four compartments: ff and pm represent averaged REV-scale model subdomains, while if and bot represent the pore-scale. The numbers refer to the respective coupling conditions.	65
6.4	Real (dashed line) and homogenized (rectangles) pore-size distribution	68
6.5	Schematic representation of the full-dimensional interface domain . . .	70
6.6	The $k_r - S_l$ relationships for lateral fluxes with an exemplary value of $S_l^{\text{merge}} = 0.5$	73
6.7	The mass and energy fluxes between the interface domain and the neighboring domains occur along the direction of the dashed blue arrows, which does not coincide with the dimension of the interface domain itself. . .	75
6.8	Schematic view of the Jacobian matrix for the global system of equations with the respective submatrices for the free-flow, interface and porous-medium subdomains and associated couplings	78
6.9	Locations where the gas pressure is stored (circles) and extrapolated (squares)	78
6.10	Extrusion factors for one- and two-dimensional domains	81
6.11	Workflow to compute the droplet-related processes for each grid cell . .	83
7.1	Phase transition	86
7.2	Phase-field model domain	86
7.3	Exchange of boundary values between the two scales	90
8.1	The pore in the experimental set-up	94
8.2	Evolution of the drop volume, recorded with X-rays	97
8.3	Comparison of the results obtained with experiment and simulation . .	98
8.4	Dimensions and discretization of the model domain Ω . The purple numbers indicate the elements in the interface domain.	99
8.5	Exemplary distribution of drops in a square domain	100
8.6	Boundary conditions for the reference case	101
8.7	Drop volume evolution for the isothermal reference case	103
8.8	Drag and retention force for the isothermal reference case	103
8.9	Drop radius evolution for the isothermal reference case	104
8.10	Liquid saturation evolution for the isothermal reference case	105
8.11	Drop volume evolution for the isothermal and nonisothermal case . . .	105
8.12	Individual drop volumes for different pore-size classes	107

8.13	Total drop volumes for three different pore-size classes	107
8.14	Variation of inflow rates	108
8.15	Variation of free-flow velocities	109
8.16	Variation of temperatures	109
8.17	Touching of homogeneously distributed drops	111
8.18	Drop volume evolution for $n_{\text{pores}} = n_{\text{pores}}(\Phi)$	111
8.19	Drop-covered area and liquid saturation for $n_{\text{pores}} = n_{\text{pores}}(\Phi)$	112
8.20	Saturation for different boundary conditions under isothermal conditions	115
8.21	Saturation for different boundary conditions under nonisothermal conditions	116
8.22	Drop volumes for different pore radii	118
8.23	Gas pressure and velocity in the whole model domain at $t_1 = 158\text{s}$. . .	120
8.24	Free flow: Mass fraction of water in gas over x-axis	121
8.25	Free flow: Temperature over x-axis	121
8.26	Porous medium: Liquid saturation over y-axis	122
8.27	Porous medium: Capillary pressure over y-axis	122
8.28	Porous medium: Liquid pressure over y-axis	123
8.29	Porous medium: Temperature over y-axis	123
8.30	Computational domains and boundary conditions	125
8.31	Drop formation and growth in the phase-field model	126
8.32	Drop volume evolution computed by the phase-field model	126
8.33	Vapor pressure in the free flow	127
8.34	Liquid pressure in the porous medium	128
8.35	Liquid saturation in the porous medium	128

List of Tables

2.1	Fluid properties for the phases and components used in this work . . .	19
8.1	Initial and parameter values	96
8.2	Model domain for the comparison with experimental data	96
8.3	Initial and boundary values for the reference case	102
8.4	Material parameters of the porous medium	102

Nomenclature

Greek Letters

α_{BJ}	Beavers-Joseph coefficient	
δ	height, thickness	m
$\Delta\theta$	contact angle hysteresis	°
Δt	time step	s
η_r	relative passability	
γ	surface tension	N/m
λ	thermal conductivity	W/(m K)
μ	dynamic viscosity	Pa s
Φ	porosity	
τ	shear stress	Pa
θ	contact angle	°
φ	phase-field variable	
ρ	density	kg/m ³
ξ	extrusion factor	m, m ²

Roman Letters

A	area	m^2
A_g	sum of cross-sectional areas of gas-filled pore throats	m^2
A_l	sum of cross-sectional areas of liquid-filled pore throats	m^2
A_{drop}°	drop surface area	m^2
a	area fraction	
c	specific heat capacity	$\text{J}/(\text{kg K})$
c_d	drag coefficient	
c_F	Forchheimer coefficient	
d	diameter	m
D_{α}^{κ}	effective diffusion coefficient of component κ in phase α	m^2/s
f	specific free energy	J/kg
$f_{\bar{r}_{\text{pore}}}$	ratio of pores in pore-size class with mean pore radius \bar{r}_{pore}	
\mathbf{g}	gravity vector	m/s^2
H	Henry coefficient	Pa
h	specific enthalpy	J/kg
h_{drop}	drop height	m
\mathbf{I}	identity tensor	
\mathbf{J}	Jacobian matrix	
\mathbf{K}	intrinsic permeability tensor	m^2

k_r	relative permeability	
l	length	m
M	molar mass	kg/mol
m	mass	kg
\mathbf{n}	unit outer normal vector	
$n_{\bar{r}_{\text{pore}}}$	number of pores in pore-size class with mean pore radius \bar{r}_{pore}	
p	pressure	Pa
p_c	capillary pressure	Pa
q	sink/source term, flux term (mass or heat)	
\bar{r}_{pore}	mean pore radius	m
\mathbf{R}	global residual vector	
\mathbf{r}	local residual vector	
R	ideal gas constant ($R = 8.314\text{J}/(\text{K mol})$)	J/(K mol)
r	radius	m
S	saturation	
\mathbf{t}	tangential vector	
T	temperature	K
T_c	reference temperature ($T_c = 647.096\text{K}$)	K
\mathbf{u}	vector of unknowns	
u	specific internal energy	J/kg

\mathbf{v}	velocity	m/s
V	volume	m^3
w	free energy density	J/m^3
X	mass fraction	
x	mole fraction	

Superscripts

κ	component
a	air
ff	free flow
if	interface
pm	porous medium
w	water

Subscripts

α	phase
a	advancing (contact angle)
ca	contact area (drop)
drop	drop property
g	gas
l	liquid
n	nonwetting

r receding (contact angle)

s solid

sat saturated

w wetting

Selected Acronyms

Γ boundary of the model domain

Ω model domain

bot bundle-of-tubes compartment

Bo Bond number

Ca Capillary number

CCTPFA Cell-centered two-point flux approximation

ff free-flow compartment

if interface compartment

LDID lower-dimensional interface domain

pm porous-medium compartment

PFM phase-field model

Re Reynolds number

REV representative elementary volume

Abstract

The objective of this work was to develop a multi-scale coupling concept for free-flow/porous-medium-flow systems which takes drops at the common interface into account. These drops influence the surrounding flow processes due to their presence at the interface, where the exchange of mass, momentum and energy between the two flow compartments takes place. In most cases, the size of the drops is of the same order of magnitude as the pore diameters in a porous medium. However, for most applications, model domains on larger spatial scales are taken into account such that they resemble real-life scenarios. Resolving the large number of individual drops in such cases would require detailed pore-scale information and lead to high computational costs.

In previous models for coupled free-flow/porous-medium-flow systems, interfacial drops have often been neglected. In the scope of this work, we present two multi-scale coupling concepts which allow to compute the flow processes on the macro-scale, but take the influence of droplet-related pore-scale processes into account. Instead of resolving the individual drops, upscaling techniques are applied and the flow processes are described on the macro-scale. The aim of this work is to implement a numerical model which allows to qualitatively identify the influence of the drops on the exchange between free flow and porous medium. For this purpose, two approaches are introduced:

Lower-dimensional interface domain coupling concept: A three-domain coupling concept where the droplet-related processes are computed in a separate subdomain allows to formulate an individual set of balance equations which takes the drops into account. The interface subdomain is coupled to the free-flow and porous-medium-flow domains respectively to model the exchange of mass, momentum and energy between the three compartments. Under the assumption of a thin interface domain with the approximate height of a drop, it can be reduced by one dimension, resulting in a lower-dimensional domain compared to the remaining two subdomains. Depending on the flow conditions in the two adjacent flow compartments, drops form, grow and detach. Their influence is taken into account when computing mass and energy fluxes across the interface.

Abstract

The results obtained with this coupling concept match the data obtained with a simple experimental set-up for drop growth. The predictions of drop formation, growth and detachment for more complex test cases match the expectations. In addition, a test case where lateral fluxes of merged drops along the interface are considered delivers reasonable results. A comparison with the results obtained by the previous simple coupling concept shows that drops should not be neglected when taking coupled two-phase systems into account.

Phase-field model coupling concept: A multi-scale concept which actually resolves the flow and droplet-related processes on two different scales helps to obtain a qualitative assessment of the interactions between the two scales. In this approach, the free-flow and porous-medium-flow processes are modeled on the macro-scale, while a phase-field model is used to resolve the drops on the pore-scale. By exchanging data and setting them as boundary conditions, the communication between the two scales is established. Due to the current restrictions of the implemented phase-field model to an artificial fluid system, only a qualitative analysis is possible with this coupling approach. The results show that drop formation and growth can be predicted for simple scenarios. However, compared to the lower-dimensional interface domain concept, the phase-field approach has the perspective to model the droplet-related processes with a smaller loss of pore-scale information.

With further extensions and modifications, the two multi-scale coupling concepts could be convenient tools to predict the behavior of drops in real-life applications. For example, adapting the models to take the influence of the drops on the free-flow velocity into account would open up a whole range of possibilities.

In summary, we present two multi-scale coupling concepts and their respective numerical implementations, which can potentially be applied to realistic problems. While their results already match phenomenological observations related to drops, the coupling concepts need to be improved for more detailed predictions and further research.

Zusammenfassung

Im Rahmen dieser Arbeit wurde ein mehrskaliges Kopplungskonzept für Systeme bestehend aus freier Strömung und porösem Medium unter der Berücksichtigung von Tropfen an der gemeinsamen Grenzfläche entwickelt. Diese Tropfen beeinflussen die Strömungsprozesse in der Umgebung, da sie direkt an der Schnittstelle entstehen, wo der Austausch von Masse, Impuls und Energie zwischen den beiden Gebieten stattfindet. In den meisten Fällen ist die Größe der Tropfen vergleichbar mit der Porengröße im porösen Medium. In vielen Anwendungen werden jedoch Modellgebiete auf größeren räumlichen Skalen betrachtet, um realistische Szenarien abbilden zu können. Die große Anzahl an Tropfen in solchen Fällen einzeln aufzulösen würde detaillierte Informationen auf der Porenskala erfordern, sowie zu hohen Rechenkosten führen.

In bisherigen Modellkonzepten für gekoppelte Systeme aus freier Strömung und porösem Medium wurden Tropfen an der Grenzfläche oft vernachlässigt. Im Rahmen dieser Arbeit werden zwei mehrskalige Kopplungskonzepte vorgestellt, mit denen die Strömungsprozesse auf der Makroskala berechnet werden können, wobei der Einfluss der tropfenabhängigen Prozesse auf der Porenskala berücksichtigt wird. Anstatt die einzelnen Tropfen aufzulösen, werden ihre Effekte aufsummiert und auf die Strömungsprozesse auf der Makroskala übertragen. Ziel der Arbeit ist es, ein numerisches Modell zu implementieren mit dem der Einfluss der Tropfen auf den Austausch zwischen freier Strömung und porösem Medium qualitativ bestimmt werden kann. Zu diesem Zweck werden zwei Ansätze vorgestellt:

Kopplungskonzept mit niedrigdimensionalem Grenzflächengebiet: Bei einem Kopplungskonzept mit drei Gebieten, in dem die tropfenabhängigen Prozesse in einem separaten Gebiet berechnet werden, kann ein individueller Satz an Bilanzgleichungen formuliert werden, um die Tropfen zu berücksichtigen. Das Grenzflächengebiet ist mit der freien Strömung und dem porösen Medium gekoppelt, um den Austausch von Masse, Impuls und Energie zwischen den drei Gebieten zu modellieren. Unter der Annahme eines

Zusammenfassung

dünnen Grenzflächengebiets, das etwa so hoch ist wie ein Tropfen, kann das Gebiet um eine Dimension reduziert werden. Dies führt zu einem Gebiet niedrigerer Dimension, verglichen mit den beiden anderen Gebieten. Abhängig von den Strömungsbedingungen in den benachbarten Gebieten bilden sich Tropfen, wachsen und lösen sich ab. Ihr Einfluss wird bei der Berechnung der Massen- und Energieflüsse über die Grenzfläche berücksichtigt. Die Ergebnisse, die sich mit diesem Kopplungskonzept ergeben, passen zu den Daten aus einem einfachen experimentellen Aufbau für Tropfenwachstum. Die Vorhersagen für Tropfenbildung, -wachstum und -ablösung für komplexere Testfälle entsprechen den Erwartungen. Sinnvolle Ergebnisse liefert außerdem ein Testfall, in dem laterale Flüsse aus sich verbindenden Tropfen entlang der Grenzfläche berücksichtigt werden. Ein Vergleich mit den Ergebnissen aus dem einfachen Kopplungskonzept ohne Tropfen zeigt, dass Tropfen nicht vernachlässigt werden sollten wenn gekoppelte Zwei-Phasen-Systeme untersucht werden.

Kopplungskonzept mit Phasefeldmodell: Ein mehrskaliges Kopplungskonzept das die Strömungs- und tropfenabhängigen Prozesse tatsächlich auf zwei verschiedenen Skalen auflöst hilft, eine qualitative Auswertung der Interaktionen zwischen den beiden Skalen zu erhalten. Bei diesem Ansatz werden die Strömungsprozesse in freier Strömung und porösem Medium auf der Makroskala modelliert, während ein Phasefeldmodell die Tropfen auf der Porenskala auflöst. Indem Daten ausgetauscht und als Randbedingungen gesetzt werden, wird die Kommunikation zwischen den beiden Skalen ermöglicht. Da das verwendete Phasefeldmodell bisher nur mit künstlichen Fluidsystemen anwendbar ist, kann mit diesem Kopplungsansatz nur eine qualitative Analyse durchgeführt werden. Die Ergebnisse zeigen, dass Tropfenbildung und -wachstum für einfache Szenarien vorhergesagt werden können. Im Vergleich zum Kopplungskonzept mit niedrigdimensionalen Grenzflächengebiet hat das Phasefeldmodell jedoch die Perspektive, die tropfenabhängigen Prozesse mit geringerem Verlust von Informationen der Porenskala zu modellieren.

Mit Erweiterungen und Modifizierungen könnten die beiden mehrskaligen Kopplungskonzepte nützliche Werkzeuge sein, um das Verhalten von Tropfen in realistischen Anwendungen vorherzusagen. Zum Beispiel würde eine Reihe von Möglichkeiten eröffnet werden, wenn der Einfluss der Tropfen auf die Geschwindigkeit der freien Strömung berücksichtigt werden würde.

Zusammenfassend werden in dieser Arbeit zwei mehrskalige Kopplungskonzepte und ihre jeweiligen numerischen Implementierungen vorgestellt, welche potenziell auf realistische

Probleme angewendet werden können. Während die Ergebnisse schon zu phänomenologischen Beobachtungen im Bezug auf Tropfen passen, müssen die Kopplungskonzepte verbessert werden um genauere Vorhersagen und weitere Forschung zu ermöglichen.

1 Introduction

Interface processes dominate the interaction of flow and transport between a free flow and a flow in a porous medium. Quantifying the transfer fluxes of mass, momentum and energy is crucial for applications like evaporation from soil, water management in fuel cells or transport of therapeutic agents in the human body.

In case of a hydrophobic porous medium, water emerging from the porous medium forms drops which block the pores for gaseous fluxes. When describing such systems, an important aspect is to understand how the drops accumulate on the surface of a porous medium and how this process influences the exchange processes at the interface between the porous medium and its surrounding. For example, in applications such as the water management of fuel cells, thermal insulation of building exteriors or turbine heat exchange processes, the drops influence the mass and heat fluxes significantly.

The examples given above represent coupled systems consisting of a gaseous free flow and a two-phase liquid-gas flow in a hydrophobic porous medium. The interfacial region where the drops form is approximately of the same height as the length scale of the pores, but influences the exchange processes significantly. Due to a pressure gradient in the respective direction, the liquid phase in the porous medium might reach the interface to the free-flow region. There, it either evaporates immediately or forms drops on the porous hydrophobic surface. Such interfacial drops influence the transfer processes directly in different ways: a larger liquid surface area due to the curved drop surfaces accelerates evaporation from the porous medium, the exchange of gas is hindered due to the blocking of pores by liquid drops, higher free-flow velocities due to a reduced cross-section lead to a pressure drop along the interface and higher evaporation rates, and so on. Besides formation and growth, dynamic drop processes such as deforming, spreading, merging, detaching, breaking up, re-attaching and shrinking affect the two flow regimes.

Predicting and controlling the number of water drops and their behavior is an important aspect to improve the application designs. Often, the drops' influence on the surrounding

flow regimes is of greater interest than the fate of the individual drops. Nevertheless, detailed knowledge of the drop behavior under different conditions is necessary in order to generate realistic models. Experiments are conducted and prototypes are built to observe and measure the phenomena directly. Besides such practical investigations, theoretical models and virtual prototypes have become an important tool to obtain a better understanding of the complex interactions. Numerical simulations, which are based on conceptual and mathematical models, are often employed to thoroughly investigate the occurring processes.

Developing a simulation tool for real-life scenarios requires a precise physical description of the relevant processes as well as an efficient model with respect to computational costs. For the coupled systems described above, usually only one of these demands can be satisfied due to the different temporal and spatial scales. If the interest lies in the evolution of pressure and velocity fields as well as water distribution and temperature, macro-scale variables and balance equations are sufficiently accurate to describe the macroscopic flow behavior. Processes happening on smaller scales are then averaged and upscaled to obtain an efficient model with respect to computational costs. However, this procedure leads to a loss of pore-scale information. In the case of interfacial drops, pore-scale information becomes crucial because these relatively tiny drops influence the overall exchange procedure between free flow and flow in a porous medium. Resolving the pore-scale information leads to high grid resolutions and small time steps, which are then again expensive with respect to computational time and effort.

The aim of this work is to overcome this dilemma by developing a multi-scale, multi-physics model which includes the influence of droplet-related pore-scale interface processes on the macroscopic flow behavior. Relevant pore-scale information has to be included, while the numerical simulation of the coupled system should still be computationally efficient. We present two multi-scale approaches with different representations of the droplet-related processes to tackle this challenging task. In both models, upscaling procedures are developed to take a variety of pore-scale processes into account. With the first approach, we want to model realistic scenarios in order to predict the amount of water that accumulates on the porous surface. The second approach is intended to give insights on the mutual influence between drops and porous media in a qualitative manner only.

For the first multi-scale coupling approach, we develop a three-domain concept with a lower-dimensional interface domain to account for the droplet-related processes. Balance

equations which take drops into account are formulated for the interface domain. With a simple upscaling procedure, the area covered by drops can be computed and taken into account for the fluxes across the interface. In addition, we include lateral fluxes along the interface in our model concept. With this conceptual model, we obtain a numerical model which allows to predict the change in the macroscopic flow behavior caused by drops at the common interface. We compare the results of a simple test case with an experiment to validate our approach. Then, we set up more complex scenarios to predict the evolution of drop volumes and thin water films over time.

In the second multi-scale coupling concept, the drops are computed on the pore-scale, while the free flow as well as the flow in the porous medium are modeled on the macro-scale. The systems on both scales are solved separately, but exchange information such as pressure, velocity and drop volumes. Even though this concept is limited to an artificial fluid system, the results can be used to further develop multi-scale coupling concepts.

The results obtained with both multi-scale approaches show that drop formation, growth and detachment can be captured. With the lower-dimensional interface domain concept, even lateral fluxes along the interface can be taken into account. Parameter variations yield the expected results. In addition, a comparison with a simpler coupling concept that neglects drops shows significant differences in the results and further stresses the importance of taking drops into account.

1.1 State of the art

This work is based on previous findings in the research fields of droplet-related processes as well as coupled free-flow/porous-medium-flow systems. Both experiments and numerical simulations have helped to gain knowledge about the occurring processes in such settings on different scales. The following literature overview is limited to related works on mathematical, conceptual and numerical models.

Droplet-related processes

Liquid drops are usually modeled on a small spatial scale with the aim to describe the related processes as exactly as possible in a physical and phenomenological way. The

most common pore-scale models which approximate the complex physics are the volume-of-fluid method and the Lattice-Boltzmann method.

With the volume-of-fluid (VOF) method, a single set of momentum equations is solved for liquid and vapor, and the volume fractions of both phases within the domain are tracked. It is applied e.g. by Baggio and Weigand [2019] to model the impact of a drop on a superhydrophobic surface. Theodorakakos et al. [2006] apply the VOF method to investigate detaching drops in fuel cells. Another model for water dynamics in fuel cells is presented by Qin et al. [2012], where simplified geometries of the different layers are used to investigate drop detachment and film flow along the corners of the gas channel. Another example is the work of Annapragada et al. [2012], who describe the motion of a drop along an inclined surface with a volume-of-fluid/continuous-surface-force (VOF-CSF) model.

For the Lattice-Boltzmann method (LBM), the discrete Boltzmann transport equation is solved which describes the statistical distribution of particles in a fluid with the help of a collision operator. This method is e. g. applied in the work of Frank and Perre [2012], who investigate spreading drops on a porous surface with two different equilibrium contact angles by applying the LBM. Another application of the LBM is presented by Wang and Sun [2018], where a sensitivity analysis on the corresponding parameters which influence the coalescence between a free drop in gas and a sessile drop on a wetting surface is conducted.

The examples mentioned above represent only a small fraction of the numerous publications on pore-scale models for droplet-related processes. However, in the scope of this work we focus on including these pore-scale phenomena in model concepts which operate on a larger spatial scale. Therefore, we build on the knowledge gained by these approaches, but do not apply any of these model concepts in our work.

Coupled free-flow/porous-medium-flow systems

Several macro-scale models for coupled free-flow/porous-medium-flow systems can be found in the literature. Commonly, either a one-domain or a two-domain approach is used for such systems.

In the one-domain approach, one set of balance equations describes the flow and transport processes in the whole model domain. Brinkman [1949] combines the Stokes equation

with Darcy's law to obtain a momentum balance equation which is valid in the whole model domain. Parameters such as porosity and permeability are defined depending on space, such that they either represent the free-flow domain or the porous-medium domain respectively. Due to the continuous definition of the spatial parameters, a smooth transition zone is given. In this case, no additional interface or coupling conditions are necessary to connect the two flow regimes with each other. This approach is amongst others applied by Goyeau et al. [2003], Valdés-Parada et al. [2006], Basirat et al. [2015] and Antoniadis and Papalexandris [2016].

For the two-domain approach, two sets of balance equations are needed. Consequently, a sharp interface separates the two flow regimes and necessitates the formulation of appropriate interface or coupling conditions. The interface is an internal boundary where both subdomains coincide. Here, coupling conditions instead of boundary conditions are set accordingly on both sides to describe the continuous exchange of mass, momentum and energy across the interface. Analyses for coupling conditions in single-phase systems are given by Discacciati and Quarteroni [2009] and Rivière and Yotov [2005]. In the approach of Beavers and Joseph [1967], the coupling conditions involve a velocity jump at the interface, while Ochoa-Tapia and Whitaker [1995] incorporate a stress jump. Shavit [2009] presents a comprehensive overview of research related to transport phenomena at the interface between free flows and porous media.

If a single-phase gaseous free flow is coupled with a two-phase flow in a porous medium, the presence of the liquid phase at the interface has to be treated appropriately. The model concept for compositional nonisothermal systems presented by Mosthaf et al. [2011] is based on the assumption that all normal water fluxes reaching the interface evaporate directly into the gaseous free flow. The approaches by Masson et al. [2016] and Chen et al. [2014] assume the same. Another possibility is to assume that the liquid phase does not even reach the interface, as implemented by Koch et al. [2020]. In both approaches, the liquid phase cannot be modeled in the free-flow region due to the assumption of a single-phase flow. Therefore, the fact that liquid drops might form and move on the porous surface is neglected in these cases.

Drops in coupled free-flow/porous-medium-flow systems

The three-dimensional multi-phase, multi-fluid approach presented by Gurau et al. [2008] and Gurau and Mann [2010] takes drop formation and detachment in a fuel cell into

account. In this approach, both flow regimes are modeled on the macroscopic scale with one transport equation for each phase. The formation of drops depends on the liquid saturation next to the surface. Both gravitational forces and a two-phase drag force are taken into account to determine when a drop detaches.

Berning et al. [2009] extend the multi-fluid approach by taking the irreducible saturation into account to model the accumulation of liquid water in the gas channel of a fuel cell. At the interface, they set the liquid pressure as the capillary pressure between the liquid phase pressure in the porous medium and the pore entry pressure.

For flow in porous media, pore-network models can be used if the porous structure is known. These models represent the individual pore throats and pore spaces of the porous medium, as e. g. described by Joekar-Niasar et al. [2010]. Qin et al. [2016] model water and vapor transport in a fuel cell with the help of two coupled pore-network models which represent the gas diffusion layer and micro porous layer respectively. Weishaupt et al. [2019] couple a pore-network model with a free-flow domain to investigate the exchange processes for discrete pores. Based on this approach, individual drops could be computed either on single pore throats or as accumulations of liquid fed by several pore throats. Such an approach to model drop formation and detachment with the help of a pore-network model is currently developed at the Department of Hydromechanics and Modelling of Hydrosystems (University of Stuttgart).

An attempt to include droplet-related pore-scale processes into a macroscopic coupled model as described by Mosthaf et al. [2011] has been made by Baber et al. [2016]. They combined the simple coupling concept for compositional, nonisothermal flow with a complex coupling concept derived at the pore-scale with the help of a bundle-of-tubes concept. With this new complex concept, drops at the coupling interface can form and grow due to fluxes from the porous medium into the free-flow domain, and detach if the forces acting on the drop are larger than the retention forces between the drop and the solid surface. The model operates on the macro-scale and does not resolve the individual drops. Several two-dimensional test cases are set up and provide results which show drop formation, growth and detachment. A drawback of this approach is that only a few upscaled drops can be computed.

The literature review shows that macro-scale models for coupled free-flow/porous-medium-systems usually neglect the presence of interfacial drops. Pore-scale models, however, are not suitable for modeling more than a few drops. Since we see promising opportunities in closing this gap by further extending the simple coupling concept by Mosthaf et al.

[2011], we base our approach on the derivation and realization presented by Baber et al. [2016] to obtain a multi-scale model for the interactions between drops and flow in porous media.

1.2 Outline

In the scope of this work, we present physical, mathematical and numerical models as well as simulation results for coupling concepts for systems consisting of a single-phase free flow and a two-phase flow in a porous medium. An overview of the coupling concepts presented or referred to in this work is given in Figure 1.1 .

In Chapter 2, fundamental terms are explained in order to create a common ground for the different conceptual models.

Chapter 3 addresses free flow and flow in porous media on the macro-scale. Assumptions and balance equations for both flow compartments are given.

A simple coupling concept without drops for the exchange of mass, momentum and energy is outlined in Chapter 4. We formulate pore-scale considerations as well as a macro-scale concept, which is then transferred to a numerical model.

Chapter 5 describes drops and droplet-related processes which are relevant when modeling coupled free-flow/porous-medium-flow systems. As preparation for the coupling concept, balance equations for a single drop are provided.

Chapter 6 features a new multi-scale coupling concept which upscales the droplet-related pore-scale interface processes in an additional lower-dimensional domain.

A second multi-scale coupling concept is developed in cooperation with Lukas Ostrowski and presented in Chapter 7. Here, the drops are modeled on the pore-scale with the help of a phase-field model.

Chapter 8 contains the results of various numerical simulations. For a single drop, experimental data is compared to the data obtained with our multi-scale coupling concept. Results for drop formation, growth and detachment as well as lateral fluxes along the interface are presented and discussed. In addition, the results of the drop coupling concept are compared to the ones obtained with the simple coupling concept. Finally, results for the multi-scale coupling concept with a phase-field model are presented.

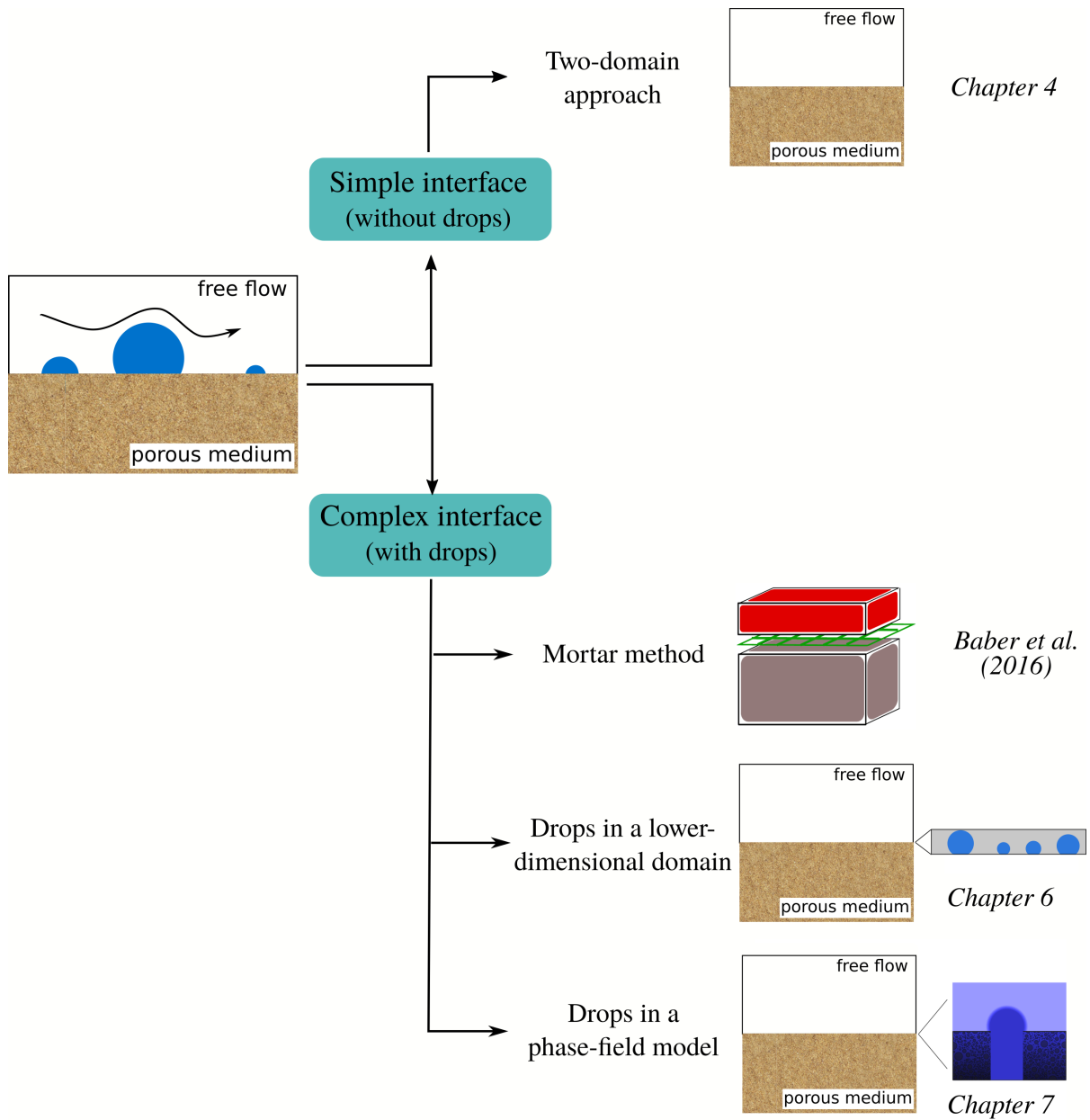


Figure 1.1: Different coupling concepts for free-flow/porous-medium-flow systems which are referred to or explained in this work.

Chapter 9 concludes this thesis with a summary and an outlook.

2 Fundamentals

This chapter explains the fundamental terms and assumptions which are used in the model concepts in the next chapters. In the following, we assume three phases to be present: one solid and two fluid phases, namely gas and liquid. We consider a system consisting of three different flow compartments: free flow, flow in a porous medium and flow across the common interface in between, as shown in Figure 2.1. The models in the scope of this work are based on the assumption of local thermodynamic equilibrium, i. e. local mechanical, thermal and chemical equilibrium are assumed.

Relevant fluid properties to model such systems are explained in Section 2.1. For the interface and porous-medium compartments, a volume-averaging approach is applied. The basic ideas and averaged quantities are described in Section 2.2.

Further details on the physical background of flow and transport processes can be found in general fluid mechanics literature such as the book by White [1968]. For flow in porous media and the related averaged quantities we refer to the works of Helmig [1997] and Bear [2013].

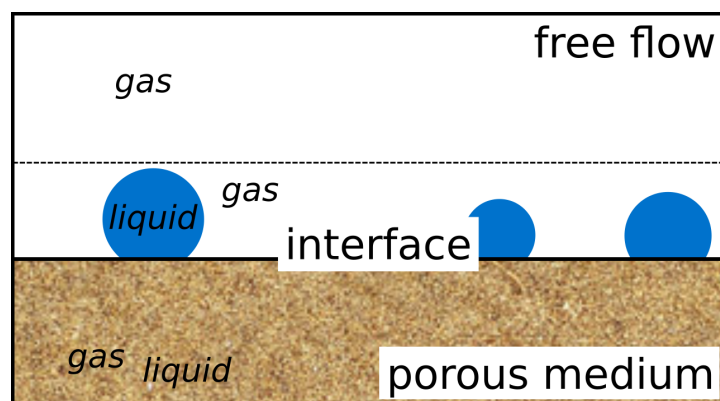


Figure 2.1: Two fluids (gas and liquid) are present in the three compartments which represent free flow, flow in a porous medium and the common interface in between.

2.1 Fluid properties

Fluids are made up of molecules which move driven by attraction, repulsion and collisions. Describing a fluid with the help of individual molecules and their positions corresponds to a consideration on the *molecular scale*. As an example, 1g of water contains $3 \cdot 10^{22}$ molecules. Due to the large number of molecules even in small portions of fluid, resolving each of them leads to high computational costs, especially with respect to storage capacity and CPU time.

However, the behavior of the molecules determines fluid properties such as density and viscosity. Therefore, a common approach is to average over a large number of molecules to obtain continuous differentiable functions. This *continuum approach* can be applied if the size of a flow system is much larger than the free path of the molecules. With the continuum approach, fluids can be described as phases consisting of components.

Components

A *component* κ is an accumulation of molecules of either a single chemical element (e. g. hydrogen) or of a molecular compound (e. g. water). In some cases, pseudo-components can be defined which are made up of several chemical substances, but are dominated by the properties of one species (e. g. air). In the scope of this work, water (superscript w) and air (superscript a) are treated as components.

Air

Air consists of several chemical elements such as nitrogen, oxygen, carbon dioxide, water vapor and small amounts of other gases, which can all be modeled as individual components. However, in many cases it is possible to regard air as a pseudo-component to simplify its description. Therefore, we consider air as a single component consisting of all of the named elements except for water vapor. Its properties are similar to the ones of its main component nitrogen, which makes up approximately 78% of the air volume.

Water

We assume the component water to be pure H₂O in either liquid or gaseous (vapor) form. Fluid properties such as density, enthalpy and heat capacity are calculated according to the empirically obtained equations presented by The International Association for the Properties of Water and Steam as listed by Cooper and Dooley [2007]. At standard ambient conditions ($T = 298.15\text{K}$, $p = 10^5\text{Pa}$), water is liquid with a density of approximately 1000kg/m^3 .

Phases

A *phase* α is a form of matter which is physically separated from other phases by an interface where thermodynamic properties such as pressure, density and temperature are possibly discontinuous. At standard conditions, a phase can be solid, liquid or gaseous. Within each phase, its thermodynamic properties and composition are relatively homogeneous. Due to phase transitions such as evaporation, condensation, dissolution and degassing, a phase might disappear or reappear during a flow process.

A gas is a fluid which does not have a free surface and takes up all of the available space. Therefore, only one gas phase can be present. We assume the gas phase to be a compressible fluid, which consists of the components air and water vapor. If a gas is assumed to be ideal, the ideal gas law can be applied:

$$pV = nRT , \quad (2.1)$$

where n is the number of moles and $R = 8.314\text{J}/(\text{molK})$ is the universal gas constant.

In contrast to gas, two or more liquid phases can mix (miscible) or exist next to each other (immiscible). In the scope of this work, the liquid phase is assumed to be incompressible and made up of water and dissolved air.

A porous medium consists of a solid matrix, which is assumed to be rigid and immobile in the scope of this work. Additionally, we assume gas and liquid to be present in the porous medium. In the interface compartment, a gas phase and liquid drops exist. The free flow consists of a gas phase only.

Mass and mole fractions

Each component κ can be quantified via its mass fraction X_α^κ or mole fraction x_α^κ with respect to a certain phase α . The sum of fractions within one phase sums up to one:

$$\sum_{\kappa} X_\alpha^\kappa = \sum_{\kappa} x_\alpha^\kappa = 1. \quad (2.2)$$

The relation between mass and mole fractions is given via the molar mass M^κ

$$X_\alpha^\kappa = \frac{x_\alpha^\kappa M^\kappa}{\sum_{\kappa} x_\alpha^\kappa M^\kappa}. \quad (2.3)$$

Phase composition

When a gas and a liquid phase coexist in chemical equilibrium, their compositions can be calculated with the help of molar quantities. In an ideal gas mixture, the partial pressure exerted by a component κ is proportional to its mole fraction:

$$p_g^\kappa = x_g^\kappa p_g. \quad (2.4)$$

According to Dalton's law, the sum of all partial pressures equals the total gas pressure:

$$\sum_{\kappa} p_g^\kappa = p_g. \quad (2.5)$$

Due to the phase equilibrium, the saturated vapor pressure corresponds to the partial pressure of the vapor of the main component in the liquid phase, i. e. $p_{\text{sat}}^w = p_g^w$ in our case. Combining this with Equations (2.4) and (2.2) yields

$$x_g^w = \frac{p_{\text{sat}}^w}{p_g} \text{ and } x_g^a = 1 - x_g^w. \quad (2.6)$$

To determine the mole fractions in the liquid phase, Henry's law can be applied. It states that the amount of dissolved gas in liquid (x_l^a) is proportional to its partial pressure above the liquid (p_g^a) by the Henry coefficient H_{gl}^a . With Henry's law and Equation (2.2), the mole fractions in the liquid phase are given as

$$x_l^a = \frac{p_g^a}{H_{gl}^a} \text{ and } x_l^w = 1 - x_l^a. \quad (2.7)$$

Density and viscosity

Density and viscosity both depend on pressure and temperature. The density of a phase α quantifies the ratio of its mass to the volume it occupies:

$$\rho_\alpha = \frac{m_\alpha}{V_\alpha}. \quad (2.8)$$

The dynamic phase viscosity μ_α describes the resistance of a fluid to deformation due to a flow field with velocity \mathbf{v}_α . For Newtonian fluids, it relates the shear stress τ linearly with the velocity gradient, i. e. $\tau = \mu_\alpha \frac{dv_{\alpha,x}}{dy}$.

Internal energy, enthalpy and heat capacity

The internal energy U is the sum of the internal kinetic and potential energy of all present molecules within a system. Instead of the total quantity, the specific internal energy $u = \frac{U}{m}$ is used in the scope of this work.

The sum of the internal energy and the volume-changing work in a system yields the enthalpy $H = U + pV$. The same relation holds for the specific enthalpy:

$$h = u + \frac{p}{\rho}. \quad (2.9)$$

The specific heat capacity of a system is either defined for a constant volume (c_v) or a constant pressure (c_p):

$$c_v = \frac{\partial u}{\partial T}, \quad c_p = \frac{\partial h}{\partial T}. \quad (2.10)$$

For ideal gases, the relation $c_p - c_v = \frac{R}{M}$ holds.

Surface tension and capillary pressure

When a gas and a liquid phase coexist, they are separated by an interface. In case of air and liquid water, the water molecules are strongly attracted to each other (cohesion), but only weakly attracted to the air molecules in the surrounding (adhesion). Due to this imbalance of attractions, a net inward force into the liquid phase causes a surface tension γ along the phase interface. Since liquids tend to reduce their surface area to

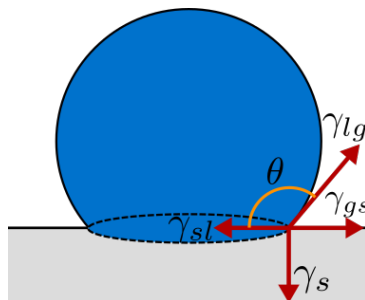


Figure 2.2: Surface tensions acting on the three-phase contact line

reach a state of minimum surface energy, this results in a curved interface. In mechanical equilibrium, the pressure difference across the curved interface is balanced by the surface tension and called *capillary pressure*, as described by the Young-Laplace equation:

$$\Delta p = p_c = \gamma \left(\frac{1}{r_x} + \frac{1}{r_y} \right), \quad (2.11)$$

where r_x and r_y are the radii of the curved interface in the two principal directions. The pressure difference is defined as $\Delta p = p^{\text{inside}} - p^{\text{outside}}$, where *inside* refers to the concave side of the interface. For spherical caps with $r = r_x = r_y$, we obtain $p_c = \frac{2\gamma}{r}$.

When the two fluids come in contact with a solid, adhesive forces are invoked. The magnitude and direction of these forces depend on the intermolecular interactions between fluid and solid, surface texture, electric charge and even possible vibrations (Niu and Tang [2014]). A three-phase contact line is established, as shown in Figure 2.2. Along the contact line, the surface tension forces balance out such that the net force per unit length is zero. Young [1805] derives an equation for surface wetting which balances the horizontal components of the surface tensions with the help of the contact angle θ :

$$\gamma_{lg} \cos(\theta) = \gamma_{sl} - \gamma_{sg}. \quad (2.12)$$

Contact angle and wettability

The angle between the fluid interfaces and the solid surface is called *contact angle* θ . Wetting fluids have a contact angle $\theta < 90^\circ$, for nonwetting fluids the contact angle is $\theta \geq 90^\circ$. With respect to water, the following wettability properties are distinguished (see Figure 2.3):

- hydrophilic: $\theta < 90^\circ$,
- hydrophobic: $90^\circ \leq \theta \leq 150^\circ$,
- superhydrophobic $\theta > 150^\circ$.

On a hydrophilic surface, water forms a thin film to maximize the contact area between water and solid. In case of a hydrophobic surface, the contact area is minimized, because the molecular attraction between air and solid is larger than the one between water and solid. Consequently, the water accumulates in drops which touch as little of the solid surface as possible.

A static or equilibrium contact angle θ^* establishes on ideal (flat, chemically homogeneous, perfectly smooth, rigid, isotropic) surfaces. In the equilibrium state, a drop is a spherical segment with a circular contact line and a constant contact angle along the contact line. The equilibrium state might be disturbed by external forces (e. g. gravity, flow forces in the surrounding), or volume changes caused by growth (liquid flux into the drop) or shrinkage (penetration, evaporation). Such disturbances lead to varying contact angles along the contact line. If a drop is deformed due to a flow field, two specific contact angles are defined: The contact angle which is observed where the flow field hits the drop is called the receding contact angle, while its opponent on the other side is the advancing contact angle. The difference between these two is the contact angle hysteresis $\Delta\theta = \theta_a - \theta_r$, which depends on the respective liquid-solid combination (see e.g. Joekar-Niasar [2010]). For an ideal surface, the contact angle hysteresis is consequently $\Delta\theta = 0$. As long as the contact angle is $\theta_r \leq \theta \leq \theta_a$, the contact line is pinned, with varying contact angles along its course. Exceeding the range of stable contact angles leads to a displacement of the contact line.

For non-ideal rough surfaces, two wetting regimes can be distinguished for the liquid phase as shown in Figure 2.4: Homogeneous wetting, where the liquid fills the spaces between the elevated parts of the solid surface, or heterogeneous wetting, where the gas

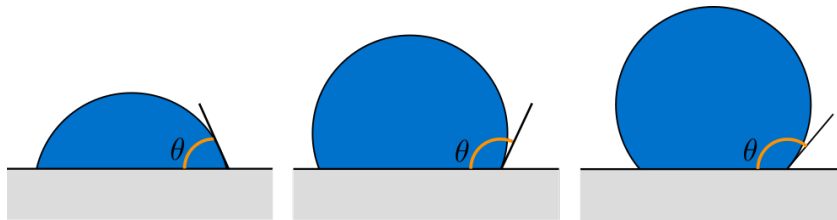


Figure 2.3: Contact angles for hydrophilic, hydrophobic and superhydrophobic surfaces

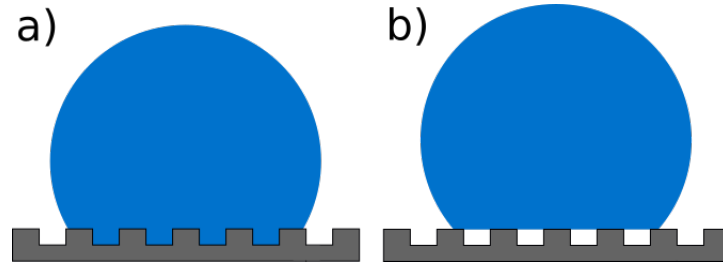


Figure 2.4: Wetting regimes on rough surfaces: a) homogeneous (Wenzel model), b) heterogeneous (Cassie-Baxter model)

phase fills these voids and the liquid's surface sits on top of the rough structure. For the homogeneous wetting regime, the Wenzel model (Wenzel [1936]) is usually applied, while the Cassie-Baxter model (Cassie and Baxter [1944]) describes the heterogeneous wetting regime. In both cases, the equations for the contact angles are derived depending on the drop radius, roughness ratio and wet surface fractions. The two models can only be applied when the drop size is large compared to the scale of the surface roughness. Since we assume the drop radii to be of the same scale as the pore radii in the scope of this work, we do not use either of these models to describe drops on the surface a porous medium.

To close this section, a list of all relevant fluid properties together with the respective equations to determine their values in the scope of this work is given in Table 2.1.

Density	$\varrho_g = \varrho_g^a + \varrho_g^w = \frac{p_g M^a}{RT} + \varrho_g^w(T, p)$	ideal gas, Cooper and Dooley [2007]
	$\varrho_l = \varrho_l^{\text{mol},w}(M^w x_l^w + M^a x_l^a)$	Class et al. [2002]
Diffusion coefficient	$D_g = 2.13 \cdot 10^{-5} \frac{10^5}{p_g} \left(\frac{T}{273.15}\right)^{1.8}$	Vargaftik [1975]
	$D_l = 2.01 \cdot 10^{-9} \frac{T}{273.15+25}$	Reid et al. [1987]
Specific enthalpy	$h_g = X_g^w h^w + X_g^a h^a$	Class [2001]
	$h_l = h_l^w$	
	$h_g^a = c_g^a(T - 273.15)$	Kays et al. [2005]
	$h_\alpha^w = h_\alpha^w(p_\alpha, T)$	Cooper and Dooley [2007]
Specific heat capacity	$c_g = c_g^a x_g^a + c_g^w x_g^w$	
	$c_l = c_l^w$	
	$c_g^a = c_g^a(T, p_g)$	Hollis [1996]
	$c_\alpha^w = c_\alpha^w(T, p_\alpha)$	Cooper and Dooley [2007]
Specific internal energy	$u_\alpha = h_\alpha - \frac{p_\alpha}{\varrho_\alpha}$	
Surface tension	$\gamma_{lg} = 0.2358 \cdot \left(1 - \frac{T}{T_c}\right)^{1.256}$ $\cdot \left(1 - 0.625\left(1 - \frac{T}{T_c}\right)\right)$	Petrova and Dooley [2014]
Thermal conductivity	$\lambda_g = \lambda_g^a = 0.02555535$	Linstrom and Mallard [2018]
	$\lambda_l = \lambda_l^w(T, p_l)$	Daucik and Dooley [2011]
Viscosity	μ_g (Wilke method)	Reid et al. [1987]
	$\mu_l = \mu_l^w$	

Table 2.1: Fluid properties for the phases and components used in this work

2.2 REV-scale averaging approach

Based on the continuum approach, flow processes can be described on different spatial scales. Flow in porous media is characterized by the pore structure of the solid matrix. Individual pore sizes and shapes as well as their distribution and connectivity influence the flow and transport processes. If the pore network's geometry is known, a *pore-scale* model is applicable. On the pore-scale, the phase interfaces within the pores are resolved and the flow can be described with the Navier-Stokes equations. One example for such models are pore-network models, which are commonly used if pore-scale information is available and small-scale processes are to be examined, as e. g. done by Joekar-Niasar et al. [2010]. Of course, the high resolutions and high numbers of unknowns lead to high computational costs, especially for larger model domains.

In such cases, it might be appropriate to average over representative elementary volumes (REV) to obtain an REV- or *macro-scale* model. An REV must be large enough to smoothen out fluctuating properties, but small enough to allow the consideration of heterogeneous properties such as permeability lenses or spatial changes in porosity, as shown in Figure 2.5. The effects of the pore-scale processes are then averaged over such a volume, yielding volume-related quantities such as porosity and saturation. With the saturation, the capillary pressure and relative permeability can be described on the REV-scale. Additionally, effective material parameters such as porosity and intrinsic permeability can be defined. The respective phase velocities can be computed with Darcy's law for low Reynolds numbers and Forchheimer's law for high Reynolds numbers (Bear [2013]). In most cases, macro- or REV-scale simulations compensate for the loss of pore-scale information with relatively low computational costs.

Porosity

The porosity quantifies the ratio of the void pore volume and the total volume of an REV:

$$\Phi = \frac{V_{\text{void space}}}{V_{\text{REV}}} . \quad (2.13)$$

It can be used to convert the seepage velocity v_s in the pores of a porous medium to the REV-scale Darcy velocity via $v_D = \Phi v_s$.

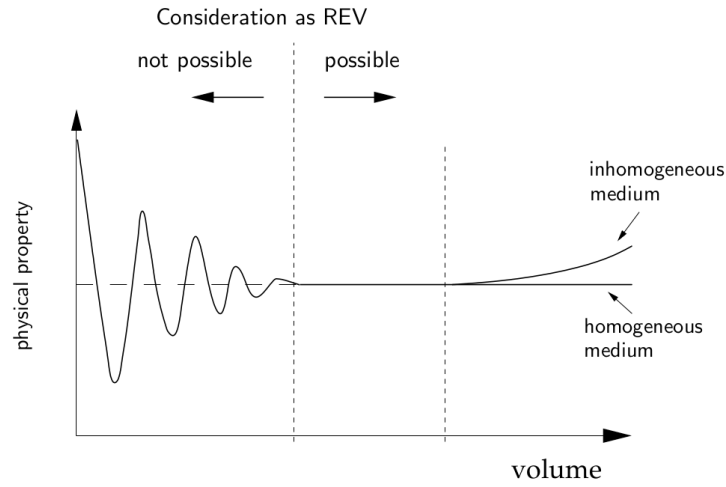


Figure 2.5: Definition of the size of a representative elementary volume (REV) (adapted from Helmig [1997] and Baber [2014])

Intrinsic permeability

Flow in porous media is impeded due to the small diameters of the available flow channels between grains or fibers. On the REV-scale, this impairment is taken into account with the help of the intrinsic permeability \mathbf{K} . Its value has to be determined experimentally for a specific porous medium and might vary in the different spatial directions. For isotropic porous media, it can be described by a scalar quantity K . The REV-scale flow velocity in a porous medium is proportional to the intrinsic permeability.

Saturation

The ratio of fluid volume of phase α and void space can be described by the saturation

$$S_\alpha = \frac{V_\alpha}{V_{\text{void space}}} . \quad (2.14)$$

Since all void space is occupied by some fluid, the saturations sum up to one: $\sum_\alpha S_\alpha = 1$.

Capillary pressure

On the REV-scale, the phase interfaces are not resolved. Consequently, the radii of the curved interfaces are unknown. Therefore, the capillary pressure p_c is parameterized as

a function of the volume-averaged saturation as $p_c(S_w)$ with the help of a constitutive relationship. Two commonly used parameterizations are the Brooks-Corey (Brooks and Corey [1964]) and the van Genuchten (van Genuchten [1980]) models. In the scope of this work, we use a regularized van Genuchten model to avoid the steep gradients for very low and very high saturations. In addition, the capillary pressure itself is defined on the REV-scale as the difference between the phase pressures

$$p_c = p_n - p_w . \quad (2.15)$$

Transferring the capillary pressure definition from pore-scale to macro-scale is not straight forward, as pointed out by Hassanizadeh and Gray [1993]. Equation (2.11) is actually only valid on the phase interface between the two phases, but cannot be derived based on a volumetric averaging approach. Hassanizadeh and Gray [1993] state that by transferring Equation (2.11) directly to the macro-scale, yielding Equation (2.15), the influence of immiscibility, surface tension, fluid-fluid interfaces, viscosity, wettability, grain sizes, heterogeneities, deformation and composition are not taken into account. As an alternative, they present a thermodynamic approach for the definition of capillary pressure.

The capillary pressure caused by the curved liquid-gas interfaces influences the saturated vapor pressure. Above curved surfaces, the vapor pressure is higher than above a flat surface. On the REV-scale, this effect is taken into account in the Kelvin equation as (Galvin [2005]):

$$p_{\text{sat,Kelvin}}^w = p_{\text{sat}}^w \exp\left(-\frac{M^w}{\rho_l RT} p_c\right) . \quad (2.16)$$

However, this is only relevant for high capillary pressures or low saturations of the wetting phase.

Relative permeability

Not only the solid matrix, but also the presence of another fluid influences the flow velocity in a porous medium. In pores filled with two fluids, the wetting phase sticks to the solid walls while the nonwetting phase flows in the center of a pore. This effect is taken into account on the REV-scale by the relative permeability k_r . In addition to the $p_c - S_w$ models, Brooks and Corey [1964] as well as van Genuchten [1980] present constitutive relationships for the relative permeabilities $k_{rw}(S_w)$ and $k_{rn}(S_w)$.

Summary

This chapter provides the physical background for the conceptual models for free flow and flow in porous media. Relevant fluid and wettability properties are described. Additionally, a volume-averaging approach which allows to model flow in porous media on a larger spatial scale is presented.

3 Free flow and flow in porous media

Conceptual and mathematical models describe flow and transport processes with the help of partial differential equations (PDEs) and supplementary closing relations. Due to the lack of pore-scale information and the high computational costs for pore-scale simulations, flow in porous media is modeled on the REV- or macro-scale in the scope of this work. For free-flow scenarios, the same PDEs can be used to describe the processes on the micro-scale as well as on the macro-scale. In this work, we model the coupled system based on a multi-domain approach on the macro-scale to account for the different characteristics of free flow and flow in porous media. Therefore, two separate sets of PDEs are used in the two flow compartments.

We consider the fluids to be compositional and assume nonisothermal conditions everywhere. The balance equations and underlying assumptions are treated in Section 3.1 for free flow and Section 3.2 for flow in porous media respectively.

3.1 Free flow

Free flow is the movement of a fluid through an open space, bounded by a combination of permeable or impermeable walls or a free surface. Boundaries and obstacles influence the velocity, pressure and temperature fields, and therefore fluid properties such as density and viscosity. Within the fluid, flow and transport due to convection, diffusion and conduction take place. Across fluid-solid boundaries, conductive heat transfer can happen.

The following sections give an overview of the free-flow assumptions applied in this work (Section 3.1.1), the balance equations to describe the flow and transport processes (Section 3.1.2) and the influence of boundaries (Section 3.1.3).

3.1.1 Assumptions

We assume a gaseous single-phase free flow consisting of the two components water vapor and air. The components mix according to binary diffusion which can be described by Fick's first law of diffusion. The gas, which mainly consists of air, is assumed to be a compressible ideal gas. We assume laminar flow conditions.

3.1.2 Balance equations

The fundamental physical laws to describe compositional, nonisothermal free flow are Newton's second law, the conservation of total and component mass, and the first law of thermodynamics.

The Navier-Stokes equations are derived from Newton's second law of motion to describe the conservation of momentum:

$$\frac{\partial(\varrho_g \mathbf{v}_g)}{\partial t} + \nabla \cdot (\varrho_g \mathbf{v}_g \mathbf{v}_g^T) = \nabla \cdot (\mu_g (\nabla \mathbf{v}_g + \nabla \mathbf{v}_g^T)) - \nabla p_g + \varrho_g \mathbf{g} . \quad (3.1)$$

The first two terms represent the total derivative $\frac{D(\varrho_g \mathbf{v}_g)}{Dt}$, which describes the changes at a fixed point in time (storage term) and the changes along the fluid's motion (convective flux term). The third term represents the viscous force, which accounts for the friction between the fluid molecules. The last two terms are the pressure and gravitational forces.

The conservation of total mass is ensured by the balance equation

$$\frac{\partial \varrho_g}{\partial t} + \nabla \cdot (\varrho_g \mathbf{v}_g) = q , \quad (3.2)$$

with a storage term, a flux term and a sink or source term q .

For each component κ , a component mass balance can be formulated:

$$\frac{\partial(\varrho_g X_g^\kappa)}{\partial t} + \nabla \cdot (\varrho_g \mathbf{v}_g X_g^\kappa - D_g \varrho_g \nabla X_g^\kappa) = q^\kappa . \quad (3.3)$$

The component flux term represents the advective transport with the flow field as well as the diffusive flux according to the concentration gradient. Since $X_g^w + X_g^a = 1$, summing up both component mass balances yields the total mass balance (3.2).

Describing a nonisothermal system requires an energy balance to account for energy storage and fluxes:

$$\frac{\partial(\varrho_g u_g)}{\partial t} + \nabla \cdot (\varrho_g \mathbf{v}_g h_g - \lambda_g \nabla T) = q^T. \quad (3.4)$$

Here, the flux term consists of the convective heat transport along with the flow field and the conductive heat flux along the temperature gradient ∇T .

This set of equations depends on seven primary variables: the pressure p_g , the velocity components in each dimension $\mathbf{v}_g = (v_{gx}, v_{gy}, v_{gz})^T$, the mass fraction of water X_g^w , the mass fraction of air X_g^a and the temperature T . Due to the relation $X_g^w + X_g^a = 1$, only one of the mass fractions remains a primary unknown and it is sufficient to solve two of the three mass balance equations. In the scope of this work, we solve the two component mass balances according to Equation (3.3). The remaining unknowns are secondary variables and can be computed according to the relations given in Table 2.1.

3.1.3 Boundaries and boundary layers

Defining boundaries and the respective conditions is a challenging task in both experiments and numerical simulations. Boundary conditions are chosen in a way such that they resemble the situation of the desired application. Except for inlet/outlet scenarios, the boundaries should usually not influence the flow behavior within a certain domain, and therefore have to be chosen carefully.

In free-flow scenarios, solid boundaries have a significant impact on the flow field. Nearby permeable and impermeable walls, frictional stress reduces the velocity. This leads to high shear forces close to the wall even for fluids with low viscosities. The resulting areas of slower flow velocities are described by the boundary layer theory. In turbulent flows, the boundary layers consist of a thin laminar viscous sublayer next to the wall, and a turbulent boundary layer between the sublayer and the outer flow field. Details on boundary layer theory can be found in textbooks such as Schlichting and Gersten [2006] or Bird et al. [2007].

Boundary layers do not only form on straight surfaces, but also along wavy surfaces or around obstacles. In the context of coupled free-flow/porous-medium-flow systems, the porous medium represents a permeable wall. On the pore-scale, gas-filled pores, liquid-filled pores and solid matter have to be taken into account to determine the velocity profile at the interface. In addition, drops on the porous surface might influence the boundary layer as obstacles. Their impact depends on their size compared to the channel cross-section available for the free flow. With respect to boundary layers, two different scenarios occur: Drops with heights smaller than the boundary layer as well as drops that are larger and intrude the outer flow field. In the latter case, the drops disturb the outer flow field and partly block the boundary layer flow, leading to additional turbulences.

The influence of a wall on a flow field is expressed with the slip velocity, which is the relative velocity between fluid and wall. Consequently, a slip condition is set at the boundary in case the relative velocity is not zero. If the free-flow velocity decreases to $\mathbf{v}_g = 0$ at the boundary due to viscous effects, a no-slip boundary condition is applied. In the scope of this work, no-slip velocities are assumed at solid walls, while slip conditions are set at the interface with a porous medium. Details for the latter case are given in Section 4.2.

3.2 Flow in porous media

Flow in porous media refers to the movement of fluid through porous materials, which consist of a solid matrix and void spaces. These void spaces can be connected or isolated, and are either filled with liquid or gas. On the pore-scale, each pore can be seen as a free-flow channel which is governed by the physical laws given in Section 3.1. Modeling flow and transport processes on the macro-scale calls for a different treatment, since the flow is hindered by the winding pathways within the solid matrix. In the following, we use an REV-scale averaged approach for the porous medium, which means that the individual pores and structures are not resolved. Definitions of the averaged properties are given in Section 2.2. More details on porous-medium models are amongst others given in the works of Helmig [1997] and Bear [2013].

3.2.1 Assumptions

The solid matrix is assumed to be rigid, nondeformable and isotropic. It is filled with a liquid and a gas phase, each consisting of the two components water and air which mix via binary diffusion (Fick's law). The gas phase is compressible, while the liquid is incompressible. We assume that both fluids show a linear relation between viscosity and shear stress, and therefore behave like a Newtonian fluid. Within the porous medium, local thermodynamic equilibrium between all phases is assumed. With respect to wettability, we assume a hydrophobic porous medium, which means that gas is the wetting phase.

3.2.2 Balance equations

Flow in porous media can be quantified with the conservation of total and component mass as well as the first law of thermodynamics. In addition, the phase velocities can be determined by either Forchheimer's or Darcy's law, depending on the flow conditions.

Forchheimer's law takes inertial forces, which occur for high flow velocities, into account (Ward [1964]):

$$\nabla p_\alpha = \varrho_\alpha \mathbf{g} - \frac{1}{\mathbf{K}} \frac{\mu_\alpha}{k_{r\alpha}} \mathbf{v}_\alpha - \frac{1}{\sqrt{\mathbf{K}}} \frac{\varrho_\alpha c_F}{\eta_{r\alpha}} \mathbf{v}_\alpha |\mathbf{v}_\alpha|. \quad (3.5)$$

For creeping flows with Reynolds numbers smaller than one, the nonlinear term can be neglected, yielding Darcy's law (see e. g. Helmig [1997]):

$$\nabla p_\alpha = \varrho_\alpha \mathbf{g} - \frac{1}{\mathbf{K}} \frac{\mu_\alpha}{k_{r\alpha}} \mathbf{v}_\alpha. \quad (3.6)$$

Since we assume creeping flows ($\text{Re} < 1$), we use Darcy's law, which can be rearranged to an equation for the phase velocity, which is also called Darcy velocity:

$$\mathbf{v}_\alpha = -\mathbf{K} \frac{k_{r\alpha}}{\mu_\alpha} (\nabla p_\alpha - \varrho_\alpha \mathbf{g}). \quad (3.7)$$

The mass balance for the porous medium is given by the equation

$$\sum_\alpha \Phi \frac{\partial(\varrho_\alpha S_\alpha)}{\partial t} + \nabla \cdot \left(\sum_\alpha (\varrho_\alpha \mathbf{v}_\alpha) \right) = \sum_\alpha q_\alpha. \quad (3.8)$$

The fact that only a volume fraction of the porous medium is available for the fluids is accounted for by multiplying the storage term with the porosity Φ . The presence of the two fluid phases is taken into account by the saturation S_α in the storage term. With Equation (3.7), the velocity can be plugged into the mass balance equation to compute the advective fluxes.

In addition to the total mass balance, a component mass balance is required for each component κ :

$$\sum_{\alpha} \Phi \frac{\partial(\varrho_{\alpha} X_{\alpha}^{\kappa} S_{\alpha})}{\partial t} + \nabla \cdot \left(\sum_{\alpha} (\varrho_{\alpha} \mathbf{v}_{\alpha} X_{\alpha}^{\kappa} - D_{\alpha}^{\text{pm}} \varrho_{\alpha} \nabla X_{\alpha}^{\kappa}) \right) = \sum_{\alpha} q_{\alpha}^{\kappa}. \quad (3.9)$$

The first term represents the storage, the second term describes the flux by advection and diffusion, and the last term is a sink/source term.

For a nonisothermal system, the conservation of energy has to be guaranteed by solving an energy equation. Due to the assumption of local thermodynamic equilibrium, the temperature within the porous medium is assumed to be equal locally across the phase interfaces: $T_s = T_g = T_l = T$. Therefore, one energy balance is sufficient for the porous medium:

$$\sum_{\alpha} \Phi \frac{\partial(\varrho_{\alpha} u_{\alpha} S_{\alpha})}{\partial t} + (1 - \Phi) \frac{\partial(\varrho_s c_s T)}{\partial t} + \nabla \cdot \left(\sum_{\alpha} (\varrho_{\alpha} h_{\alpha} \mathbf{v}_{\alpha} - \lambda_{\text{pm}} \nabla T) \right) = q_T. \quad (3.10)$$

Here, the first term describes the storage within the fluids, while the second term represents the heat storage within the solid matrix. The flux term consists of a convective and a conductive part.

3.2.3 Additional relations

The system of partial differential equations for total mass, water mass, air mass and energy contains the unknowns $p_g, p_l, S_l, S_g, X_g^w, X_g^a, X_l^w, X_l^a, h_l, h_g, u_g, u_l$ and T . We choose the primary unknowns to be p_g, S_l and T , if both fluid phases are present. If the liquid phase disappears, the primary variable S_l switches to X_g^w as suggested by Class et al. [2002].

The pressure p_g and the saturation S_l are obtained by solving the two component mass balances given in Equation 3.9. Solving the energy equation (3.10) yields the temperature

T. The remaining unknowns are therefore secondary variables and need to be determined with the help of supplementary relations and constitutive relationships, which are explained in Section 2.2.

The phase pressures are linked to each other via the capillary pressure $p_c = p_n - p_w$, where n corresponds to the nonwetting and w to the wetting phase. The capillary pressure itself is determined by the saturation S_w via the $p_c - S_w$ relationship. In the scope of this work, the model by van Genuchten [1980] is used for the $p_c - S_w$ as well as the $k_r - S_w$ relationships.

The gas-phase saturation S_g is given by the relation $S_g + S_l = 1$.

The mass fractions X_α^κ are computed with Dalton's and Henry's law.

The specific enthalpies h_α as well as the specific internal energies u_α are obtained with the relations given in Table 2.1.

In contrast to the free flow, the flow velocity \mathbf{v}_α in the porous medium can be computed as a secondary variable with Equation (3.7).

Summary

This chapter introduces the model concepts to describe free flow and flow in porous media on the macro-scale. We use the Navier-Stokes equations for the momentum conservation in the free-flow domain. In the porous medium, Darcy's law is applied to compute the phase velocities.

4 Coupling concept without drops

Modeling the interactions and transfer processes between a free flow and a flow in a porous medium requires a coupling concept. Even though the interface region is small compared to the flow compartments on both sides, its structure and the occurring pore-scale processes strongly influence the transfer of mass, momentum and energy between the compartments. Since the two flow compartments can often be modeled on the REV-scale, the coupling concept should be based on volume-averaged quantities as well, but still account for the pore-scale processes.

In this chapter, a simple coupling concept which neglects the influence of drops is introduced. This approach is presented by Mosthaf et al. [2011] and assumes an interface devoid of thermodynamic properties, which means it cannot store mass, momentum or energy. Therefore, the conditions on both sides of the interface have to be continuous, i. e. they have to guarantee the continuity of fluxes across the interface.

We first provide pore-scale considerations concerning the fluxes and normal forces at the interface between a free flow and a flow in a porous medium in Section 4.1. The full derivation of a macro-scale coupling concept based on the pore-scale processes is presented in detail by Mosthaf et al. [2011] and will therefore be omitted in this work. However, the resulting macro-scale concept is explained in Section 4.2. The numerical model to solve a coupled system consisting of the balance equations given in Chapter 3 combined with the coupling conditions in this chapter is described in Section 4.3.

4.1 Pore-scale considerations

In the following, the interface between a free flow and a flow in a porous medium is assumed to be a bundle of tubes which consists of several parallel pores next to each other. The pores can have different radii but are assumed to have the same length δ .

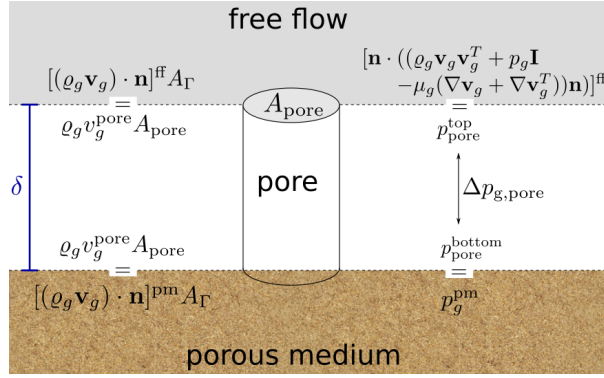


Figure 4.1: Continuity of fluxes and force balance for the gas phase in a single pore

Each pore is connected to the pore space in the porous medium below as well as to the free flow above. A similar derivation is also presented by Baber [2014].

We first consider a single pore as shown in Figure 4.1. The pore is connected to a gas reservoir in the porous medium below as well as to a gaseous free flow above. If the pressures p_g^{ff} and p_g^{pm} differ, a gas flux through the pore towards the region with lower pressure is established. Under the assumption of laminar flow and an incompressible Newtonian fluid, the flow velocity through the pore can be described with the Hagen-Poiseuille law:

$$v_g^{\text{pore}} = \frac{(r_{\text{pore}})^2 \Delta p_g^{\text{pore}}}{8\mu_g \delta}, \quad (4.1)$$

with the pressure difference

$$\Delta p_g^{\text{pore}} = p_g^{\text{pore,top}} - p_g^{\text{pore,bottom}}. \quad (4.2)$$

The gaseous mass flux coming from the porous medium and reaching the lower end of the pore is given as

$$q^{\text{pm}} = [(\rho_g \mathbf{v}_g) \cdot \mathbf{n}]^{\text{pm}} A_\Gamma. \quad (4.3)$$

Due to continuity of fluxes, it has to be equal to the mass flux within the pore

$$q^{\text{pm}} = q^{\text{pore}} = \rho_g v_g^{\text{pore}} A_{\text{pore}}, \quad (4.4)$$

which then has to be equal to the mass flux into the free flow at the top of the pore

$$q^{\text{pm}} = q^{\text{pore}} = q^{\text{ff}} = [(\rho_g \mathbf{v}_g) \cdot \mathbf{n}]^{\text{ff}} A_\Gamma. \quad (4.5)$$

The continuity of mass fluxes on both sides of the pore can then be described as

$$[(\varrho_g \mathbf{v}_g) \cdot \mathbf{n}]^{\text{pm}} = [(\varrho_g \mathbf{v}_g) \cdot \mathbf{n}]^{\text{ff}} . \quad (4.6)$$

For mechanical equilibrium, the normal forces exerted by the free flow and the flow in the porous medium on both pore ends have to be taken into account. Within the pore, the pressure difference is described on the pore-scale with the help of the Hagen-Poiseuille equation:

$$\Delta p_g^{\text{pore}} = \frac{8\mu_g \delta v_g^{\text{pore}}}{(r_{\text{pore}})^2} . \quad (4.7)$$

Due to the motion of the fluid on the free-flow side, viscous effects have to be taken into account here as well. At the upper end of the pore, the pore-scale pressure p_g^{top} counters the free-flow forces:

$$[\mathbf{n} \cdot ((\varrho_g \mathbf{v}_g \mathbf{v}_g^T + p_g \mathbf{I} - \mu_g (\nabla \mathbf{v}_g + \nabla \mathbf{v}_g^T)) \mathbf{n})]^{\text{ff}} = [p_g^{\text{top}}]^{\text{pore}} . \quad (4.8)$$

According to Equation (4.2), the pressure at the upper end of the pore is given as

$$p_g^{\text{pore, top}} = \Delta p_g^{\text{pore}} + p_g^{\text{pore, bottom}} . \quad (4.9)$$

In the following, we assume that the pore-scale pressure at the bottom of the pore $p_g^{\text{pore, bottom}}$ is equal to the macro-scale pressure in the porous medium p_g^{pm} :

$$p_g^{\text{pore, bottom}} = p_g^{\text{pm}} . \quad (4.10)$$

With these equilibrium conditions, the normal mechanical equilibrium between free flow and flow in a porous medium can be written as

$$[\mathbf{n} \cdot ((\varrho_g \mathbf{v}_g \mathbf{v}_g^T + p_g \mathbf{I} - \mu_g (\nabla \mathbf{v}_g + \nabla \mathbf{v}_g^T)) \mathbf{n})]^{\text{ff}} A_{\text{pore}} = (\Delta p_g^{\text{pore}} + p_g^{\text{pm}}) A_{\text{pore}} . \quad (4.11)$$

The pore velocity v_g^{pore} for the pressure difference Δp_g^{pore} results from the continuity of mass fluxes in Equation (4.4):

$$v_g^{\text{pore}} = \frac{[\mathbf{v}_g \cdot \mathbf{n}]^{\text{pm}} A_{\Gamma}}{\pi (r_{\text{pore}})^2} . \quad (4.12)$$

In summary, Equations (4.6) and (4.11) describe the continuity of mass fluxes and the balance of normal forces respectively on the REV-scale under the influence of the pore-scale pressure within the pore if only the gas phase is present.

For a bundle of tubes, the contributions from the individual pores have to be summed up. Under the assumptions of a Poiseuille flow, constant velocities along δ and negligible gravitational effects, the pressure difference in all pores is equal, while the fluxes differ.

The mass flux through the bundle of tubes is now given as the sum of the individual pore mass fluxes:

$$q^{\text{tubes}} = \Phi \sum_{\bar{r}_{\text{pore}}} \underbrace{\frac{(\bar{r}_{\text{pore}})^2 \Delta p_g^{\text{pore}}}{8\mu_g \delta}}_{v_g^{\text{pore}}} \varrho_g \pi (\bar{r}_{\text{pore}})^2 n_{\bar{r}_{\text{pore}}} . \quad (4.13)$$

To transfer the pore-scale mass fluxes to the REV-scale, the pore velocity v_g^{pore} (4.1) is multiplied with the porosity Φ , which yields the REV-scale velocity $v_g = \Phi v_g^{\text{pore}}$. For the continuity of mass fluxes, Equation (4.6) remains valid since $q^{\text{ff}} = q^{\text{tubes}} = q^{\text{pm}}$.

Balancing the normal forces also yields Equation (4.11), with the pressure difference now given as

$$\Delta p_g^{\text{pore}} = \frac{[\varrho_g \mathbf{v}_g \cdot \mathbf{n}]^{\text{pm}} A_{\Gamma} \delta}{\Phi \sum_{\bar{r}_{\text{pore}}} \frac{(\bar{r}_{\text{pore}})^2}{8\mu_g} \varrho_g \pi (\bar{r}_{\text{pore}})^2 n_{\bar{r}_{\text{pore}}}} . \quad (4.14)$$

Consequently, Equations (4.6) and (4.11) remain valid for a bundle of tubes with the adaptations given in Equations (4.13) and (4.14).

In case of a two-phase flow in the porous medium, the balance between liquid-filled pores and the gaseous free flow has to be taken into account as well. Following the assumptions by Mosthaf et al. [2011], the liquid phase evaporates immediately when it reaches the interface. Therefore, the continuity of mass fluxes can directly be written as a balance of the REV-scale quantities above and below the bundle of tubes:

$$[(\varrho_g \mathbf{v}_g + \varrho_l \mathbf{v}_l) \cdot \mathbf{n}]^{\text{pm}} = [(\varrho_g \mathbf{v}_g) \cdot \mathbf{n}]^{\text{ff}} . \quad (4.15)$$

For mechanical equilibrium, the capillary pressure p_c has to be taken into account. In a hydrophobic porous medium, it is defined as $p_c = p_l - p_g$, which can be reformulated as $p_l - p_c = p_g$. Therefore, the force $(p_l - p_c)A_{\text{pore}} = p_g A_{\text{pore}}$ acts on the interface between

pore and free flow. For the bundle of tubes, the normal force balance is consequently given as

$$\begin{aligned} & \left[\mathbf{n} \cdot \left((\rho_g \mathbf{v}_g \mathbf{v}_g^T + p_g \mathbf{I} - \mu_g (\nabla \mathbf{v}_g + \nabla \mathbf{v}_g^T)) \mathbf{n} \right) \right]^{\text{ff}} A_\Gamma \\ &= \sum_{\text{gas}} p_g^{\text{pore,top}} A_{\text{pore}} + \sum_{\text{liq}} (p_l^{\text{pore,top}} - p_c) A_{\text{pore}} = \sum_{\text{all}} p_g^{\text{pore,top}} A_{\text{pore}} . \end{aligned} \quad (4.16)$$

As mentioned before, a detailed derivation based on the pore-scale processes is given by Mosthaf et al. [2011] and Baber [2014]. The resulting macro-scale equations are presented in the next section.

4.2 Macro-scale coupling concept

On the macro-scale, the interface between a free flow and a porous medium is assumed to be a sharp border which clearly separates the two regimes. Across this sharp interface, a transfer of mass, momentum and energy takes place. The interface has to be treated as an interior boundary within the global model domain. Consequently, appropriate boundary conditions have to be formulated.

Developing such conditions poses different challenges. Since the velocity is a primary variable in the free flow but not in the porous medium, a respective coupling condition needs to be set only at the free-flow side of the interface. Furthermore, the pressure appears in a second-order term in the porous-medium mass balance equation, but is only differentiated once in the respective free-flow equation. Additionally, possibly large differences between the two coupled systems with respect to the spatial and temporal scales have to be bridged.

Figure 4.2 shows an exemplary model domain for such coupled systems. The model domain Ω consists of the two non-overlapping sub-domains Ω^{ff} and Ω^{pm} . The interface Γ separates the subdomains such that $\bar{\Omega} = \bar{\Omega}^{\text{ff}} \cup \bar{\Omega}^{\text{pm}}$, $\Omega^{\text{ff}} \cap \Omega^{\text{pm}} = \emptyset$ and $\bar{\Omega}^{\text{ff}} \cap \bar{\Omega}^{\text{pm}} = \Gamma$. The respective outer boundaries are denoted as Γ^{ff} and Γ^{pm} .

As stated by Mosthaf et al. [2011], the simple coupling concept is based on the assumption of local thermodynamic equilibrium at the interface. Even though the equilibrium cannot rigorously be achieved, this assumption allows to apply a concept that corresponds to

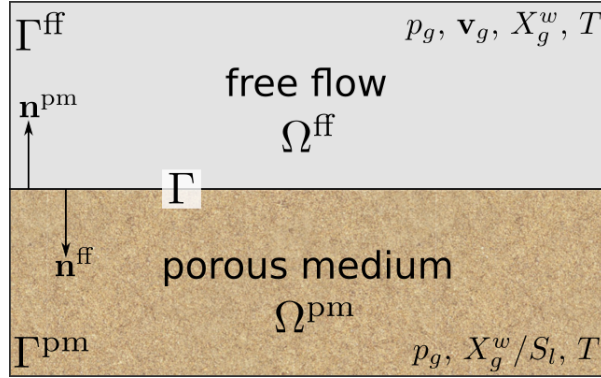


Figure 4.2: Exemplary model domain Ω with the respective primary variables and normal vectors for Ω^{ff} and Ω^{pm}

phenomenological explanations. In the following, we discuss the components which make up thermodynamic equilibrium: mechanical, chemical and thermal equilibrium.

4.2.1 Mechanical equilibrium

For local mechanical equilibrium, the forces acting on the interface from both sides have to balance out and the mass fluxes across the interface have to be continuous. The forces acting on the interface can be decomposed into a normal and a tangential contribution. From the free-flow side, the normal inertial forces $(\rho_g \mathbf{v}_g \mathbf{v}_g^T) \mathbf{n}$ as well as the normal shear stress

$$\boldsymbol{\sigma} \mathbf{n} = (-p_g \mathbf{I} + \mu_g (\nabla \mathbf{v}_g + \nabla \mathbf{v}_g^T)) \mathbf{n} . \quad (4.17)$$

act on the interface.

From the porous-medium side, the pressure and the viscous forces exerted by the flow field act on the interface. Since the viscous forces are already accounted for in the Darcy velocity $\mathbf{v}_\alpha^{\text{pm}}$, only the phase pressures balance out the forces from the free-flow side.

In contrast to a hydrophilic porous medium in Mosthaf et al. [2011], we assume the porous medium to be hydrophobic. Therefore, the capillary pressure is given as $p_c = p_l - p_g$. On top of the water-filled pores, the capillary pressure p_c works against the liquid pressure p_l inside the porous medium. The resulting pressure in liquid-filled pores is then $p_l - p_c = p_g$, which is equal to the pressure in the gas-filled pores. Consequently, the gas pressure p_g acts on the whole interface area from the porous-medium side and the macro-scale

condition for a hydrophobic porous medium is given as

$$\left[\mathbf{n} \cdot \left((\varrho_g \mathbf{v}_g \mathbf{v}_g^T + p_g \mathbf{I} - \mu_g (\nabla \mathbf{v}_g + \nabla \mathbf{v}_g^T)) \mathbf{n} \right) \right]^{\text{ff}} = [p_g]^{\text{pm}}. \quad (4.18)$$

Tangential forces

In most cases, the tangential flow velocities in the free flow and the porous medium differ significantly. Therefore, describing a continuous velocity profile across the interface is challenging. As already mentioned in Section 3.1, a no-slip condition could be set for the tangential free-flow velocity. This would result in a parabolic velocity profile in the free-flow domain, with the tangential velocity $v_{g,t}^{\text{ff}} = 0$ at the interface.

Beavers and Joseph [1967] proposed a condition to link the two velocities and obtain a continuous velocity profile:

$$\left[\left(-\frac{\sqrt{k_i}}{\alpha_{BJ}} (\nabla \mathbf{v}_g + \nabla \mathbf{v}_g^T) \mathbf{n} - \mathbf{v}_g \right) \cdot \mathbf{t}_i \right]^{\text{ff}} = [-\mathbf{v}_g \cdot \mathbf{t}_i]^{\text{pm}}, \quad (4.19)$$

where \mathbf{t}_i are the tangential vectors along the interface in each dimension i and $k_i = (\mathbf{K} \mathbf{t}_i) \cdot \mathbf{t}_i$ is the corresponding component of the porous-medium permeability.

However, Saffman [1971] states that the small tangential velocities within the porous medium can be neglected, leading to the Beavers-Joseph-Saffman condition

$$\left[\left(\mathbf{v}_g + \frac{\sqrt{k_i}}{\alpha_{BJ}} (\nabla \mathbf{v}_g + \nabla \mathbf{v}_g^T) \mathbf{n} \right) \cdot \mathbf{t}_i \right]^{\text{ff}} = 0. \quad (4.20)$$

This equation does not depend on the porous-medium flow anymore and can therefore be used as a boundary condition for the tangential free-flow velocity. The Beavers-Joseph coefficient α_{BJ} has to be determined numerically or experimentally.

Continuity of normal mass fluxes

Since the interface cannot store mass, the mass fluxes across the interface have to sum up to zero. In the presented approach, the liquid phase is assumed to evaporate directly into the gaseous free flow when it reaches the interface:

$$[(\varrho_g \mathbf{v}_g) \cdot \mathbf{n}]^{\text{ff}} = -[(\varrho_g \mathbf{v}_g + \varrho_l \mathbf{v}_l) \cdot \mathbf{n}]^{\text{pm}}. \quad (4.21)$$

The specific enthalpy of the vaporization is then accounted for in the balance of heat fluxes.

4.2.2 Thermal equilibrium

Thermal equilibrium is given when the temperature as well as the corresponding normal heat fluxes are continuous at the interface.

Continuity of temperature

Due to the assumption of local thermodynamic equilibrium within the porous medium, all three phases are in thermal equilibrium and have the same temperature: $T_s^{\text{pm}} = T_g^{\text{pm}} = T_l^{\text{pm}} = T^{\text{pm}}$. For thermal equilibrium at the interface, the temperatures on both sides have to be equal. Since this cannot always be guaranteed, we assume

$$[T]^{\text{ff}} \approx [T]^{\text{pm}} . \quad (4.22)$$

Continuity of normal heat fluxes

The associated normal heat fluxes are given as

$$[(\varrho_g h_g \mathbf{v}_g - \lambda_g \nabla T) \cdot \mathbf{n}]^{\text{ff}} = - \left[\left(\sum_{\alpha} \varrho_{\alpha} h_{\alpha} \mathbf{v}_{\alpha} - \lambda^{\text{pm}} \nabla T \right) \cdot \mathbf{n} \right]^{\text{pm}} . \quad (4.23)$$

The specific vaporization enthalpy of the liquid phase is taken into account in the convective heat flux $\varrho_l h_l \mathbf{v}_l$.

4.2.3 Chemical equilibrium

Chemical equilibrium is given when all reaction rates are equal in the two opposite directions. As a consequence, the macro-scale parameters of a system in chemical equilibrium do not change and the concentrations are constant.

Continuity of chemical potential

On the pore-scale, chemical equilibrium refers to an equilibrium of the chemical potentials. However, in the case of a coupled free-flow/porous-medium-flow system, the continuity of the chemical potentials across the interface cannot be guaranteed on the macro-scale due to the possible pressure jump resulting from condition (4.18). Therefore, Mosthaf et al. [2011] use a condition for the mole fractions, even though it might not always be fulfilled and could lead to a jump in the chemical potential across the interface. We convert the proposed condition into the continuity of mass fractions to match the choice of primary variables in our system:

$$[X_g^\kappa]^{\text{ff}} \approx [X_g^\kappa]^{\text{pm}} . \quad (4.24)$$

Continuity of normal component mass fluxes

The respective normal component mass fluxes for $\kappa \in \{a, g\}$ are

$$\left[(\varrho_g X_g^\kappa \mathbf{v}_g - D_g \varrho_g \nabla X_g^\kappa) \cdot \mathbf{n} \right]^{\text{ff}} = - \left[\sum_{\alpha} (\varrho_{\alpha} X_{\alpha}^{\kappa} \mathbf{v}_{\alpha} - D_{\alpha}^{\text{pm}} \varrho_{\alpha} \nabla X_{\alpha}^{\kappa}) \cdot \mathbf{n} \right]^{\text{pm}} . \quad (4.25)$$

Again, direct evaporation of the liquid phase is assumed at the coupling interface. Out of the three mass coupling conditions (4.21) and (4.25), two are sufficient to describe the normal mass fluxes across the interface. The choice depends on the mass balance equations which are solved in the subdomains.

With all of these conditions we can describe the exchange processes between a free flow and a flow in a porous medium. The next step towards a simulation is the discretization of the respective equations and the implementation of the coupling conditions.

4.3 Numerical model

For certain simple set-ups, analytic solutions exist for Navier-Stokes as well as Darcy problems. A solution for a single-phase coupled problem is constructed by Chidyagwai and Rivière [2011]. However, due to their complexity and high nonlinearity, no analytic

solutions exist for realistic coupled free-flow/porous-medium-flow problems. Therefore, we solve the coupled system numerically.

To do so, we apply separate discretizations in time and space. The respective discretizations used within this work are explained in Section 4.3.1. In Section 4.3.2, we describe how the arising system of nonlinear equations is solved. Details on the used software are presented in Section 4.3.3.

4.3.1 Discretization

A general form of the continuous balance equations can be written as

$$\frac{\partial \mathbf{M}(\mathbf{u})}{\partial t} + \nabla \cdot \mathbf{F}(\mathbf{u}) = \mathbf{Q}(\mathbf{u}) , \quad (4.26)$$

where \mathbf{u} is the vector of unknowns (solution vector), \mathbf{M} is the storage, \mathbf{F} the flux and \mathbf{Q} the source term. The vector \mathbf{u} contains all unknowns of the respective subdomain.

Discrete versions of the continuous equations are obtained by covering the model domain with a grid and defining discrete points where the variables are evaluated and stored. The grid divides the domain into N cells Ω_i , $i \in 0, \dots, N-1$. In the scope of this work, we assume non-overlapping grid cells and apply finite-volume based discretizations in space. The grid cells correspond to control volumes over which the equations are integrated. Integrating over the grid cells Ω_i and applying the Gauß theorem for the flux term yields

$$\int_{\Omega_i} \frac{\partial \mathbf{M}(\mathbf{u})}{\partial t} dV + \int_{\Gamma_i} (\mathbf{F}(\mathbf{u}) \cdot \mathbf{n}) dA = \int_{\Omega_i} \mathbf{Q}(\mathbf{u}) dV . \quad (4.27)$$

This formulation states that the change of \mathbf{u} over time within Ω_i , the normal fluxes across the boundary Γ_i and the sink or source terms within Ω_i have to balance out. Since \mathbf{n} is the outer unit normal vector of Γ_i , the outflow of Ω_i across Γ_i is equal to the inflow into a neighboring element Ω_j , whose cell edge Γ_j coincides with Γ_i . We apply an upwinding scheme for the advective terms between two cells, i. e. the upstream value is used to evaluate the respective flux. The diffusive and conductive terms are averaged between the corresponding grid cells.

In the following, the two different spatial discretization schemes which are applied for the free-flow as well as the porous-medium-flow domain are explained.

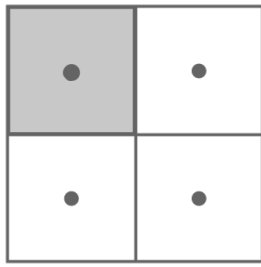
Cell-centered two-point flux approximation (CCTPFA)

In a cell-centered finite-volume method, all variables are computed and stored in the cell centers as shown in Figure 4.3a. The set of all unknowns in all cell centers are the degrees of freedom of the system. We use a two-point flux approximation which only takes the values of the two neighboring cells into account when computing the flux contribution, i. e. gradients are always computed between two cell centers at the midpoints of the respective grid edge. This method is fast for structured, rectangular grids but leads to unstable results for unstructured grids. For such grids, a multi-point flux approximation should be considered, as e. g. suggested by Wolff et al. [2013]. For high flow velocities, pressure oscillations might occur because the driving force for the advective flow, the pressure gradient, is computed at the same location as the resulting flow velocity. Therefore, the CCTPFA method is only suited for slow flow velocities, such as the ones occurring in porous media. It is robust and monotone, but only consistent if the directions of the permeability tensor are aligned with the distance vectors between the cell centers and cell faces (Heinemann et al. [1989]).

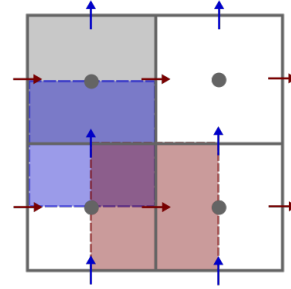
Since we use only rectangularly meshed grids, the two-point flux approximation is sufficient for our numerical examples and will be used in the porous-medium subdomain.

Staggered grid

For larger flow velocities, e. g. in free-flow problems, the staggered grid method provides a suitable alternative. Harlow and Welch [1965] present the marker-and-cell (MAC) scheme, where the velocity components v_i and their respective control volumes are shifted by half a cell away from the cell centers as shown in Figure 4.3b. With this method, pressure oscillations are avoided because the fluxes between the grid cells are then evaluated at the cell edges with the respective velocity components. All scalar primary and secondary variables are still evaluated and stored at the cell centers. The staggered grid is only suited for structured grids. However, it is a robust and mass-conservative scheme. A detailed error analysis for the staggered grid is presented amongst others by Nicolaides [1992] and Nicolaides and Wu [1996]. In the scope of this work, we use the staggered grid for the spatial discretization of the free-flow subdomain.



(a) Grid cells for the cell-centered two-point flux approximation



(b) Grid cells for the staggered grid with shifted control volumes

Figure 4.3: Spatial discretization schemes

Coupling CCTPFA and staggered grid

Evaluating the coupling conditions (Section 4.2) on the interface where the CCTPFA and the staggered grid meet, requires conform grids on both sides of the interface. In the scope of this work, we use rectangular grids only and follow the approach by Fetzer et al. [2017]. For the calculation of the advective fluxes on the free-flow side, the respective velocity components which are given directly on the face edges are used. On the porous medium side, the gas pressure gradient across the interface between the center of the porous-medium cell as well as the center in the free-flow cell is computed. Due to the assumption of a single-phase gaseous free flow, no liquid pressure gradient can be computed at the interface. As mentioned before, all liquid that reaches the upper row of porous-medium cells is assumed to evaporate directly into the free flow.

Temporal discretization

The spatial discretization leads to a system of ordinary differential equations with respect to time. Similar to the spatial grid, a temporal grid with discrete points in time is used to evaluate this system. We use a fully-implicit Euler method, which applies a backward finite-difference to the storage term:

$$\frac{\partial \mathbf{M}(\mathbf{u}^{n+1})}{\partial t} \approx \frac{\mathbf{M}(\mathbf{u}^{n+1}) - \mathbf{M}(\mathbf{u}^n)}{\Delta t^{n+1}}. \quad (4.28)$$

The time step size might vary since it is determined by the convergence of the Newton solver as described in the next section.

In coupled systems, the flow processes might occur on different temporal scales. Especially in the case of a porous medium coupled to a free flow, the difference in the temporal scales can be large. Typical free-flow applications with high flow velocities operate on time scales of seconds, while flow processes in porous media often take hours or days. Therefore, either a compromise with respect to the time-stepping scheme has to be found, or a multi-rate approach such as the one presented by Rybak et al. [2015] has to be applied.

4.3.2 Solving the nonlinear system

Solving a continuous equation in a discrete way inevitably leads to inaccuracies. Therefore, a local residual vector \mathbf{r} which contains the discrepancies from the original equation is defined with Equation (4.26) as

$$\mathbf{r} := \frac{\partial \mathbf{M}(\mathbf{u})}{\partial t} + \nabla \cdot \mathbf{F}(\mathbf{u}) - \mathbf{Q}(\mathbf{u}) , \quad (4.29)$$

where all quantities on the right-hand side correspond to the discrete versions.

Assembling the balance equations given in Sections 3.1 and 3.2, and combining them with the coupling conditions presented in Section 4.2 results in a global system of nonlinear partial differential equations of the form

$$\mathbf{J}(\mathbf{u}) \cdot \mathbf{u} = \mathbf{R} , \quad (4.30)$$

where \mathbf{J} is the global Jacobian matrix, \mathbf{u} the global vector of unknowns and \mathbf{R} the global residual vector.

In a monolithic approach, the global Jacobian matrix \mathbf{J} consists of four submatrices as shown in Figure 4.4: two matrices on the diagonal for the free-flow and porous-medium domains respectively, and two coupling matrices on the off-diagonal which contain the entries according to the coupling conditions. The coupling matrices are sparse, because not all primary variables in the two subdomains are linked to each other via coupling conditions. Furthermore, each submatrix is made up of the submatrices of the individual grid elements, whose local residuals \mathbf{r} are obtained sequentially and finally assembled into the global residual vector \mathbf{R} and Jacobian matrix \mathbf{J} .

FF	FF/PM
PM/FF	PM

Figure 4.4: Schematic representation of the Jacobian matrix for the coupled system

The nonlinear system can be solved by applying a standard iterative Newton scheme:

$$\underbrace{\left(\frac{\partial \mathbf{R}}{\partial \mathbf{t}}\right)^{n+1,m}}_{\mathbf{J}(\mathbf{u}^{n+1,m})} \underbrace{(\mathbf{u}^{n+1,m} - \mathbf{u}^{n+1,m-1})}_{\Delta \mathbf{u}} = -\mathbf{R}(\mathbf{u}^{n+1,m}). \quad (4.31)$$

The Jacobian matrix $\mathbf{J}(\mathbf{u}^{n+1,m})$ is assembled in each Newton step m and obtained by numerical differentiation. The emerging linear system $\mathbf{J}(\mathbf{u}^{n+1,m})\Delta \mathbf{u} = -\mathbf{R}(\mathbf{u}^{n+1,m})$ is solved for $\Delta \mathbf{u}$ with a direct linear solver. The difference $\Delta \mathbf{u}$ in Equation (4.31) refers to the correction of the solution vector from the last Newton step ($m - 1$) to the current one (m). The superscript $n + 1$ illustrates that the converged solution of Equation (4.31) is the initial solution for the next time step.

The Newton scheme is considered to be converged as soon as the difference between two subsequent solutions $\Delta \mathbf{u}$ is smaller than a given threshold.

The time step size is varied depending on the convergence of the Newton solver. If the solver does not converge for a certain time step, the time step size is reduced several times if necessary, until convergence is reached or a maximum number of reductions has been carried out.

4.3.3 Implementation

The numerical model is implemented in DuMu^x (DUNE for Multi-Phase, Component, Scale, Physics, ...), a free and open-source simulator for multi-phase flow and transport processes in porous media and free-flow scenarios. It is written in an object-oriented style of C++ and depends on the Distributed and Unified Numerics Environment DUNE (Blatt et al. [2016]). DuMu^x is implemented in the form of a DUNE module, and can itself be extended by further modules. DuMu^x provides implementations of several free-flow and porous-medium-flow models, each with the option of isothermal/nonisothermal

conditions and immiscible/compositional fluids. Various fluid systems, material laws and parameterizations are available to tailor a model for a specific application. In addition, it offers several discretization methods and allows the implementation of multi-domain problems. The core code is mainly developed and used at the Department of Hydromechanics and Modelling of Hydrosystems at the University of Stuttgart, Germany. Current information, updates and the documentation of DuMu^x can be found at <http://dumux.org>.

For the grid, the tensor-grid mode of DUNE-GRID's YaspGrid (Bastian et al. [2008]) is used, which allows a gradual grid refinement in any direction. The monolithic linear system is solved with DUNE-ISTL (Blatt and Bastian [2007]) and the direct solver UMFPack (Davis [2004]).

Summary

In this chapter, we present a simple coupling approach for the exchange of mass, momentum and energy which is based on the assumption of local thermodynamic equilibrium. The simple coupling concept does not take drops into account. Pore-scale considerations with respect to the transfer processes are presented first, followed by a macro-scale concept. Furthermore, the respective discretizations and a solution strategy for the global system of equations for the coupled free-flow/porous-medium-flow system are explained.

5 Drops

In the following, we discuss the theory of drops based on the continuum approach. Drops are small round-shaped accumulations of a liquid substance hold together by surface tension and separated from the surrounding phases by a sharp interface. Under equilibrium conditions, they take on a spherical shape to minimize the surface energy. Drops occur in different phase combinations, e. g. in contact with solid surfaces as sessile or pending drops, in gaseous phases (e. g. as sprays and rain), as well as in immiscible two-phase liquids (e. g. emulsions).

In the scope of this work, we are interested in water drops which form on top of a hydrophobic porous surface and are surrounded by air. If the liquid mass flux from the porous medium below is sufficiently large, the drops grow. Otherwise, they might shrink due to evaporation or penetrate back into the pores. Drops might also form on a solid surface due to condensation out of saturated gas as well as due to the impact and splashing of falling drops. However, the latter case is neglected in this work.

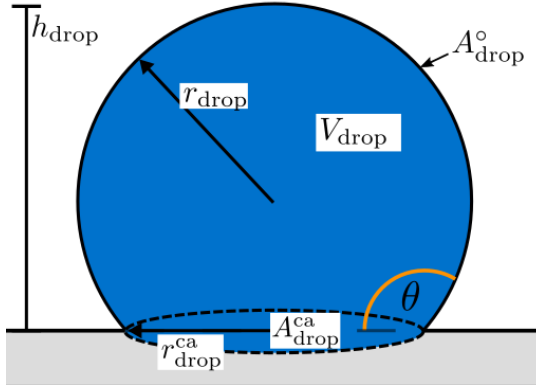
In many technical applications, drops are small compared to the rest of the system. In most cases, the total amount of water mass is of greater interest than the drops' individual sizes and exact shapes. Often, the distribution, existence or movement of drops in general is more decisive for the performance than the development, growth and detachment of one single drop. For example, water drops grow and eventually merge in the gas channels of fuel cells. The resulting liquid water film then blocks the reaction between oxygen and hydrogen. Even though understanding the behavior of the individual drops helps to improve such systems, the overall water mass is significant for the cell's performance. Nevertheless, we have to begin at the pore-scale to understand the occurring processes and derive models from the behavior of a single drop. Later on, the pore-scale knowledge can be transferred to a larger spatial scale in order to obtain conceptual models for the huge amount of drops found on surfaces and interfaces in applications.

In the following, we examine the behavior of one drop depending on the surrounding conditions and use it as a template for the many other drops that form under the same or similar conditions. Based on these considerations, we develop coupling concepts to investigate the influence of drops on the exchange processes in coupled free-flow/porous-medium-flow systems in Chapter 6 and Chapter 7.

As preparation, we define geometrical relations to describe drops in Section 5.1. Section 5.2 gives an overview of drop dynamics which are caused by flow processes in the liquid reservoir below the drop or in the gaseous surrounding above. In Section 5.3, the mass, momentum and energy balance equations for a single drop on top of a pore are developed.

5.1 Geometry of drops

Assuming the drops to be spherical segments under equilibrium conditions simplifies the calculation of various geometrical quantities. With a constant contact angle θ and $90^\circ \leq \theta \leq 180^\circ$, the spherical segment can be described by the following equations:



$$r_{\text{drop}} = \frac{h_{\text{drop}}}{1 - \cos(\theta)}, \quad (5.1)$$

$$V_{\text{drop}} = \frac{\pi}{3} h_{\text{drop}}^2 (3r_{\text{drop}} - h_{\text{drop}}), \quad (5.2)$$

$$r_{\text{drop}}^{\text{ca}} = r_{\text{drop}} \sin(\theta), \quad (5.3)$$

$$A_{\text{drop}}^{\text{ca}} = \pi (r_{\text{drop}}^{\text{ca}})^2, \quad (5.4)$$

$$A_{\text{drop}}^{\circ} = 2\pi r_{\text{drop}} h_{\text{drop}}, \quad (5.5)$$

Figure 5.1: Geometry of a drop

where $A_{\text{drop}}^{\text{ca}}$ is the contact area with the solid and A_{drop}° refers to the curved surface area of the drop, as shown in Figure 5.1.

5.2 Drop dynamics

Drop formation is a dynamic process, which depends on the surrounding conditions and fluid properties. In the literature, an accumulation of liquid is usually called a drop as soon as it has a curved surface, in contrast to e. g. a film with an almost flat surface. The drop eventually reaches an equilibrium state, which might be disturbed by an external flow field, gravitational forces or expansive/retreating forces due to volume-changing work. Since a liquid drop cannot store any momentum, it either deforms or moves according to the forces resulting from any of these disturbances.

The following considerations are made with respect to a drop on a solid surface. Strictly speaking, we have to consider drops on a liquid surface or even on mixed surfaces (liquid-solid) if the contact area of a grown drop exceeds the pore-throat cross-sectional area. However, this difference is neglected due to the lack of detailed analyses of such a setting. Theodorakakos et al. [2006] connected a sessile drop to a liquid-filled tube and varied the diameter and tube inflow velocity. They found that the droplet shape was hardly affected by these variations and conclude that liquid mass flux into the drop is not fast enough to influence the detachment significantly. Therefore, they also conclude that the small differences due to the reduced friction area between liquid and solid in the case of a liquid-filled pore underneath the drop compared to a drop on a solid surface can be neglected.

In the next paragraphs, different drop dynamics are explained.

Formation

In a coupled free-flow/porous-medium-flow system, liquid drops might form on the surface of the porous medium. The pores of a porous medium are in most cases small enough to be considered as capillary tubes. For a circular capillary tube, where two immiscible fluid phases and a solid phase meet, the Young-Laplace equation (2.11) is extended to take the contact angle θ into account:

$$p_c = \frac{2\gamma_{lg} \cos(\theta)}{r_{\text{tube}}}. \quad (5.6)$$

In a hydrophobic porous medium, the pores with the largest radii fill first, because the capillary pressure p_c is at its minimum in these pores. With contact angles of $90^\circ \leq$

$\theta \leq 180^\circ$, the value of p_c becomes negative due to the cosine function. This reflects the fact that the capillary pressure has to be overcome by the liquid phase to enter the hydrophobic tube, in contrast to a hydrophilic tube where the water would rise due to capillary forces. Near the porous surface, the capillary effect determines the drop formation on top of a pore: A drop forms, if the liquid pressure in the porous medium exceeds the capillary pressure within the pore as well as the gas pressure in the gaseous free flow above the pore:

$$p_i^{\text{pm}} \geq -\frac{2\gamma_{lg} \cos(\theta)}{r_{\text{pore}}} + p_g^{\text{ff}} . \quad (5.7)$$

In the scope of this work, we refer to *formation* as the instant when a surface pore is filled with liquid and the meniscus rises above the pore opening. We assume that a surface pore fills instantaneously with water once the formation criterion (5.7) is met. Hence, surface pores can either be fully gas-filled or fully liquid-filled.

Growth

A drop on a liquid-filled pore can either grow or shrink due to liquid mass fluxes between drop and porous medium. If the pressure gradient within the pore is directed upwards, the drop volume increases. In case of a downward pressure gradient or evaporative fluxes into the gas phase, the drop shrinks. When the drop volume changes, either the contact line moves and therefore the contact area changes, or the contact angle changes while the contact area stays constant. In the scope of this work, we assume the contact angle to be constant during any changes in the drop volume. Therefore, the contact area $A_{\text{drop}}^{\text{ca}}$ increases during growth such that the drop covers a part of the solid surface next to the pore opening as well.

Deformation

A drop on a solid surface surrounded by a gaseous free flow is exposed to several forces due to the flowing fluid as shown in Figure 5.2. A pressure force acting across the drop F_p , a shear force acting on the top wall above the drop F_τ and a dynamic pressure force acting at the front of the drop $F_{p\mathbf{v}^2}$ add up to the drag force F_{drag} exerted by the free flow:

$$F_{\text{drag}} = F_p + F_\tau + F_{p\mathbf{v}^2} . \quad (5.8)$$

Instead of calculating the three force contributions, equations given in the literature for the drag coefficient c_d can be used to obtain the drag force via

$$F_{\text{drag}} = \frac{1}{2} \rho_g v_{g,t}^2 c_d(\text{Re}) A_{\text{proj}} , \quad (5.9)$$

where $v_{g,t}$ is the tangential free-flow velocity component, c_d is the Reynolds number-dependent drag coefficient and A_{proj} is the projected drop area normal to the free-flow direction. This approach is for example chosen by Zhang et al. [2006], who use the empirical correlation given by Clift et al. [1978] to compute the drag coefficient:

$$c_d = \frac{24}{\text{Re}} (1 + 0.1925 \text{Re}^{0.63}) , \quad (5.10)$$

where $\text{Re} = \frac{V_g L}{\nu}$ is the Reynolds number which depends on a characteristic length L . Unfortunately, it is difficult to find a good definition for the characteristic length. Cho et al. [2012] find that the suggestion by Chen [2008]

$$c_d = \frac{30}{\sqrt{\text{Re}}} \quad (5.11)$$

deviates from the experimental results for small droplets with $d_{\text{drop}} < 10^{-4} \text{m}$. Therefore, they determine the fitting parameters a and b empirically and obtain

$$c_d = a \cdot \text{Re}^b \text{ with } a = 46.247 \left(\frac{d_{\text{drop}}}{h_{\text{channel}}} \right)^{0.1757} \text{ and } b = 0.2158 \frac{d_{\text{drop}}}{h_{\text{channel}}} - 0.6384 . \quad (5.12)$$

A different approach is chosen by Kumbur et al. [2006], who define two control volumes around and above the drop to balance the forces directly.

Since the liquid drop cannot take up any momentum, it is deformed by the drag force. Its immediate detachment is prevented by the adhesion or retention force which depends on the surface tension between liquid and gas γ_{lg} as well as the dynamic contact angles between liquid and solid θ_a and θ_r . Cho et al. [2012] suggest to calculate the retention force as

$$F_{\text{ret}} = 2r_{\text{drop}} \pi \gamma_{lg} \sin^2(\theta) \sin\left(\frac{\Delta\theta}{2}\right) . \quad (5.13)$$

Other expressions for F_{ret} are given e.g. by Chen et al. [2005] and Kumbur et al. [2006].

Cho et al. [2012] compare the analytical solutions for drop deformation and detachment with data from experiments and numerical simulations. Due to the good agreement, we

follow their suggestions and apply Equation (5.9) with (5.12) and Equation (5.13) to compute the respective forces.

The ratio of the viscous drag forces to the surface tension force is defined by the dimensionless capillary number Ca :

$$Ca = \frac{\mu_g V_g}{\gamma_{lg}}, \quad (5.14)$$

with a characteristic flow velocity V_g . Flows with low capillary numbers (ca. $Ca < 10^{-5}$) are dominated by capillary forces, otherwise viscous forces are dominant and capillary forces can be neglected. In the scope of this work, the liquid drops are surrounded by a gas phase with velocities of $V_g \geq 1\text{m/s}$. With a dynamic gas viscosity of $\mu_g = 1.8 \cdot 10^{-5} \text{kg m/s}^2$ and a surface tension of $\gamma_{lg} = 0.07 \text{N/m}$, the capillary numbers are $Ca \geq 2.6 \cdot 10^{-4}$. Therefore, the deformation of drops due to viscous forces should not be neglected, because these forces dominate the surface tension forces which try to keep the spherical shape. However, we neglect the deformation of drops due to a lack of knowledge with respect to the resulting advancing and receding contact angles. Additionally, we are mostly interested in the drop's volume instead of its exact shape.

Detachment

In case of a moving gas phase above a drop, the drop deforms as described in the previous section and shown in Figure 5.2. If the drag force F_{drag} becomes larger than the retention force F_{ret} , the drop cannot be hold onto the solid surface any longer and detaches. Therefore, we formulate the detachment criterion as

$$F_{\text{drag}} > F_{\text{ret}}, \quad (5.15)$$

which is also applied by Baber et al. [2016]. Detached drops might roll or slide along the solid surface, merge with other drops, or break up further and evaporate into the gaseous phase. In the scope of this work, we assume the detached drop volume to be transported away with the free flow. For now, we do not take break-up, rolling or sliding along the interface into account. If the formation condition (5.7) is still fulfilled, a new drop forms on the same pore.

Even though the drops are attached to the liquid body within a pore, we assume that the detachment is determined by the condition in Equation (5.15) which is valid for

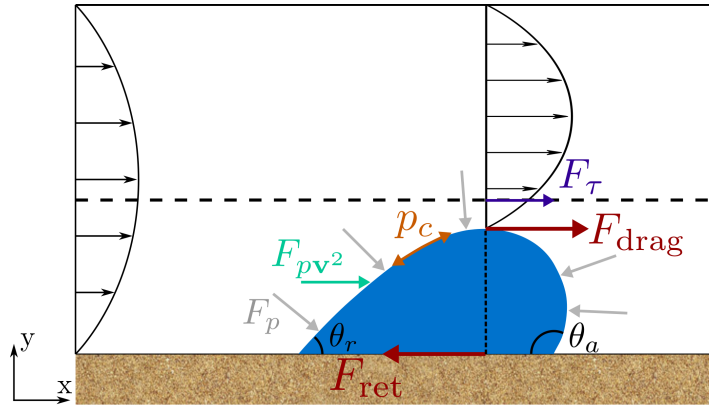


Figure 5.2: Forces acting on a sessile drop surrounded by a gaseous free flow

drops attached to a continuous solid surface as shown in Figure 5.2. For a more precise description, the equivalent of the retention force F_{ret} which holds the drop and liquid body together would have to be modeled.

When the drag force exceeds the surface force, drops might also slide along the interface, without completely detaching from it. The resulting movement of the three-phase contact line is for example investigated by Qin et al. [2012]. Their results show that the contact line extends and deforms with increasing drop volume and gas flow rate.

Spreading

A spherical drop on a solid surface tends to spread and therefore flatten due to gravitational forces. The Bond or Eötvös number Bo is defined as the ratio between gravitational forces and surface tension forces:

$$Bo = \frac{(\rho_l - \rho_g) g L^2}{\gamma_{lg}}, \quad (5.16)$$

where L is a characteristic length, e. g. the drop diameter $d_{drop} = 2r_{drop}$. Low Bond numbers indicate that the surface tension dominates, high Bond numbers suggest that gravitational effects should not be neglected. According to Carey [1992], gravitational effects can be neglected for $Bo < 2.5$. Amongst others, Butt et al. [2007] and Bonaccorso et al. [2013] reformulate this condition and state that gravity can be neglected if $d_{drop} < \sqrt{\frac{2\gamma_{lg}}{\rho_g g}}$, which corresponds to $Bo < 1$. Depending on the wettability property of the solid with respect to the liquid, the contact area increases while the drop height decreases, until the specific equilibrium contact angle θ^* is established.

Fu et al. [2019] present numerical simulations of sessile drops spreading on porous surfaces under the influence of gravitational forces. They find that spreading and penetration are competing processes, which depend on the Bond number, the intrinsic permeability, the equilibrium contact angle, the initial drop size and the grain size in the porous medium.

In the scope of this work, gravitational effects on drops are neglected due to small Bond numbers of $Bo \leq 1$. However, drops sitting on a liquid-filled pore might grow due to a liquid flux from the pore into the drop. In this case, the contact area increases, if the contact angle stays constant. Therefore, we refer to *spreading* as the expansion of the drop contact line due to drop growth.

Merging

If water drops grow, they eventually touch and merge. This leads to a permanent spreading on hydrophilic surfaces and a temporary spreading on hydrophobic surfaces. A thin water film on a hydrophobic surface tends to reduce its contact area with the solid surface and form drops again. If enough water is emerging from the pores to the surface, a permanent water film establishes even on hydrophobic surfaces. This process is of course unstable and difficult to predict. Due to our lack of knowledge concerning these processes, we assume the growing drops to merge as soon as a certain volume fraction of the void space above the porous medium is filled with water. The criterion itself and the respective equations to describe the film flow are given in Section 6.3.

In case of a continuous water film on the porous surface, the gas phase in the porous medium and the free-flow gas phase are no longer connected. Therefore, gaseous mass fluxes between the two compartments are no longer possible. Due to this significant effect on the exchange processes, at least a simple representation of merging drops is taken into account in Section 6.3 to develop a model concept which considers lateral liquid mass fluxes along the interface.

Evaporation

Drops are surrounded by water vapor, which satisfies the gas phase to a certain extent. Butt et al. [2007] point out that a sessile drop is usually never in thermodynamic equilibrium due to evaporation taking place continuously. A liquid with a flat surface evaporates only if its vapor pressure p_{sat}^w is higher than the pressure of its vapor in the

surrounding, i. e. it evaporates only if the surrounding is not saturated with its vapor. Due to their curvature, drops have a slightly higher vapor pressure, and therefore can also evaporate in a saturated atmosphere. However, this will not be considered in the following discussion due to the tiny influence.

We assume the water vapor to behave like an ideal gas, the liquid phase to be incompressible and the liquid pressure inside the drop to be constant. In addition, the surface tension γ_{lg} does not depend on the curvature of the drop surface. Therefore, the Kelvin equation as derived by Galvin [2005] can be used for a drop in equilibrium:

$$p_{\text{sat,Kelvin}}^w = p_{\text{sat}}^w(T) \exp\left(\frac{M^\kappa}{\varrho^\kappa RT} p_c\right) = p_{\text{sat}}^w(T) \exp\left(\frac{M^\kappa}{\varrho^\kappa RT} \frac{2\gamma_{lg}}{r_{\text{drop}}}\right). \quad (5.17)$$

In a non-moving atmosphere ($\mathbf{v}_g^{\text{ff}} = 0$), radial diffusion according to Fick's law takes place:

$$f_{\text{evap}}^w = -\varrho_g D_g \frac{x_g^w}{dr} A^\circ, \quad (5.18)$$

where r is the radial distance from the drop surface A° . Integrating Equation (5.18) to infinity as done by Erbil et al. [2002] and Song et al. [2011] yields

$$\frac{d(\varrho_l V_{\text{drop}})}{dt} = -4\pi r_{\text{drop}} \varrho_g D_g (x_{g,\text{drop}}^w - x_{g,\infty}^w) f(\theta). \quad (5.19)$$

Several expressions for the dependence on the contact angle $f(\theta)$, which itself depends e. g. on surface behavior and surface roughness, are amongst others presented by Picknett and Bexon [1977] and Bourges-Monnier and Shanahan [1995].

A detailed overview of several drop evaporation models with different complexity as well as experimental data for drop evaporation is presented by Wilms [2005].

5.3 Balance equations for a single drop

As explained in the previous section, a drop on top of a pore grows due to liquid mass fluxes from below and shrinks due to evaporative fluxes into the surrounding atmosphere. Since we want to include drops in our conceptual model for coupled free-flow/porous-medium-flow systems, we develop balance equations for a single drop first. These considerations will serve as a base for the description of the interface region later on.

In the following, we formulate the mass and force balances for a single drop on a liquid-filled pore as shown in Figure 5.3a. The drop is surrounded by a gaseous single-phase free flow and connected to the liquid phase of a two-phase flow in a porous medium. The drop mass is segregated from the surrounding gas phase by the drop surface. Towards the porous medium, we define the drop boundary as the virtual horizontal area that connects the edges of the pore throat at the top of the porous medium. For the conservation of mass, we need to take three contributions into account: The rate of change of mass within the drop over time, the mass fluxes across the drop boundaries and possible sinks or sources. If we assume that no sinks or sources are present, and no mass fluxes occur across the contact area with the solid matrix $A_{\text{drop},s}^{\text{ca}}$, the conservation of mass for the drop is given as depicted in Figure 5.3b:

$$\frac{\partial}{\partial t} \int_{V_{\text{drop}}} \varrho_l dV + \int_{A_{\text{pore}}} [(\varrho_l \mathbf{v}_l) \cdot \mathbf{n}]^{\text{pm}} dx = \int_{A_{\text{drop}}^{\circ}} \mathbf{F}_{\text{evap}} \cdot \mathbf{n}^{\text{drop}} dx . \quad (5.20)$$

The vector \mathbf{n} is the unit outer normal vector of the respective domain.

In case of a nonisothermal system, the gaseous mass flux on the right-hand side of the equation represents the water vapor which evaporates from the drop and diffuses into the free flow, see Section 5.2. From the porous-medium side, the drop can only be fed by liquid water fluxes. Evaluating the integrals leads to

$$\frac{\partial(\varrho_l V_{\text{drop}})}{\partial t} + [(\varrho_l \mathbf{v}_l) \cdot \mathbf{n}]^{\text{pm}} A_{\text{pore}} = - [(\varrho_g \mathbf{v}_g) \cdot \mathbf{n}]^{\text{ff}} A_{\text{drop}}^{\circ} , \quad (5.21)$$

where the right-hand side is 0 in an isothermal system.

Since both fluid phases are assumed to consist of the two components water and air, one component mass balance for each component $\kappa \in \{a, w\}$ is formulated. Evaluating the integrals yields the component mass balances similar to the total mass balance (5.21):

$$\begin{aligned} \frac{\partial(\varrho_l V_{\text{drop}} X_l^{\kappa})}{\partial t} + [(\varrho_l \mathbf{v}_l X_l^{\kappa} - D_l^{\text{pm}} \varrho_l \nabla X_l^{\kappa}) \cdot \mathbf{n}]^{\text{pm}} A_{\text{pore}} \\ = - [(\varrho_g \mathbf{v}_g X_g^{\kappa} - D_g \varrho_g \nabla X_g^{\kappa}) \cdot \mathbf{n}]^{\text{ff}} A_{\text{drop}}^{\circ} . \end{aligned} \quad (5.22)$$

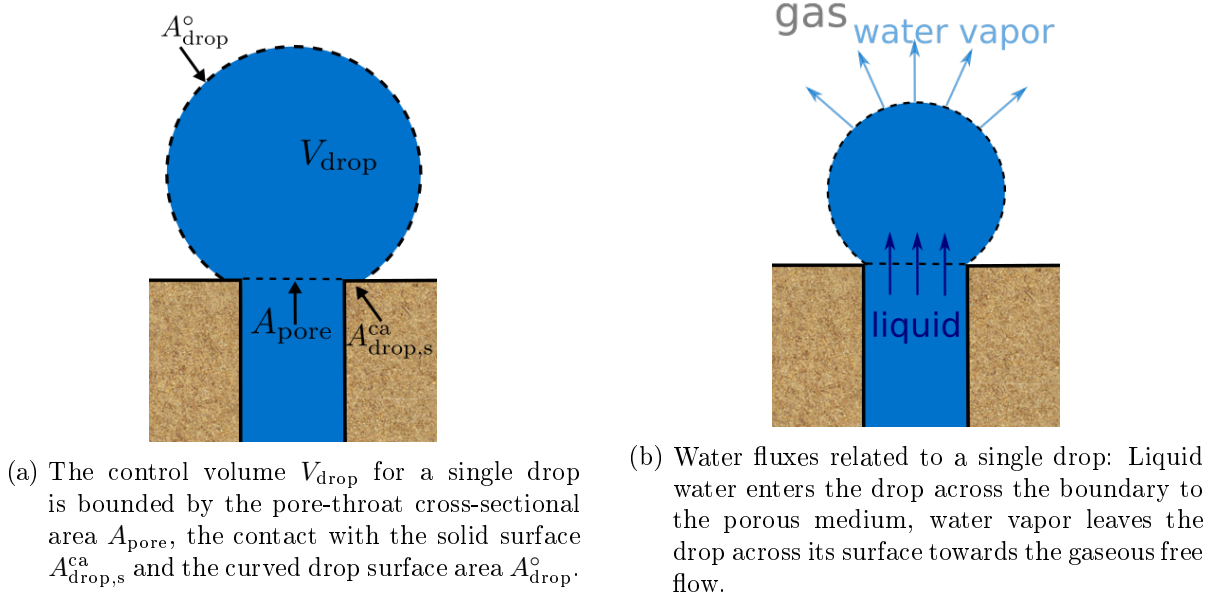


Figure 5.3: Mass balance for a single drop

The drop's energy balance can be written as

$$\begin{aligned} \frac{\partial(\varrho_l V_{\text{drop}} u_l)}{\partial t} + [(\varrho_l \mathbf{v}_l h_l - \lambda_{\text{pm}} \nabla T) \cdot \mathbf{n}]^{\text{pm}} A_{\text{pore}} \\ = - [(\varrho_g \mathbf{v}_g h_g - \lambda_g \nabla T) \cdot \mathbf{n}]^{\text{ff}} A_{\text{drop}}^{\text{o}} . \end{aligned} \quad (5.23)$$

All balance equations are valid for growing as well as shrinking drops up to certain drop volumes. For growing drops, the evaporative flux reduces the drop mass while the liquid mass flux from the porous medium increases the mass. For shrinking drops, both fluxes decrease the mass within the drop. The minimum drop volume after forming and before collapsing as well as the maximum drop volume before a drop detaches or breaks apart have to be determined experimentally.

For mechanical equilibrium at the drop surface, the normal forces are taken into account. Along the drop surface A^{o} , the pressure within the drop p_l^{drop} , the capillary pressure caused by the curvature p_c as well as the free-flow forces acting in normal direction on the surface have to balance:

$$\int_{A^{\text{o}}} [\mathbf{n} \cdot ((\varrho_g \mathbf{v}_g \mathbf{v}_g^T + p_g \mathbf{I} - \mu_g (\nabla \mathbf{v}_g + \nabla \mathbf{v}_g^T)) \mathbf{n})]^{\text{ff}} + \frac{2\gamma_{lg}}{r_{\text{drop}}} dx = \int_{A^{\text{o}}} p_l^{\text{drop}} dx . \quad (5.24)$$

As shown in Figure 5.4, the last term has to be evaluated for the surface of the spherical

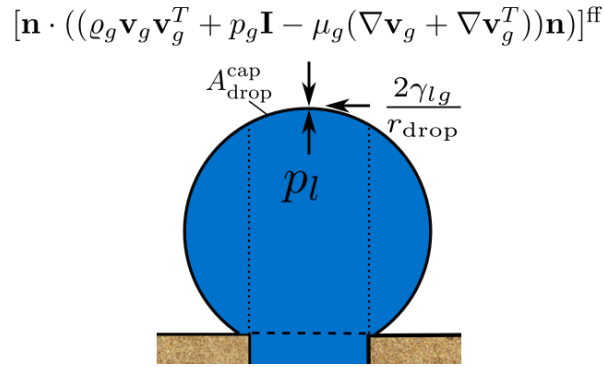


Figure 5.4: Force balance at the drop surface A_{drop}°

cap between the dotted lines $A_{\text{drop}}^{\text{cap}}$ only, because the contributions of the pressure against the side walls of the drop cancel out. At the lower boundary of the drop control volume, the internal drop pressure and the liquid-phase pressure in the porous medium are in equilibrium:

$$\int_{A_{\text{pore}}} p_l^{\text{drop}} dx = \int_{A_{\text{pore}}} p_l^{\text{pm}} dx . \quad (5.25)$$

This expression is based on the assumption that the surface pores of the porous medium are parallel tubes of length δ , which are connected to the liquid or gas reservoirs respectively. The pressure difference along a pore Δp^{pore} is neglected here, since it is small compared to the absolute pressures.

Summary

This chapter presents drop properties and droplet-related processes which are relevant for sessile drops on solid or porous surfaces. Gravitational forces are neglected. Except for the computation of the retention force, the drops are assumed to be spherical segments with a constant contact angle. A drop detaches if the drag force exerted by the surrounding flow field is larger than the retention force. If they do not detach before they touch and merge, drops form film flow even on hydrophobic surfaces. In a nonisothermal model, evaporation from the curved drop surface has to be taken into account since it reduces the drop volume. A set of balance equations is given at the end of this chapter to describe the storage of mass and energy within the drops as well as the respective fluxes across the drop's surface.

6 Coupling concept with drops in a lower-dimensional interface domain

The two-domain macro-scale coupling concept for free-flow/porous-medium-flow systems presented in Section 4.2 follows the assumption that all liquid water that reaches the interface evaporates immediately into the gaseous free flow. However, this does not always hold true. If the evaporation rate is not large enough, water leaving the surface pores might cluster in puddles or form a thin film flow on a hydrophilic porous medium. In case of a hydrophobic porous medium, the water rises within the surface pores with an upwards bent meniscus if an adequate pressure gradient has established. When the three-phase contact line reaches the upper end of a surface pore, a drop starts to form as explained in Section 5.2. These drops reduce the available interface area for gaseous mass fluxes. Growing drops eventually touch and merge to a film if a continuous flux of water from the porous medium is sustained.

According to the definition of the two subdomains in the simple coupling concept in Section 4.2, these drops would then belong to the free-flow domain. However, using a macro-scale description under the assumption of a single-phase gaseous free flow does not allow to describe the presence of liquid drops. Nevertheless, the pore-scale droplet-related processes in the thin interface region should be considered since they affect the exchange of mass, momentum and energy between the macro-scale flow compartments. If all surface pores fill with water or if a continuous film flow establishes, gaseous mass fluxes across the interface are even blocked completely. Since this effect cannot be captured with the simple coupling concept, we develop a multi-scale, multi-physics concept to take the influence of liquid drops at the interface of a gaseous free-flow and a two-phase flow in a hydrophobic porous medium into account.

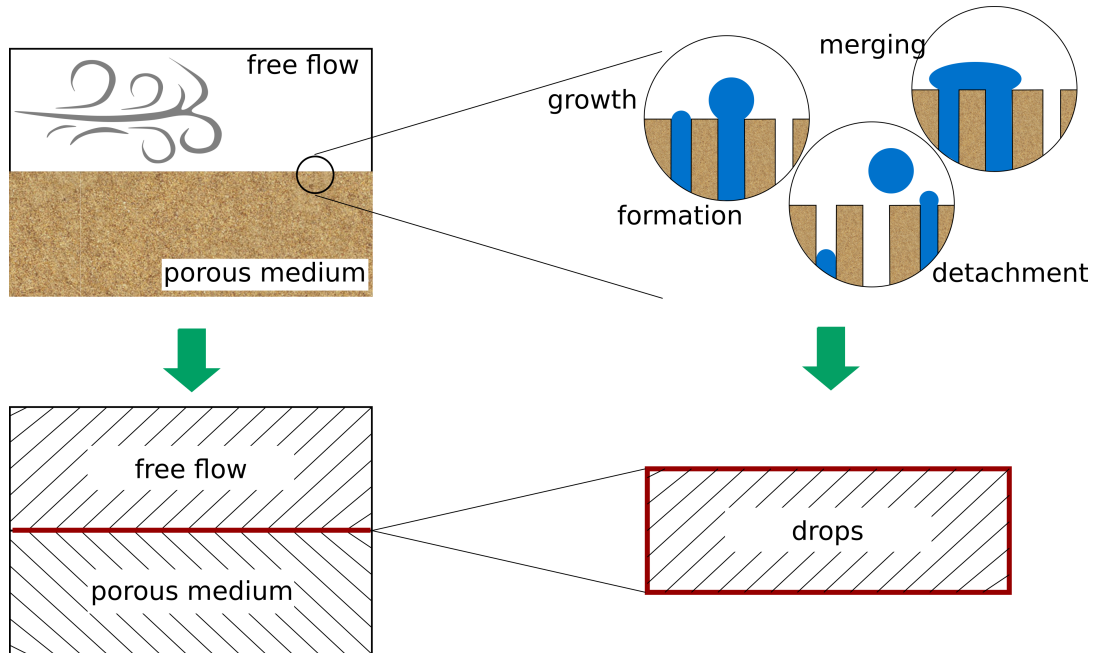


Figure 6.1: Schematic overview of the three-domain approach with a lower-dimensional interface domain to include the droplet-related pore-scale processes in a macroscopic coupled free-flow/porous-medium-flow description

Figure 6.1 illustrates the new multi-scale approach to include drops in the coupled system. It is based on the simple macro-scale coupling concept (Section 4.2), shown in the upper left corner. In the scope of this work, we take a closer look at different dynamic droplet-related processes which occur on the pore-scale, as illustrated in the upper right corner (Section 5.2). We then include these droplet-related processes in an additional interface domain with the help of a simple upscaling technique. This results in an averaged description, as shown schematically in the lower right corner. This full-dimensional interface domain is then reduced by one dimension to a lower-dimensional domain, which is embedded between the two macro-scale model domains as depicted in the lower left corner of Figure 6.1.

The concept of a lower-dimensional domain is for example applied by Gläser et al. [2017] for fractures within porous media. They integrate the equations for flow in porous media over the height of the aperture to reduce the dimension by one. In our case, an upscaling approach is applied to describe the behavior of drops and their effect on the free flow and the flow in the porous medium, without resolving the individual drops anymore.

In the scope of this chapter, the multi-scale coupling concept is introduced in several steps. In Section 6.1, the continuity of fluxes and the force balance are discussed on

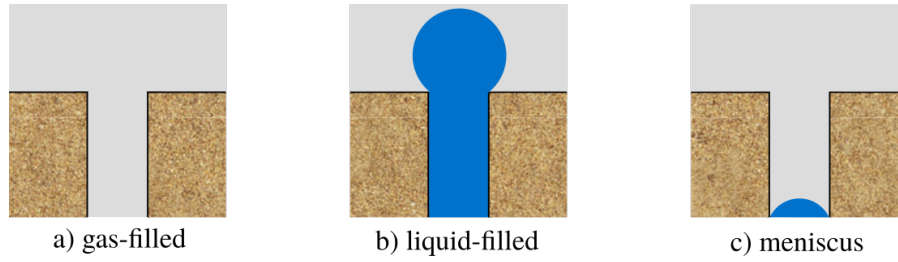


Figure 6.2: Three pore scenarios for two-phase flow between free flow and porous medium

the pore-scale. The transfer of droplet-related information from the pore-scale to the REV-scale is described in Section 6.2. Then, a full-dimensional interface domain is taken into account to formulate the respective balance equations in Section 6.3. In Section 6.4, we reduce the dimension of the interface domain by one and adapt the equations respectively. Coupling conditions for the exchange of mass, momentum and energy are given in Section 6.5. The transmission to a numerical model is explained in Section 6.6. A shortened version describing the three-domain multi-scale coupling concept analogously to the following sections is presented by Ackermann et al. [2021a].

6.1 Pore-scale considerations

If both gas and liquid are present in the porous medium below a surface pore, three different scenarios are possible as shown in Figure 6.2:

- a) The pore is gas-filled, which allows a direct gas flux between porous medium and free flow through the pore.
- b) The pore is liquid-filled and a drop has formed on top, which allows liquid flux from the porous medium through the pore into the drop as well as evaporation from the drop into the surrounding gaseous free flow.
- c) The pore is gas-filled with a liquid meniscus at the bottom, which is connected to the liquid phase in the porous medium and evaporates directly into the free flow.

In this section, we consider the surface pores as a bundle of tubes, where the three cases can occur simultaneously on different pores. However, we neglect the case of a liquid meniscus at the bottom of a gas-filled pore. If the drop formation criterion (5.7) is met, a drop forms and the pore is completely liquid-filled. Otherwise, we assume a gaseous

mass flux from the porous medium towards the free flow and do not distinguish between air from the gaseous phase and water vapor from the liquid phase.

Due to capillary forces or a sufficient pressure difference between the upper and the lower end of a pore, liquid can enter a gas-filled pore and displace the present gas, or vice versa. In a hydrophobic porous medium, liquid water has to overcome the capillary forces with the help of a pressure gradient to invade a pore.

In the following, we assume drop growth under a constant contact angle. As a consequence, the contact area of a growing drop increases and covers not only the pore throat, but also a part of the solid surface. Nevertheless, the area available for liquid mass flux between pore and drop is still A_{pore} and does not depend on the drop radius r_{drop} or the drop volume V_{drop} respectively. In contrast, the surface area A_{drop}° , which determines the evaporative rate, becomes larger with an increasing drop volume.

To balance the fluxes and normal forces, we divide the interface region into four compartments as shown in Figure 6.3:

- **ff**: a free-flow compartment which is the bottom layer of the free-flow domain Ω^{ff} ,
- **if**: a thin interface layer where the drops grow into a free-flow surrounding,
- **bot**: a bundle of tubes as the top layer of the porous medium,
- **pm**: a porous-medium compartment which is the upper part of the porous-medium domain Ω^{pm} .

The free-flow compartment **ff** as well as the porous-medium compartment **pm** represent a part of the free-flow and porous-medium domain respectively. Therefore, the continuity of fluxes across the top and bottom boundary of the domain shown in Figure 6.3 is given due to continuous densities and velocities.

With the drop formation condition in Equation (5.7), it is possible to determine which pores are invaded by liquid. With $A_{\text{pore}} = \pi r_{\text{pore}}^2$, the continuity of mass fluxes between the porous-medium compartment **pm** and the bundle of tubes **bot** can be written as

$$[(\varrho_g \mathbf{v}_g + \varrho_l \mathbf{v}_l) \cdot \mathbf{n}]^{\text{pm}} A_{\Gamma} = \Phi \sum_{\text{gas}} \varrho_g v_g^{\text{pore}} A_{\text{pore}} + \Phi \sum_{\text{liq}} \varrho_l v_l^{\text{pore}} A_{\text{pore}} . \quad (6.1)$$

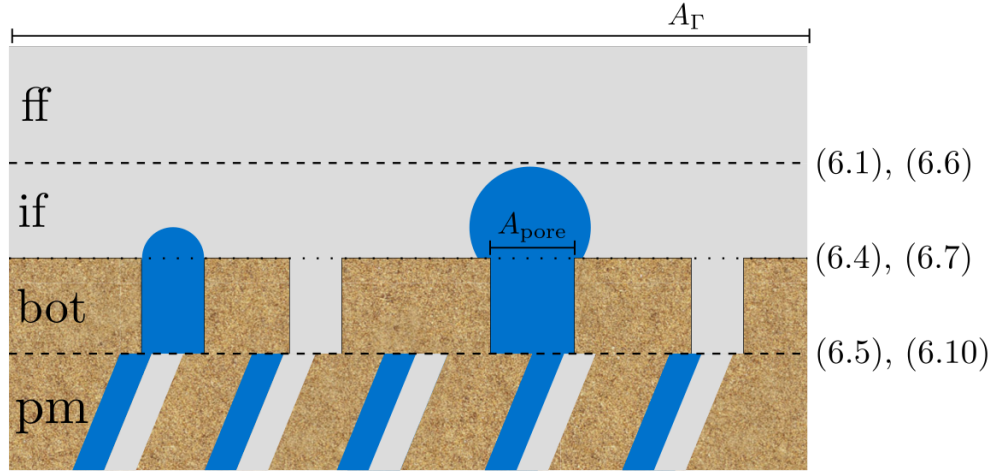


Figure 6.3: A model domain with four compartments: **ff** and **pm** represent averaged REV-scale model subdomains, while **if** and **bot** represent the pore-scale. The numbers refer to the respective coupling conditions.

Multiplying the fluxes on the right-hand side with the porosity Φ bridges the gap between the pore-scale velocities in the bundle of tubes and the REV-scale velocities in the porous medium.

The mass flux from the porous medium is distributed between the gas- and liquid-filled pores according to Equation (6.1). Therefore, the individual phase fluxes have to be equal on both sides:

$$\begin{aligned} [(\varrho_g \mathbf{v}_g) \cdot \mathbf{n}]^{\text{pm}} A_g^{\text{pm}} &= \Phi \sum_{\text{gas}} \varrho_g v_g^{\text{pore}} A_{\text{pore}} , \\ [(\varrho_l \mathbf{v}_l) \cdot \mathbf{n}]^{\text{pm}} A_l^{\text{pm}} &= \Phi \sum_{\text{liq}} \varrho_l v_l^{\text{pore}} A_{\text{pore}} . \end{aligned} \quad (6.2)$$

With these equations, the areas available for gas and liquid flux respectively can be defined as

$$\begin{aligned} A_g^{\text{pm}} &= \sum_{\text{gas}} A_{\text{pore}} , \\ A_l^{\text{pm}} &= \sum_{\text{gas}} A_{\text{pore}} , \end{aligned} \quad (6.3)$$

which yields $A_g^{\text{pm}} + A_l^{\text{pm}} = \Phi A_\Gamma$.

The same areas are available for the fluxes between interface **if** and bundle of tubes **bot**,

i. e. $A_l := A_l^{\text{if}} = A_l^{\text{pm}}$ and $A_g := A_g^{\text{if}} = A_g^{\text{pm}}$. The considerations in Section 4.1 revealed a pressure difference Δp^{pore} between the upper and lower end of a pore. However, this difference is small and is therefore neglected in the following. Consequently, the previous equations can be used to formulate the continuity of mass fluxes between **if** and **pm** directly, which eliminates the bundle-of-tubes compartment from the considerations with respect to the mass flux continuity:

$$[(\varrho_g \mathbf{v}_g) \cdot \mathbf{n}]^{\text{pm}} A_g + [(\varrho_l \mathbf{v}_l) \cdot \mathbf{n}]^{\text{pm}} A_l = \Phi \sum_{\text{gas}} \varrho_g v_g^{\text{if}} A_{\text{pore}} + \Phi \sum_{\text{liq}} \varrho_l v_l^{\text{if}} A_{\text{pore}} . \quad (6.4)$$

For the continuity of mass fluxes between the interface compartment **if** and the free-flow compartment **ff**, only the gas fluxes need to be balanced. According to the considerations in Section 5.3, evaporative fluxes leaving the drop will enter the free-flow domain. In addition, the direct gas flux from the gas-filled pores has to be taken into account:

$$\Phi \sum_{\text{gas}} \varrho_g v_g^{\text{pore}} A_{\text{pore}} + (\mathbf{F}_{\text{evap}} \cdot \mathbf{n}) A_{\text{drop}}^{\circ} = - [(\varrho_g \mathbf{v}_g) \cdot \mathbf{n}]^{\text{ff}} A_{\Gamma} . \quad (6.5)$$

The evaporative flux \mathbf{F}_{evap} is defined in Section 5.3.

Equations (6.1) and (6.5) can analogously be applied for the component mass and energy fluxes between the compartments.

For the balance of normal forces between porous medium **pm** and bundle of tubes **bot**, the mechanical equilibrium can be formulated as

$$p_g^{\text{pm}} A_g + p_l^{\text{pm}} A_l = \sum_{\text{gas}} p_g^{\text{pore}} A_{\text{pore}} + \sum_{\text{liq}} p_l^{\text{pore}} A_{\text{pore}} . \quad (6.6)$$

Again, we assume the pore-scale pressures to be equal to the REV-scale pressures.

Between the bundle of tubes **bot** and the interface compartment **if**, the respective pressures act on the same areas and therefore balance each other:

$$\begin{aligned} p_g^{\text{pore}} &= p_g^{\text{if}} , \\ p_l^{\text{pore}} &= p_l^{\text{if}} = p_l^{\text{drop}} . \end{aligned} \quad (6.7)$$

When the small pressure differences Δp^{pore} within the pores are neglected, the balance of normal forces can also be formulated for the porous medium and interface by substituting

the pore pressures in Equation (6.6) with the interface pressures in Equation (6.7). In summary, the balance of normal forces between **if** and **pm** is

$$p_g^{\text{pm}} A_g + p_l^{\text{pm}} A_l = p_g^{\text{if}} A_g + p_l^{\text{drop}} A_l . \quad (6.8)$$

The capillary pressure p_c can be used to convert the liquid pore pressure into a sum of p_c and the gas pore pressure via $p_l = p_g + p_c$, yielding

$$\begin{aligned} p_g^{\text{pm}} A_g + (p_g + p_c)^{\text{pm}} A_l &= p_g^{\text{if}} A_g + (p_g + p_c)^{\text{if}} A_l \\ p_g^{\text{pm}} A_g + p_g^{\text{pm}} A_l + p_c A_l &= p_g^{\text{if}} A_g + p_g^{\text{if}} A_l + p_c A_l \\ p_g^{\text{pm}} (A_g + A_l) + p_c A_l &= p_g^{\text{if}} (A_g + A_l) + p_c A_l \\ p_g^{\text{pm}} &= p_g^{\text{if}} . \end{aligned} \quad (6.9)$$

For the force balance between **ff** and **if**, we get the following equation under the assumption of small or zero velocities within the interface compartment:

$$[\mathbf{n} \cdot ((\rho_g \mathbf{v}_g \mathbf{v}_g^T + p_g \mathbf{I} - \mu_g (\nabla \mathbf{v}_g + \nabla \mathbf{v}_g^T)) \mathbf{n})]^{\text{ff}} A_\Gamma = p_g^{\text{if}} A_\Gamma . \quad (6.10)$$

6.2 Transfer from the pore- to the REV-scale

For the transfer of the droplet-related information to the REV-scale, we first homogenize the pore sizes to reduce computational costs. Then, the pore-scale descriptions of drop formation, growth and detachment are converted to REV-scale descriptions with the help of REV-scale quantities in the free flow and flow in the porous medium.

The surface pore radii of a porous medium can possibly lie within a large spatial range and occur in a large variety. Even if all occurring radii were known, evaluating the drop formation condition (5.7) for each possible pore radius would lead to high computational costs. Therefore, we cluster all occurring pore radii in pore-size classes with a mean pore radius \bar{r}_{pore} . With the number of pores in a pore-size class $n_{\bar{r}_{\text{pore}}}$, the percentage of pores belonging to a certain pore-size class is given as $f_{\bar{r}_{\text{pore}}} = \frac{\Phi A_\Gamma}{n_{\bar{r}_{\text{pore}}} A_{\text{pore}}}$, analogous to the definitions specified by Baber et al. [2016]. An example for a pore-size distribution is given in Figure 6.4, which would require only four evaluations of Equation (5.7). The

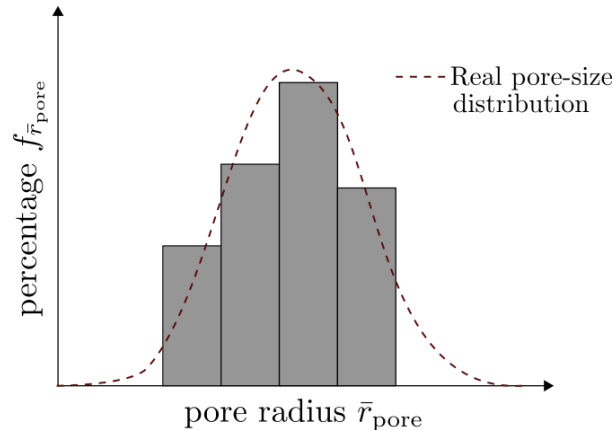


Figure 6.4: Real (dashed line) and homogenized (rectangles) pore-size distribution

loss of pore-scale information with such a homogenization procedure is neglected in the scope of this work.

The homogenization applied here differs from the one used by Baber et al. [2016]. After evaluating the drop formation condition (5.7) for each pore-size class, they compute an upscaled drop volume as the sum of all individual drops. The detachment criterion (5.15) is then evaluated for the upscaled drop only. Due to the large projected area of such an upscaled drop, the detachment happens for relatively small free-flow velocities. In contrast, we consider the growth and detachment processes for each pore-size class individually by considering the respective projected areas to compute the drag force F_{drag} . Drops on differently sized pores might form and grow with a delay in time, and therefore detach at different times, which is taken into account in our approach. Therefore, we obtain a more detailed representation of the current amount of liquid water within the interface domain.

Considerations based on a bundle of tubes were already presented in Section 6.1 as a first step towards an REV-scale model. In the following, the top layer of the porous medium is assumed to be such a bundle of tubes, while the interface domain itself is only represented by a thin layer of the free flow. Therefore, the bundle of tubes is not explicitly modeled as part of the coupled system. To bridge the gap between the different spatial scales, several pores are taken into account in each control volume on the REV-scale.

To stress the dependence of the drop formation on the respective pore radius, the drop

formation condition (5.7) can be rearranged to yield a critical radius r^{crit} :

$$\bar{r}_{\text{pore}} \geq r^{\text{crit}} = -\frac{2\gamma_{lg} \cos(\theta)}{p_l^{\text{pm}} - p_g^{\text{ff}}} . \quad (6.11)$$

For each pore-size class where \bar{r}_{pore} fulfills this condition, drops are assumed to form on all $n_{\bar{r}_{\text{pore}}}$ pores. Therefore, the cross-sectional areas of these pores are summed up to be taken into account for liquid mass fluxes between porous medium and interface later on:

$$A_l = \sum_{\bar{r}_{\text{pore}} \geq r^{\text{crit}}} \pi(\bar{r}_{\text{pore}})^2 n_{\bar{r}_{\text{pore}}} . \quad (6.12)$$

If condition (6.11) is fulfilled for the pore radii \bar{r}_{pore} of all pore-size classes, the area available for gaseous mass fluxes is $A_g = \Phi A_\Gamma - A_l = 0$.

As soon as drops have formed, they grow due to liquid mass fluxes from the porous medium. The REV-scale liquid mass flux q_l^{pm} from the porous medium into the drops has to be distributed to all pores according to

$$q_l^{\text{pm}} = [\varrho_l \mathbf{v}_l \cdot \mathbf{n}]^{\text{pm}} A_l = [\varrho_l \mathbf{v}_l \cdot \mathbf{n}]^{\text{pm}} \sum_{\bar{r}_{\text{pore}} \geq r^{\text{crit}}} \pi(\bar{r}_{\text{pore}})^2 n_{\bar{r}_{\text{pore}}} , \quad (6.13)$$

where the velocity \mathbf{v}_l depends on the pressure gradient ∇p_l between porous medium and interface domain. An individual drop on a pore with radius \bar{r}_{pore} is therefore fed by the mass flux

$$q_{l,\text{pore}}^{\text{pm}}(\bar{r}_{\text{pore}}) = \frac{q_l^{\text{pm}} f_{\bar{r}_{\text{pore}}}}{n_{\bar{r}_{\text{pore}}}} . \quad (6.14)$$

In addition to the exchange between porous medium and interface domain, the gaseous mass flux between free flow and interface q^{ff} has to be taken into account. As explained in Section 6.1, this flux consists of the gas entering the interface domain from the porous medium through gas-filled pores as well as the evaporative fluxes, i. e. the water vapor from the drop surface. Under the assumption of isothermal conditions, this mass flux is zero in case all pores are filled with liquid.

The drop volume is determined by the balance between the feeding liquid mass fluxes from the porous medium and the evaporative gaseous fluxes into the free flow, as given in Equation (5.21). Depending on this balance, drops can shrink, grow or have a constant volume. A growing drop detaches if the force exerted by the free flow is larger than the

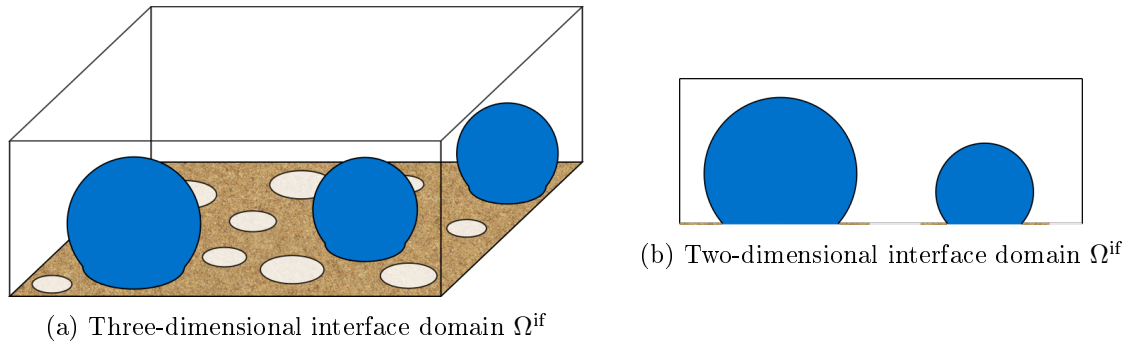


Figure 6.5: Schematic representation of the full-dimensional interface domain

surface-tension force, as explained in Section 5.2. The mass and energy losses due to drop detachment are transferred to the macro-scale by summing up all drop volumes for which the detachment condition (5.15) is fulfilled within each REV. We assume that the respective drops completely detach from the pores and are transported away by the free flow, without further interactions.

6.3 Full-dimensional interface domain

With the considerations in the previous two sections, we derive a model concept for a full-dimensional interface domain where droplet-related processes are taken into account. Based on the conclusions in Section 6.1, the REV-scale interface domain Ω^{if} consists of a thin layer of the free-flow region only. It is connected to a bundle of tubes in the top layer of the porous medium as well as to a free flow. As shown in Figure 6.5, it resembles the **if** compartment in Figure 6.3. For the sake of simplicity, some processes are illustrated for the two-dimensional version only in the following. Nevertheless, it has to be kept in mind that a realistic representation of the occurring processes requires a three-dimensional description.

6.3.1 Assumptions

When describing droplet-related processes, several assumptions and simplifications become necessary. In accordance to the approach by Baber [2014], we make the following assumptions with respect to the drops:

- static equilibrium conditions,

- constant pressure around each drop,
- rapid mixing (constant temperature, mole fractions and pressure inside the drop),
- gravity can be neglected,
- laminar flow conditions,
- constant curvature of the drop surfaces,
- spherical drops with circular contact lines.

The last assumption is dropped when computing the retention force F_{ret} , since the corresponding equations have been obtained empirically and depend on the advancing θ_a and receding θ_r contact angles of a deformed drop. Even though the derivation of the detachment condition (5.15) is valid for deformed drops as shown in Figure 5.2, we assume spherical, non-deforming drops to simplify the computation of the drop geometries and respective forces. The small changes in the surface area due to deformation are also neglected for the evaporative fluxes from the drop into the free flow.

Furthermore, the assumptions are not completely valid anymore as soon as lateral fluxes occur, since the film does not have a curved surface but is assumed to be flat.

6.3.2 Balance equations

Deriving balance equations for the interface domain requires the definition of a control volume Ω^{if} . In the following, we assume Ω^{if} to represent the whole interface domain as shown in Figure 6.5. The height of the interface domain Ω^{if} is assumed to be the height $h_{\text{drop}}^{\text{max}}$ of the biggest possible drop, which forms on the largest pore. The conservation of mass within the domain $\Omega \subseteq \Omega^{\text{if}}$ is given as

$$\sum_{\alpha} \frac{\partial(\varrho_{\alpha} S_{\alpha})}{\partial t} + \sum_{\alpha} (\nabla \cdot \mathbf{F}_{\alpha}) = \sum_{\alpha} q_{\alpha}, \quad (6.15)$$

where the phases are denoted by $\alpha \in \{g, l\}$ and \mathbf{F}_{α} is the respective mass flux. Integrating over Ω yields

$$\int_{\Omega} \sum_{\alpha} \frac{\partial(\varrho_{\alpha} S_{\alpha})}{\partial t} dV + \int_{\Omega} \sum_{\alpha} (\nabla \cdot \mathbf{F}_{\alpha}) dV = \int_{\Omega} \sum_{\alpha} q_{\alpha} dV. \quad (6.16)$$

The saturations S_α are defined analogously to the quantities in a porous medium and represent the volume fraction occupied by the respective phase α . The liquid saturation S_l directly corresponds to the total drop volume present in Ω via $S_l = \sum V_{\text{drop}}/|\Omega|$. We assume a porosity of $\Phi = 1$ in the interface domain, because no solid phase is present. Therefore, the porosity is omitted in the balance equations. Applying the Gauß theorem yields surface integrals for the flux terms:

$$\int_{\Omega} \sum_{\alpha} \frac{\partial(\varrho_{\alpha} S_{\alpha})}{\partial t} dV + \int_{\Gamma} \sum_{\alpha} (\mathbf{F}_{\alpha} \cdot \mathbf{n}) dS = \int_{\Omega} \sum_{\alpha} q_{\alpha} dV . \quad (6.17)$$

The first term represents the storage of liquid and gas within the interface domain. The second term represents the mass fluxes and can be divided into flux terms across the different boundaries of Ω :

$$\int_{\Gamma} \sum_{\alpha} (\mathbf{F}_{\alpha} \cdot \mathbf{n}) dS = \int_{\Gamma^{\text{top}}} (\mathbf{F}_g \cdot \mathbf{n}) dS + \int_{\Gamma^{\text{lateral}}} \sum_{\alpha} (\mathbf{F}_{\alpha} \cdot \mathbf{n}) dS + \int_{\Gamma^{\text{bottom}}} \sum_{\alpha} (\mathbf{F}_{\alpha} \cdot \mathbf{n}) dS . \quad (6.18)$$

In the context of a coupled free-flow/porous-medium-flow system, the mass fluxes across Γ^{top} equal the mass fluxes entering the free-flow domain q^{ff} , as shown in Equation (6.5). Therefore, only gaseous mass fluxes are taken into account. Analogously, the boundary Γ^{bottom} is shared with the porous-medium domain and allows the transfer of gaseous as well as liquid matter with $q^{\text{pm}} = q_l^{\text{pm}} + q_g^{\text{pm}}$, see Equation (6.4).

If flow tangential to the interface is neglected, the mass fluxes across all lateral boundaries Γ^{lateral} are zero. Otherwise, lateral mass fluxes along the interface due to pressure gradients have to be taken into account. In the scope of this work, a simple merging criterion is applied due to the lack of detailed knowledge: If

$$\frac{\sum V_{\text{drop}}}{|\Omega|} = S_l^{\text{if}} > S_l^{\text{merge}} , \quad (6.19)$$

the individual drops are assumed to touch and merge, resulting in a thin film flow. This film can only persist on a hydrophobic surface if it is continuously fed with water from the porous medium below. The critical saturation S_l^{merge} should be determined experimentally. We model the lateral phase velocities analogously to the Darcy velocity as

$$v_{\alpha}^{\text{if}} = -K \frac{k_{r\alpha}}{\mu_{\alpha}} (\nabla p_{\alpha} - \varrho_{\alpha} g) , \quad (6.20)$$

with the horizontal gravity component $g = 0$. The permeability is assumed to be $K = \frac{h^2}{12}$,

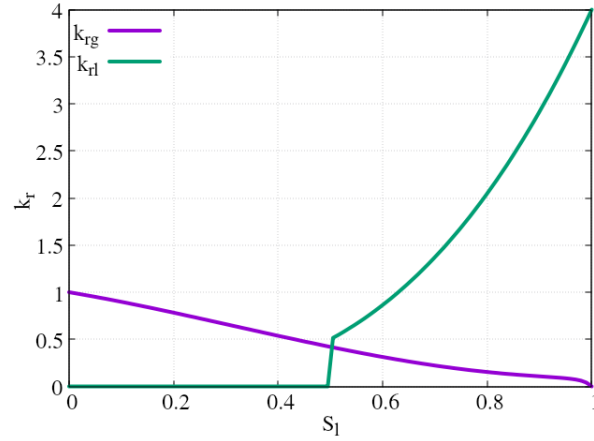


Figure 6.6: The $k_r - S_l$ relationships for lateral fluxes with an exemplary value of $S_l^{\text{merge}} = 0.5$

analogous to pipe flow. Of course, the film has an open surface on top instead of a wall boundary as assumed for pipe flow. Nevertheless, we will use this assumption until we are able to formulate a more appropriate permeability model. The relative permeability for the liquid phase depends on S_l^{merge} and is assumed to be given as

$$k_{rl} = \begin{cases} 0 & S_l \leq S_l^{\text{merge}} \\ 4S_l^3 & S_l > S_l^{\text{merge}} \end{cases} . \quad (6.21)$$

Independent of the liquid film flow, gaseous mass flux can take place along the interface. Its relative permeability does therefore not depend on S_l^{merge} :

$$k_{rg} = (1 - S_l^2)(2(S_l + 2) - 3 \frac{\mu_l(1 - S_l^2) + \mu_g S_l^2}{\mu_l(1 - S_l) + \mu_g S_l}) . \quad (6.22)$$

The $k_r - S_l$ relationships are shown in Figure 6.6 and were recently developed at the Department of Hydromechanics and Modelling of Hydrosystems (University of Stuttgart) by Carina Bringedal and published by Ackermann et al. [2021a]. They are derived analytically with the help of a homogenization technique via asymptotic expansions.

Similar to the total mass balance Equation (6.15), balance equations for component mass and energy are formulated:

$$\sum_{\alpha} \frac{\partial(\varrho_{\alpha} S_{\alpha} X_{\alpha}^{\kappa})}{\partial t} + \sum_{\alpha} (\nabla \cdot \mathbf{F}_{\alpha}^{\kappa}) = \sum_{\alpha} q_{\alpha}^{\kappa} \quad (6.23)$$

and

$$\sum_{\alpha} \frac{\partial(\varrho_{\alpha} S_{\alpha} u_{\alpha})}{\partial t} + \sum_{\alpha} (\nabla \cdot \mathbf{F}_{\alpha}^T) = \sum_{\alpha} q_{\alpha}^T \quad (6.24)$$

For the component mass and energy flux terms, the same restrictions as for the total mass flux apply. If lateral fluxes are neglected, all fluxes across the boundaries Γ^{lateral} are zero. The component mass fluxes $\mathbf{F}_{\alpha}^{\kappa}$ across the remaining boundaries consist of advective and diffusive fluxes for component transport in Equation (6.23). In Equation (6.24), the heat fluxes \mathbf{F}_{α}^T are made up of advective and conductive fluxes respectively.

6.4 Lower-dimensional interface domain

Since the full-dimensional interface domain in the previous section is assumed to be approximately of drop height $h_{\text{drop}}^{\text{max}}$, it does not have to be resolved with a fine grid in the y-direction, normal to the surface of the porous medium. One grid cell would be enough to capture the droplet-related processes between the adjacent grid cells belonging to the free-flow and porous-medium-flow domains respectively. Therefore, a lower-dimensional formulation is derived in the following to reduce the computational costs and simplify the model concept. The lower-dimensional interface Γ is then defined as the intersection of the free-flow and the porous-medium-flow domains: $\Gamma = \bar{\Omega}^{\text{ff}} \cap \bar{\Omega}^{\text{pm}}$.

The total mass balance for the interface Γ is then

$$\sum_{\alpha} \frac{\partial(\varrho_{\alpha} S_{\alpha})}{\partial t} + \sum_{\alpha} (\nabla \cdot \mathbf{F}_{\alpha}) = q^{\text{ff}} + q^{\text{pm}} - q^{\text{detach}}. \quad (6.25)$$

The lower-dimensional interface domain does not have any boundaries with the free-flow and porous-medium-domain respectively as depicted in Figure 6.7. Therefore, the exchange of mass with these two domains has to be included in the sink/source terms q^{ff} and q^{pm} on the right-hand side, see Section 6.5. The last sink term accounts for the detached drops within Γ :

$$q^{\text{detach}} = \begin{cases} 0 & \text{drop has not detached} \\ \frac{\varrho_l V_{\text{drop}}}{\Delta t} & \text{drop has detached.} \end{cases} \quad (6.26)$$

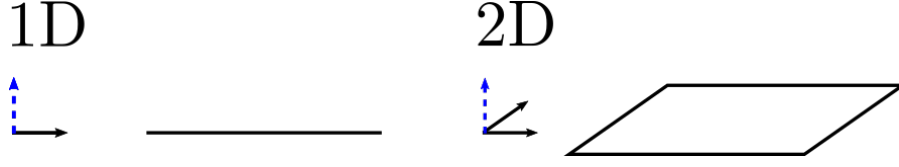


Figure 6.7: The mass and energy fluxes between the interface domain and the neighboring domains occur along the direction of the dashed blue arrows, which does not coincide with the dimension of the interface domain itself.

Due to the dimensional differences, all volume-related terms are multiplied by extrusion factors to guarantee consistency in the units. Details on these factors are given with the numerical model in Section 6.6.3.

Both phases are made up of the two components water w and air a . For each component $\kappa \in \{w, a\}$, the following component mass balance holds:

$$\sum_{\alpha} \frac{\partial(\varrho_{\alpha} S_{\alpha} X_{\alpha})}{\partial t} + \sum_{\alpha} (\nabla \cdot \mathbf{F}_{\alpha}^{\kappa}) = q^{\text{pm},\kappa} + q^{\text{ff},\kappa} - q^{\text{detach},\kappa}, \quad (6.27)$$

with $q^{\text{detach},\kappa} = \frac{\varrho_l X_l^{\kappa} V_{\text{drop}}}{\Delta t}$ in case of detachment.

In addition to the mass balances, an energy balance is needed to describe a nonisothermal system:

$$\sum_{\alpha} \frac{\partial(\varrho_{\alpha} S_{\alpha} u_{\alpha})}{\partial t} + \nabla \cdot \mathbf{F}_T = q_T^{\text{ff}} + q_T^{\text{pm}} - q_T^{\text{detach}}, \quad (6.28)$$

with $q_T^{\text{detach}} = \frac{\varrho_l u_l V_{\text{drop}}}{\Delta t}$.

If lateral mass fluxes along the interface are taken into account, the phase velocities are computed as in Equation (6.20) with the respective relative permeabilities. The mass fluxes are then given as

$$q_g^{\text{if}} = \varrho_g v_g^{\text{if}} A^{\text{if}} \quad (6.29)$$

and

$$q_l^{\text{if}} = \varrho_l v_l^{\text{if}} A^{\text{if}}, \quad (6.30)$$

where A^{if} is the cross-sectional area of the interface. For a one-dimensional interface domain, the cross-sectional area is obtained with the help of the extrusion factor ξ_{1D} (see Section 6.6.3). The lateral mass fluxes along the interface are parallel to the tangential vectors of the free-flow and porous-medium domain boundaries which coincide with the interface Γ .

6.5 Coupling concept with lower-dimensional interface domain

With the description of the lower-dimensional interface domain in the previous section, it is possible to formulate a three-domain coupling concept. Here, the exchange of mass, momentum and energy between the free flow and the interface, as well as between the interface and the porous medium is taken into account. In contrast to the two-domain approach, the free flow and the flow in the porous medium are not directly coupled with each other, but interact via the interface domain.

The exchange of mass takes place across the gaseous- and liquid-filled pores, whose cross-sectional areas are added up to A_g and A_l as explained in Section 6.2. In the numerical model, the balance equation integrals are only evaluated after all individual terms are computed. Therefore, the sum of the individual mass and heat flux terms is multiplied by the area A_Γ automatically. As a consequence, we need to use relative values instead of absolute areas in the balance equations to account for the fact that not the whole area A_Γ is available for the fluxes. Therefore, we define the respective area fractions as

$$a_l = \frac{A_l}{\Phi A_\Gamma}, \quad (6.31)$$

$$a_g = \frac{A_g}{\Phi A_\Gamma}. \quad (6.32)$$

These area fractions are then used to account for the drops in the coupling mass fluxes:

$$q^{\text{ff}} = [(\varrho_g \mathbf{v}_g) \cdot \mathbf{n}]^{\text{ff}} A_\Gamma, \quad (6.33)$$

$$q^{\text{pm}} = [(\varrho_g \mathbf{v}_g) \cdot \mathbf{n}]^{\text{pm}} a_g A_\Gamma + [(\varrho_l \mathbf{v}_l) \cdot \mathbf{n}]^{\text{pm}} a_l A_\Gamma. \quad (6.34)$$

The water flowing from the porous medium into the interface domain across the liquid-covered area $a_l A_\Gamma$ feeds the drop. This mass flux is given as $q_l^{\text{pm}} = [(\varrho_l \mathbf{v}_l) \cdot \mathbf{n}]^{\text{pm}} a_l A_\Gamma$ and matches the mass flux in Equation (5.21). Obviously, these fluxes are zero if no drop is present and $a_l = 0$. In that case, the available area fraction for gas flux is $a_g = 1$ and $q^{\text{pm}} = [(\varrho_g \mathbf{v}_g) \cdot \mathbf{n}]^{\text{pm}} A_\Gamma$, which corresponds to the mass flux in the simple coupling concept, see Equation (4.21).

Adding these mass fluxes to the current upscaled drop volume in the drop domain yields the new drop volume:

$$V_{\text{drop}}^{\text{up}} = V_{\text{drop}}^{\text{up,old}} + \frac{\Delta t}{\varrho_l} q_l^{\text{pm}}. \quad (6.35)$$

With this concept, the macro-scale balance equations contain two upscaled quantities which represent the droplet-related pore-scale processes: the ratio of liquid-filled pores at the interface area a_l and the proportion of the interface area that is available for gas exchange a_g . These quantities do not resolve individual drops, but help to model the drops' influence on the surrounding flow regimes. The fractions depend mostly on the respective drop volume, which itself is determined by the formation, growth and detachment processes. We neglect the deformation process in our model concept, since it does not change the area which is available for liquid fluxes from the porous medium into the drop.

6.6 Numerical model

The balance equations given in Sections 3.1, 3.2 and 6.4 are now combined with the coupling conditions in Sections 4.2 and 6.5. This results in a global system of the form $\mathbf{J}(\mathbf{u}) \cdot \mathbf{u} = \mathbf{R}$, which is evaluated numerically with a monolithic approach. A schematic view of the system's Jacobian matrix $\mathbf{J}(\mathbf{u})$ is given in Figure 6.8. The choice of appropriate discretizations in space and time depends on the problem at hand. In the following, we use the same discretizations as for the simple coupling concept presented in Section 4.3. For the interface domain, a cell-centered two-point flux approximation is applied analogously to the porous-medium domain. For each balance equation, appropriate boundary conditions have to be set. Details on the choice of boundary conditions for the presented test cases are given in Chapter 8. In the following, a few general issues regarding the implementation of the lower-dimensional interface domain coupling concept are discussed.

6.6.1 Pressure gradients and resulting fluxes

For the conservation of mass, momentum and energy in the interface domain, the storage within each control volume, the fluxes across the boundaries and the sources within each

FF	FF/IF	0
IF/FF	IF	IF/PM
0	PM/IF	PM

Figure 6.8: Schematic view of the Jacobian matrix for the global system of equations with the respective submatrices for the free-flow, interface and porous-medium subdomains and associated couplings

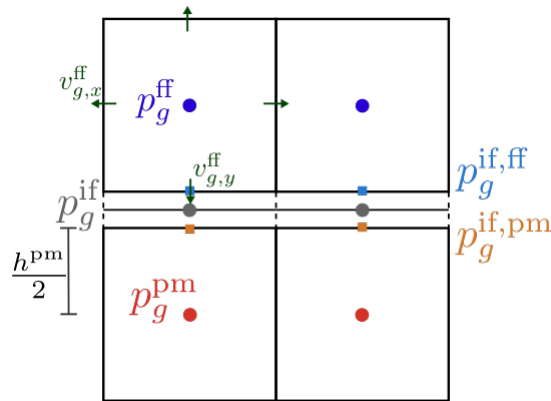


Figure 6.9: Locations where the gas pressure is stored (circles) and extrapolated (squares)

control volume have to be evaluated. The mass flux terms across the faces are summed up to the total flux q as

$$q = q^{\text{pm}} + q^{\text{ff}} + q_{\text{lateral}}^{\text{if}}. \quad (6.36)$$

As mentioned before, the fluxes across the upper and lower boundary have to be modeled as sink/source terms in a lower-dimensional domain, see Figure 6.7. Fluxes across real boundaries are referred to as *lateral* fluxes in the following.

Flux between interface and free flow

Due to the staggered grid discretization scheme (Section 4.3.1), the velocity component of the free-flow velocity \mathbf{v}_g^{ff} normal to the interface is stored on the horizontal face of the free-flow control volume. Therefore, this value can be used directly to compute the mass flux

$$q_g^{\text{ff}} = (\varrho_g^{\text{ff}} \mathbf{v}_g^{\text{ff}}) \cdot \mathbf{n}^{\text{ff}} A_{\Gamma}. \quad (6.37)$$

Flux between interface and porous medium

For the porous medium, a cell-centered discretization scheme is used. Therefore, the phase velocities at the upper boundary of Ω^{pm} are not given and need to be calculated according to the respective gradients. The locations of stored and extrapolated pressure values are illustrated in Figure 6.9.

The gaseous mass flux from the porous medium towards the interface is driven by the pressure gradient between cell center and upper boundary

$$\nabla p_g^{\text{pm}} = \frac{p_g^{\text{pm}} - p_g^{\text{if,pm}}}{h^{\text{pm}}/2}. \quad (6.38)$$

The mass flux between the edge of the interface domain control volume and its center is driven by

$$\nabla p_g^{\text{if}} = \frac{p_g^{\text{if,pm}} - p_g^{\text{if}}}{h^{\text{if}}/2}. \quad (6.39)$$

Combining these two gradients in order to compute the mass flux between porous medium and interface yields the overall pressure gradient

$$\nabla p_g^{\text{if,pm}} = \frac{p_g^{\text{pm}} - p_g^{\text{if}}}{h^{\text{pm}}/2}, \quad (6.40)$$

since the cell center and edge of a lower-dimensional interface domain element coincide ($h = h^{\text{pm}} + h^{\text{if}} = h^{\text{pm}} + 0 = h^{\text{pm}}$). If a drop exists in the interface domain, the same principle applies to the liquid pressure gradient

$$\nabla p_l^{\text{if,pm}} = \frac{p_l^{\text{pm}} - p_l^{\text{if}}}{h^{\text{pm}}/2}. \quad (6.41)$$

Therefore, the pressures $p_g^{\text{if,pm}}$ and $p_l^{\text{if,pm}}$ are eliminated.

Flux along the interface

For the case of lateral mass fluxes, we compute the phase velocities according to Darcy's law. This assumption allows to take the influence of the respective other phase on the flow velocities into account with the help of the relative permeability $k_{r\alpha}$.

The lateral mass flux along the interface domain for each phase $\alpha \in \{g, l\}$ can be written as

$$q_\alpha^{\text{if}} = \varrho_\alpha v_\alpha A_n^{\text{if}} = \varrho_\alpha \left(-K \frac{k_{r\alpha}}{\mu_\alpha} \nabla p_\alpha \right) A_n^{\text{if}} = -K \frac{k_{r\alpha}}{\mu_\alpha} \frac{p_\alpha^{i-1} - p_\alpha^i}{\Delta x} A_n^{\text{if}}, \quad (6.42)$$

where A_n^{if} is the area between neighboring interface domain elements with the indices i and $i - 1$.

We define the mobility $\lambda_\alpha = \frac{k_{r\alpha}}{\mu_\alpha}$ to be dependent on the liquid saturation S_l with the $S_l - k_{r\alpha}$ -relationships given in Section 6.3 (Figure 6.6). The appropriate value for S_l^{merge} has to be determined experimentally and will only be estimated within this work.

6.6.2 Upscaling

Baber et al. [2016] assemble the upscaled drop volumes of several grid cells to form one large drop within a drop domain $\Omega_{\text{drop}}^{\text{REV}}$. The drop radius as well as the area fractions a_g and a_{drop} are computed for the large drop and then used in each of the contributing cells to account for the coupling mass fluxes. This does not allow to take the drop volume evolution for the individual pore radii into account.

Within this work, one upscaled drop volume per grid cell is calculated. We sum up the individual drop volumes that accumulate for each of the pore-size classes to a global drop volume $V_{\text{drop}}^{\text{sum}}$. In each time step, the fate of the individual drops depending on the respective mean pore radius \bar{r}_{pore} is determined. The upscaled drop volume is updated accordingly, and then used to compute the sink term which depends on the detached drop volume. With this approach, a broader variety of drop sizes can be taken into account, yielding more precise information since we do not have to average these values over several grid cells.

6.6.3 Extrusion factors

The balance equations and coupling conditions in the previous sections are originally formulated for three-dimensional control volumes. Intrinsic fluid properties such as density (mass per volume) are also defined in a three-dimensional way. Therefore, all one- or two-dimensional model domains are expanded to three dimensions by so-called extrusion factors in DuMu^x, our numerical framework (see Section 4.3.3).

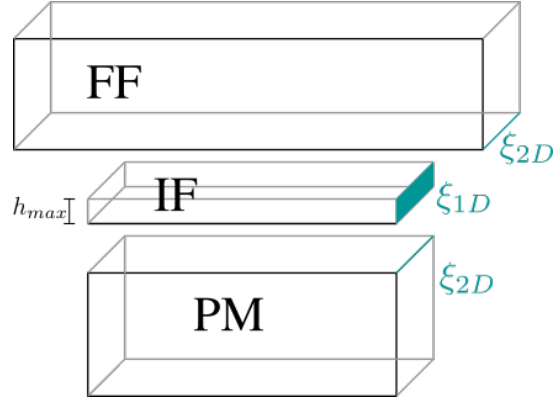


Figure 6.10: Extrusion factors for one- and two-dimensional domains

The extrusion factor ξ_{2D} of a two-dimensional domain has the unit m, and extrudes the domain by the length ξ_{2D} in the third dimension (z -direction). A one-dimensional domain is extruded by a factor ξ_{1D} with the unit m^2 , which represents an extrusion in the second and third dimension (y - and z -direction) simultaneously. This means, that the cross-sectional area of the now three-dimensional domain is equal to ξ_{1D} . These factors are used to compute three-dimensional volumes when integrating over the control volumes to assemble the local residuals. However, the flow and transport processes are still assumed to be one- and two-dimensional respectively.

When coupling model domains of different dimensions, the extrusion factors have to be chosen in a consistent way. In our case, the extrusion of the interface domain in y -direction is prescribed by the height of the biggest drop. Therefore, the extrusion factor for the interface domain has to be defined as $\xi_{1D} = h_{\text{drop}} \cdot \xi_{2D}$, such that all domains are extruded equally in the third dimension, as shown in Figure 6.10.

6.6.4 Workflow

In each time step, the Newton solver solves the global nonlinear system with the three-domain Jacobian matrix (Figure 6.8) as explained for the simple coupling concept in Section 4.3.2. Then, the droplet-related processes are computed with the macro-scale solution for the current time step. Each interface grid cell is coupled to one free-flow and one porous-medium grid cell respectively. Therefore, each grid cell is treated as an REV with several pores, according to the given pore-scale distribution in the problem at hand.

The overall procedure for each time step is

1. solve nonlinear problem with a_g and a_l from previous time step,
2. evaluate drop formation, growth and detachment with pressures and fluxes from current time step,
3. update a_g and a_l for the next time step.

The workflow for the second step in in case of a single pore-size class is shown in Figure 6.11.

In case of different pore-size classes, the workflow becomes more complex. However, since the overall procedure is the same as for a single pore-size class, we omit the details here.

Summary

In this chapter, the multi-scale coupling concept which includes drops in an additional lower-dimensional interface domain into the coupled free-flow/porous-medium-flow system is presented. First, the continuity of fluxes and the balance of normal forces for drops at the interface between the two macro-scale flow compartments are discussed on the pore-scale. Then, the pore-scale knowledge is transferred to the REV-scale to obtain a consistent model concept. Balance equations for a full-dimensional interface are formulated and then reduced by one dimension since it is not necessary to resolve the interface in the vertical direction. Not only vertical mass fluxes between free flow and porous medium across the interface are taken into account, but also lateral mass fluxes along the interface which result from merging drops. The coupling conditions for mass, momentum and energy are taken from the simple coupling concept and extended to take the drops into account. In the last section, the necessary extensions of the numerical model are explained and the workflow to integrate the droplet-related computations into the overall procedure is described. The results obtained with the numerical model are shown in Chapter 8.

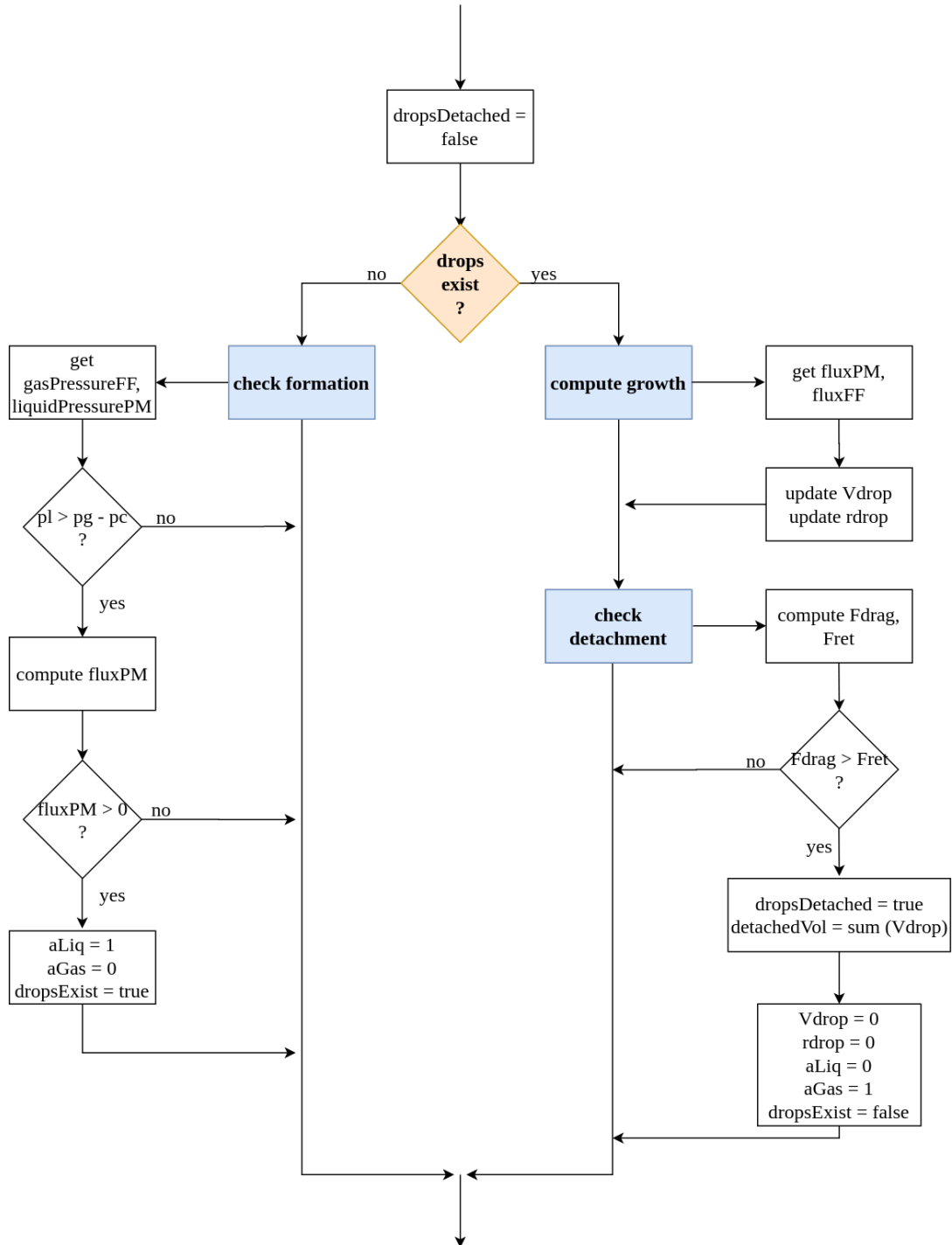


Figure 6.11: Workflow to compute the droplet-related processes for each grid cell

7 Coupling concept with drops in a phase-field model domain

Upscaling droplet-related processes to the macro-scale inevitably leads to a loss in pore-scale information. As an alternative, we present a multi-scale approach in which processes on both scales are modeled separately. While free flow and flow in a porous medium are described on the REV-scale, the droplet-related processes are taken into account on the pore-scale by computing individual drops. This approach was developed and implemented in a joint work with Lukas Ostrowski within the framework of the International Research Training Group DROFIT *. The considerations presented in this chapter are also published in Ackermann et al. [2021c].

An isothermal coupled free-flow/porous-medium-flow system is considered in the following. Two-phase flow is assumed in the porous medium, while the free-flow consists of a gas phase only. We refer to the gaseous phase as vapor in the following to stress that both phases consist of the same component.

In this coupling concept, drops at the common interface are modeled on the pore-scale with the help of a phase-field model as presented in Section 7.1. Initially, the idea was to model the macro-scale flow and transport processes as described in Sections 3.1 and 3.2. However, compatibility issues arise when comparing the macro-scale concept with the pore-scale phase-field model. Due to their different conceptual backgrounds, the models differ with respect to several issues, which are explained and resolved in Section 7.2. With the respective adaptations the models become compatible, and the exchange of mass and momentum between the two scales can be described with the coupling concept outlined in Section 7.3. Details of the numerical implementation as well as technical aspects are explained in Section 7.4.

*<https://www.project.uni-stuttgart.de/dropit/>

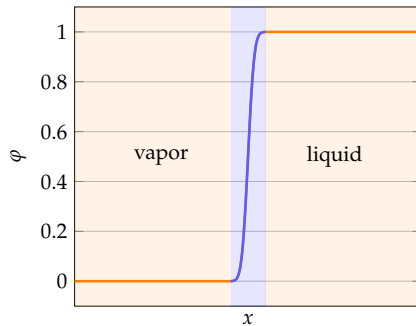


Figure 7.1: Phase transition

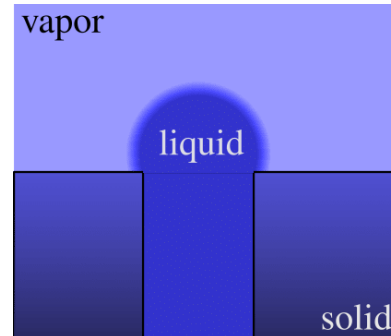


Figure 7.2: Phase-field model domain

7.1 Phase-field model

The phase-field model represents a diffuse interface approach which we apply to model the multi-phase flow processes on the pore-scale in the following. In contrast to sharp-interface models, diffuse-interface models are able to handle complex interface morphologies or topological changes. A comprehensive review on diffuse-interface models is given by Anderson et al. [1998].

In the phase-field model, a transition region of thickness $x_{\text{trans}} > 0$ between vapor and liquid instead of a sharp phase interface is assumed. The smooth transition from vapor to liquid and vice versa is modeled with the help of the phase-field variable $\varphi \in [0, 1]$ as shown in Figure 7.1. If $\varphi = 1$, only the liquid phase is present, for $\varphi = 0$ only vapor exists. The zone in between with $0 < \varphi < 1$ is assumed to be a diffuse interface region where both phases are present. Phase-field models are based on an energy principle, fulfill the second law of thermodynamics as well as a dissipative entropy inequality. Further details on the theoretical background of phase-field models in general are presented by Cahn and Hilliard [1958].

In contrast to sharp interface models, one set of equations is sufficient to describe the flow processes between the two phases. The phase-field variable φ accounts for the presence of each phase respectively.

In the following, we define one pore-scale *cell problem* for each drop. The corresponding model domain is depicted in Figure 7.2. Even though this allows to take different pore geometries into account, we assume for now that all pores and therefore all cell problems have the same geometry. The pore throats are assumed to be connected to a porous medium, while the atmosphere surrounding the drops is part of a free-flow domain.

Under the assumption of a compressible and viscous fluid, an isothermal Navier-Stokes-Allen-Cahn model is considered (Dreyer et al. [2014]). For the primary variables density ϱ , velocity \mathbf{v} and phase-field φ , the respective balance equations are given as

$$\frac{\partial \varrho}{\partial t} + \nabla \cdot (\varrho \mathbf{v}) = 0, \quad (7.1)$$

$$\frac{\partial(\varrho \mathbf{v})}{\partial t} + \nabla \cdot (\varrho \mathbf{v} \mathbf{v}^T + p \mathbf{I}) = \nabla \cdot \mathbf{S} - \psi \nabla \cdot (\nabla \varphi \nabla \varphi^T), \quad (7.2)$$

$$\frac{\partial(\varrho \varphi)}{\partial t} + \nabla \cdot (\varrho \varphi \mathbf{v}) = -\eta \chi, \quad (7.3)$$

with the capillary parameter ψ , the (artificial) mobility η and the generalized chemical potential χ . The dissipative viscous part of the stress tensor in Equation (7.2) is given as $\mathbf{S} = \mathbf{S}(\varphi, \nabla \mathbf{v}) = \mu(\varphi)(\nabla \mathbf{v} + \nabla \mathbf{v}^T)$, with the viscosity $\mu(\varphi) = h(\varphi)\mu_l + (1 - h(\varphi))\mu_g > 0$, interpolated by the function $h(\varphi) = 3\varphi^2 - 2\varphi^3$.

The Helmholtz free energy density w is defined with the help of the specific free energy $f(\varrho)$ as

$$w(\varrho, \varphi, \nabla \varphi) = h(\varphi)\varrho f_l(\varrho) + (1 - h(\varphi))\varrho f_g(\varrho) + \frac{1}{\psi}W(\varphi) + \frac{\psi}{2}|\nabla \varphi|^2, \quad (7.4)$$

with the nonlinear interpolation function h as given above and a mixing energy (Cahn and Hilliard [1958]) using the double well potential $W(\varphi) = \varphi^2(1 - \varphi)^2$.

The hydrodynamic pressure p is given by the thermodynamic relation

$$p = p(\varrho, \varphi) = -w(\varrho, \varphi) + \varrho \frac{\partial w}{\partial \varrho}(\varrho, \varphi), \quad (7.5)$$

and the generalized chemical potential which steers the phase-field variable into equilibrium is defined as

$$\chi = \frac{1}{\psi}W'(\varphi) + \frac{\partial(\varrho \psi)}{\partial \varphi} - \psi \Delta \varphi. \quad (7.6)$$

Further details on the compressible Navier-Stokes-Allen-Cahn model are given by Blesgen [1999]. The presented phase-field model is described in more detail by Ostrowski et al. [2020]. A description of the initial and boundary conditions as well as the numerical model are published by Ackermann et al. [2021c].

7.2 Model compatibility

The approach presented in this chapter combines two models which operate on different length scales to a multi-scale coupling concept which takes the interaction between pore-scale drops and macroscopic free flow and flow in porous media into account. When comparing the model concepts for the macro-scale (Sections 3.1 and 3.2) with the model concept applied on the pore-scale (Section 7.1), differences with respect to fluid properties and primary variables become obvious. In order to obtain a compatible multi-scale approach, a few adaptations in at least one of the two model concepts become necessary. In the following, we mention the common assumptions of both submodels first, before discussing the differences and respective adaptations.

Common assumptions

We assume isothermal conditions and viscous, compressible fluids in both submodels. In addition, the same parameter values are used on both scales. If a parameter depends on the length scale, a scaling factor is applied to obtain its counterpart on the respective other scale. In general, several cell problems are associated with a single REV on the macro-scale. Since we consider two-dimensional flows, the drops are assumed to be cylindrical with unit length in z-direction.

Fluid properties

The balance equations for the macro-scale presented in Chapter 3 consider a compositional fluid system with two components present in each phase, under nonisothermal conditions. The phase-field model which is used for the multi-scale coupling concept is designed to model a fluid where both phases consist of the same component, e.g. liquid water and water vapor. In addition, nonisothermal processes cannot yet be taken into account. Therefore, the macro-scale balance equations are reduced to a single-component two-phase fluid under isothermal conditions.

The density ratio between liquid water and water vapor is $\varrho_l^{\text{H}_2\text{O}}/\varrho_g^{\text{H}_2\text{O}} \approx 1000$. Due to numerical difficulties, the phase-field model can only handle ratios of $\varrho_l/\varrho_g = 1$, which cannot be observed for any real fluid. Therefore, an artificial fluid system is defined

for both the pore- and the macro-scale. The equation of state used for the pressures resembles a stiffened gas:

$$\begin{aligned} p_l(\varrho_l) &= 5\text{m}^2/\text{s}^2\varrho_l - 5.5\text{kg}/(\text{m s}^2) , \\ p_g(\varrho_g) &= 1.5\text{m}^2/\text{s}^2\varrho_g - 0.084\text{kg}/(\text{m s}^2) . \end{aligned} \quad (7.7)$$

These values are derived with the help of an equilibrium condition, which also results in the equilibrium density values $\varrho_l \approx 1.2\text{kg}/\text{m}^3$ and $\varrho_g \approx 0.3\text{kg}/\text{m}^3$. The viscosities are set to $\mu_g = 0.0125\text{kg}/(\text{m s})$ and $\mu_l = 1.025\text{kg}/(\text{m s})$, the temperature is assumed to be $T = 1\text{K}$ and the molar mass is $M = 1\text{kg}/\text{mol}$. Again, we want to stress that these quantities do not resemble a physical fluid and are only used to test the conceptual idea of the multi-scale coupling approach. With these fluid properties, only a qualitative analysis of the interactions between drops and macro-scale flow regimes can be conducted.

Primary variables

For an isothermal system with an immiscible fluid, only the gas-phase pressure p_g^{ff} and the velocity \mathbf{v}_g^{ff} are primary variables in the free-flow domain. The primary unknowns in the porous medium are the gas-phase pressure p_g^{pm} as well as the liquid saturation S_l . The phase-field balance equations are solved for the density ϱ , the pore-scale velocity \mathbf{v} and the phase-field variable φ . Pressures and densities can be converted into each other with the equation of state (7.7). For the velocities, the free-flow velocity \mathbf{v}_g^{ff} complies with the phase-field velocity \mathbf{v} . The flow velocities in the porous medium $\mathbf{v}_\alpha^{\text{pm}}$ can be computed as secondary variables with Darcy's law (Equation 3.6). Dividing them by the porosity Φ yields the pore-scale velocities, which correspond to the phase-field velocity. The phase-field variable φ as well as the macro-scale saturation S_l do not have corresponding quantities in the respective other model concept.

Length scales

The assumptions made for the free-flow as well as the porous-medium-flow model are valid on spatial scales of centimeters to kilometers. The phase-field model is developed for the range of micrometers to millimeters. Within an area of a few square-centimeters of a porous surface, hundreds of pores might be present. We combine the different length

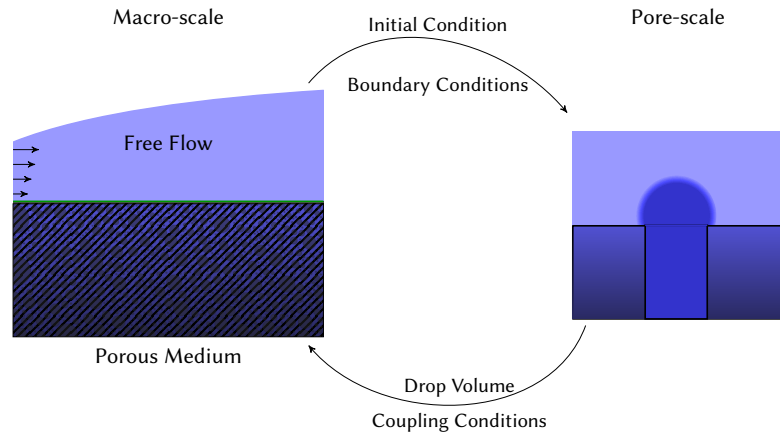


Figure 7.3: Exchange of boundary values between the two scales

scales in the scope of this work by coupling several cell problems to a each pair of adjacent macro-scale grid cells on both sides of the interface.

7.3 Coupling concept with phase-field model

The multi-scale coupling concept is based on the iterative data exchange between the macro-scale and the pore-scale model. With an explicit coupling in time, the same time step is computed separately in each model. Figure 7.3 shows the main principle for the exchange. The aim is to replace all coupling conditions for the macro-scale model as listed in Section 4.2 by data obtained with the pore-scale model. Vice versa, the pore-scale model is supposed to be initiated with data from the macro-scale model only, without the need to choose any values manually. Achieving this goal would result in a very complex coupling scheme, including appropriate scalings and conversions. Therefore, we begin with a simplified version to obtain a first impression on the mutual influence of the processes on both scales.

In a first simplified approach, the drop geometry does not interfere with the free flow. Therefore, the respective coupling conditions on the free-flow side of the common interface are evaluated as given in Section 4.2. However, the balance between the free-flow velocity-dependent drag force and the retention force determines the drop detachment as explained in Section 5.2.

To obtain a coupled model, we partly consider the interactions between porous medium and drops in our coupling concept. For the pore-scale cell problem, the Darcy velocity

at the upper boundary of the porous medium is converted to the pore-scale velocity via $\mathbf{v}_i^{\text{pore}} = \mathbf{v}_i^{\text{pm}}/\Phi$. This value is set as a Dirichlet boundary value for the phase-field velocity at the lower end of the pore. Depending on this velocity, the evolution of the drop volume on the pore-scale can be determined by computing the flux across the lower pore-throat boundary. The drop volume is computed as

$$V_{\text{drop}} = 2 \int_{\Omega_{\text{micro}}} \varphi d\mathbf{x} - d_{\text{pore}} h_{\text{pore}}, \quad (7.8)$$

where Ω_{micro} is the computational domain of the cell problem and h_{pore} denotes the height of the pore. Since the drops are assumed to be symmetric, the computational domain considers only half a drop. Therefore, the phase-field integral is multiplied by 2 to obtain the full drop volume.

The drop volume is then handed back to the macro-scale model, which reconstructs the drop radius and computes the force balance to determine if the drop detaches (see Equation (5.15): $F_{\text{drag}} > F_{\text{ret}}$). In case of detachment, the macro-scale model applies the sum of the detached drop volumes of all pores within the REV as the sink term near the upper boundary of the porous medium to account for the respective mass loss.

7.4 Numerical model

Besides the differences in the conceptual models, the numerical models employed by the two submodels in the presented multi-scale coupling approach differ: The phase-field model is implemented in FEniCS*, which is an open-source computing platform for solving partial differential equations, written in Python. Further details on FEniCS are described by Alnæs et al. [2015]. For the macro-scale model, we use DuMu^x, an open-source simulator for flow and transport processes in porous media and free-flow scenarios. Details on the numerical model in DuMu^x are already given in Section 6.6.

Both implementations depend on several packages and require tedious installation procedures. Therefore, we build a Docker[†] container which contains an installation script to download the needed files and compile the DuMu^x core. This allows to build and run the implementation of the multi-scale concept without further knowledge of any of the two base implementations.

*<https://fenicsproject.org/>

†<https://docs.docker.com/>

The sequential coupling scheme is implemented with the following procedure. Before the time loop starts, DuMu^x initiates FEniCS and prepares the data and control pipes for the inter-process communication. Then, in each time step,

1. DuMu^x calls FEniCS with macro-scale information from current time step,
2. FEniCS computes the pore-scale solution for the current time step,
3. FEniCS hands pore-scale information to DuMu^x,
4. DuMu^x adapts boundary values and drop information for the next time step,
5. DuMu^x computes the macro-scale solution for the current time step.

Consequently, the overall simulation is steered by DuMu^x. Its Newton solver determines the time step sizes Δt , which are included in the data given to FEniCS such that both models compute the same time steps. The simulation time t_{end} is set as an input parameter for DuMu^x.

Summary

In this chapter, an approach to combine two existing models which operate on different spatial scales to a multi-scale coupling for coupled free-flow/porous-medium-flow problems under the influence of drops is presented. The drops are modeled on the pore-scale with the help of a phase-field model, which was implemented by Lukas Ostrowski. For the coupled system, the simple coupling concept is taken as a base and extended such that it can exchange information with the pore-scale model. This data exchange is currently limited to the liquid velocity from the porous medium into the surface pore as well as the resulting drop volume. The respective exchange procedure and the corresponding workflow of the numerical model are also outlined in this chapter. The results obtained with the numerical model are presented in Chapter 8.

8 Simulation results

In the previous chapters, three different model concepts for coupled free-flow/porous-medium-flow systems have been presented: a simple coupling concept (Chapter 3), as well as two complex multi-scale coupling concepts (Chapters 6 and 7) which take the influence of interfacial drops into account. In the following, the results of numerical simulations with the two multi-scale models are shown to investigate their validity, performance and capabilities. The respective results are then discussed and partly compared with the simple coupling concept to estimate the influence of the interfacial drops. The aim of this chapter is to investigate the applicability of the respective model concepts and their future perspectives.

The main part of the following sections covers the results obtained with the *Lower-Dimensional Interface Domain* (LDID) multi-scale coupling concept. Section 8.1 contains a comparison with an experimental set-up for a simple drop formation and growth scenario. In Section 8.2, two reference cases are presented and a parameter study is conducted to investigate the formation, growth and detachment in multi-drop settings. Merging drops are considered in Section 8.3, where we determine if and when drops touch and therefore cover the whole interface area. In Section 8.4, lateral fluxes along the interface are taken into account. Finally, the results obtained with the LDID multi-scale coupling concept are compared to the results produced with the simple coupling concept in Section 8.5. The software code to reproduce the results presented in Sections 8.1 to 8.5 is published under <https://git.iws.uni-stuttgart.de/dumux-pub/ackermann2020a>.

At the end of this chapter, results obtained with the *Phase-Field Model* (PFM) multi-scale coupling concept are presented and discussed in Section 8.6.

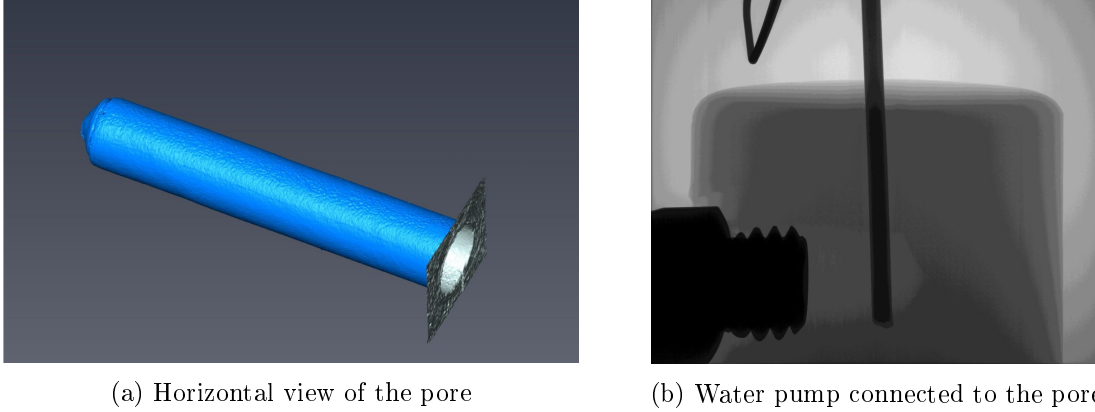


Figure 8.1: The pore in the experimental set-up

8.1 Comparison with experiment

An experimental set-up is used to assess if the results obtained with the LDID multi-scale coupling concept presented in Chapter 6 match the behavior of a real drop. The experiment was conducted by Dr. Ing. Stephanie Fest-Santini at the Department of Management, Information and Production Engineering of the University of Bergamo, Italy. Further details about this comparison are published by Ackermann et al. [2021b]. In the following, the set-ups for both the experiment and the simulation are outlined. Then, we compare the measured and computed data, and discuss the results.

8.1.1 Experimental set-up

A pore with a length of $7.92 \cdot 10^{-3}\text{m}$ and a diameter of $1.495 \cdot 10^{-3}\text{m}$ as shown in Figure 8.1a was drilled into a cylindrical Teflon* block with a diameter of $d_{\text{block}} = 0.03\text{m}$ and a height of $h_{\text{block}} = 0.015\text{m}$. A high precision peristaltic pump (Ismatec REGLO Digital MS-2/12) was connected to the lower end of the pore to maintain a continuous mass flux into the pore, see Figure 8.1b. The liquid consists of a mixture of pure water and potassium iodide with a mass ratio of 6:1.

Initially, the pore is completely filled with air. At $t = 0\text{s}$, the pump starts to inject the liquid with a constant rate of $q_{\text{pump}} = 8.85 \cdot 10^{-10}\text{m}^3/\text{s}$ into the pore. The calculated standard deviation is $4.83 \cdot 10^{-11}\text{m}^3/\text{s}$.

*Polytetrafluoroethylene

8.1.2 Simulation set-up

For the simulation, a porous medium has to be defined instead of a solid block with a single pore. We set up a two-dimensional domain with the dimensions $l_x = 5 \cdot 10^{-3}\text{m}$ and $l_y = 30 \cdot 10^{-3}\text{m}$, as shown in Figure 8.2. As mentioned in Section 6.6.3, the domain is extruded to the third dimension automatically. The extrusion factor is set to $\xi_{2D} = 5 \cdot 10^{-3}\text{m}$, leading to an interfacial area of $25 \cdot 10^{-6}\text{m}^2$. The initial saturation is set as $S_l^{\text{pm}} = 0.99$. The pump is modeled with a Neumann boundary condition at the lower boundary of the porous medium. The measured inflow rate $q_{\text{pump}} = 8.85 \cdot 10^{-10}\text{m}^3/\text{s}$ is set as the corresponding boundary value.

In the interface domain, a single pore-size class with the radius $r_{\text{pore}} = 7.475 \cdot 10^{-4}\text{m}$ is defined. The number of pores is manually set to 1. Since the only pore that is present is filled with liquid, no gaseous mass flux can occur between porous medium and interface. Consequently, no gas flux takes place between free flow and interface either, since we assume isothermal conditions where evaporation from the drop is neglected.

The velocity in the free-flow domain is set to zero in accordance with the experimental set-up. Therefore, no pressure jump occurs across the boundary between free-flow and interface domain. Since the initial values for the gas-phase pressure are set equally, the free-flow domain does not interact with the interface domain, which matches the experiment.

Even though the contact angle θ varies in the experiment, we assume θ to be constant in the simulation for the sake of simplicity. While the contact angle measured directly after the drop formation is $\theta_0 = 57.6^\circ$, it is above $\theta = 110^\circ$ for the rest of the experiment. Therefore, we average over the contact angle values between the second and the last measurement, which yields $\theta = 140^\circ$ for the simulation.

Further initial and parameter values are listed in Table 8.1. Spatial parameters such as porosity Φ and intrinsic permeability \mathbf{K} are chosen randomly, since the Teflon block does not resemble a porous medium. Gravity is taken into account in the macro-scale domains for a realistic replication of the experimental conditions.

Primary variable	value	unit
p_g^{ff}	10^5	Pa
\mathbf{v}_g^{ff}	0	m/s
$X_g^{w,\text{ff}}$	0.1	-
p_g^{if}	10^5	Pa
S_l^{if}	0	-
p_g^{pm}	10^5	Pa
S_l^{pm}	0.99	-
Parameter	value	unit
Φ	0.07	-
\mathbf{K}	10^{-10}	m^2
T	293.15	K
\mathbf{g}	$(0, -9.81)^T$	m/s^2
θ	140	$^\circ$

Table 8.1: Initial and parameter values

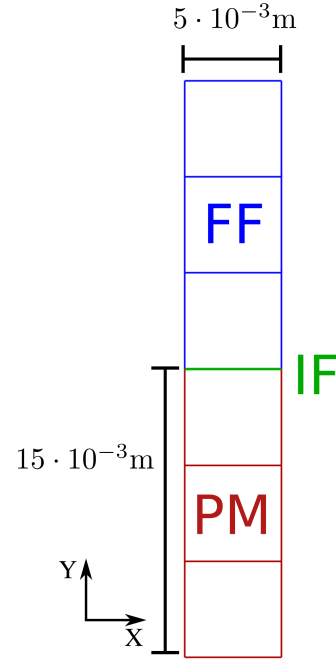


Table 8.2: Model domain for the comparison with experimental data

8.1.3 Results

A series of 2D X-ray images showing the drop evolution was recorded throughout the drop growth, see Figure 8.2. Detailed information regarding the components of the microtomography unit is published by Santini et al. [2013]. From these images, the evolution of the surface profile as well as the drop volume were reconstructed over time. In addition, the drop radius and the contact angle could be computed. The simulation outputs are the evolution of drop volume and drop diameter over time.

Since the pump rate can only be measured with a standard deviation, the simulation was run for three different pump rates q_{pump} . The resulting drop volumes for experiment and simulation are shown in Figure 8.3a.

For spherical drops as assumed in the numerical model, the drop radius r_{drop} can be computed with the drop volume and the contact angle θ between drop and Teflon as

$$r_{\text{drop}} = \sqrt[3]{\frac{3V_{\text{drop}}}{\pi \cdot (1 - \cos(\theta))^2 \cdot (2 + \cos(\theta))}}. \quad (8.1)$$

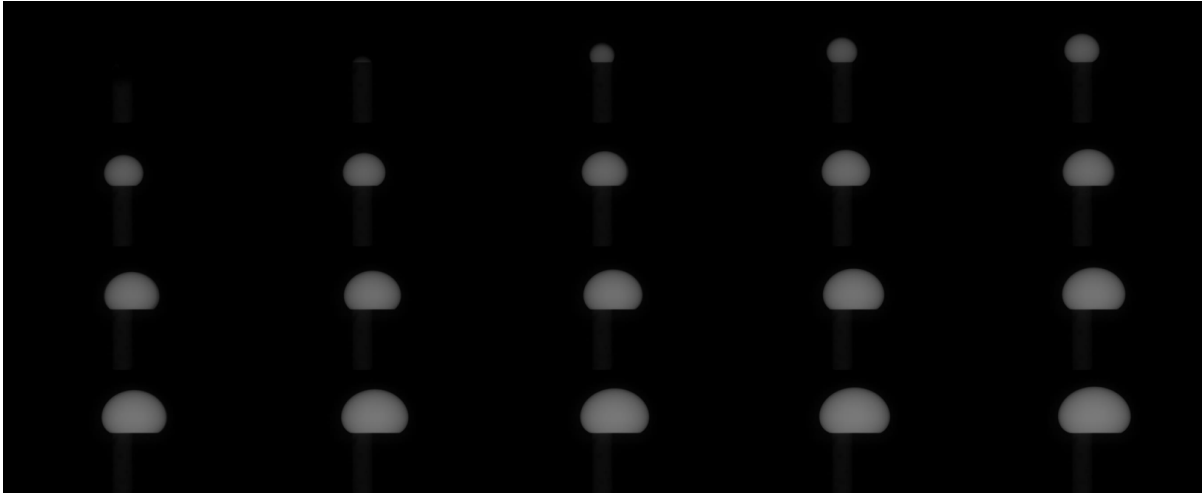


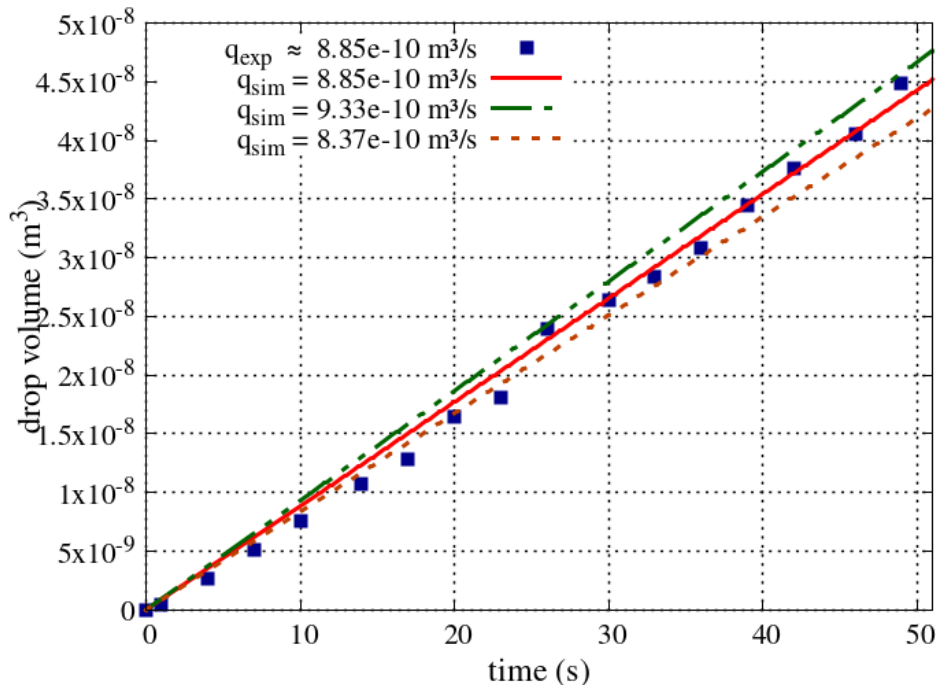
Figure 8.2: Evolution of the drop volume, recorded with X-rays

The radii obtained from the experiment as well as from the simulation are presented in Figure 8.3b.

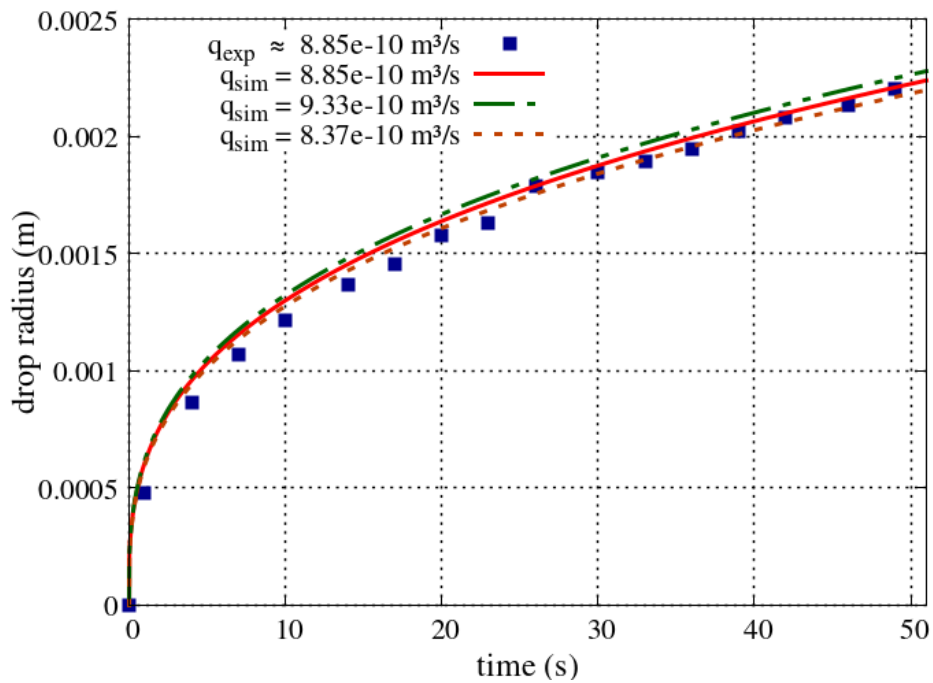
8.1.4 Discussion

The drop volumes for $t = 50\text{s}$ measured in the experiment and computed with the simulation are both approximately $V_{\text{drop}} = 4.5 \cdot 10^{-8}\text{m}^3$. The drop radii are computed based on the drop volume and are consequently almost equal for $t = 50\text{s}$ with $r_{\text{drop}}^{\text{exp}} = 2.27 \cdot 10^{-3}\text{m}$ and $r_{\text{drop}}^{\text{sim}} = 2.22 \cdot 10^{-3}\text{m}$. The difference is most likely caused by the fact that the contact angle varies throughout the experiment, but is assumed to be constant in the simulation. Since the deviation is relatively small, we assume the implementation of the lower-dimensional interface domain coupling concept as suitable to model drop formation and growth processes, even though the individual drops are not resolved.

It has to be kept in mind that the Teflon block with a single pore is modeled as a porous medium in this comparison. However, this simplification does not affect the representation of the drop formation and growth process based on the multi-scale coupling concept.



(a) Drop volumes in experiment and simulation



(b) Drop radii in experiment and simulation

Figure 8.3: Comparison of the results obtained with experiment and simulation

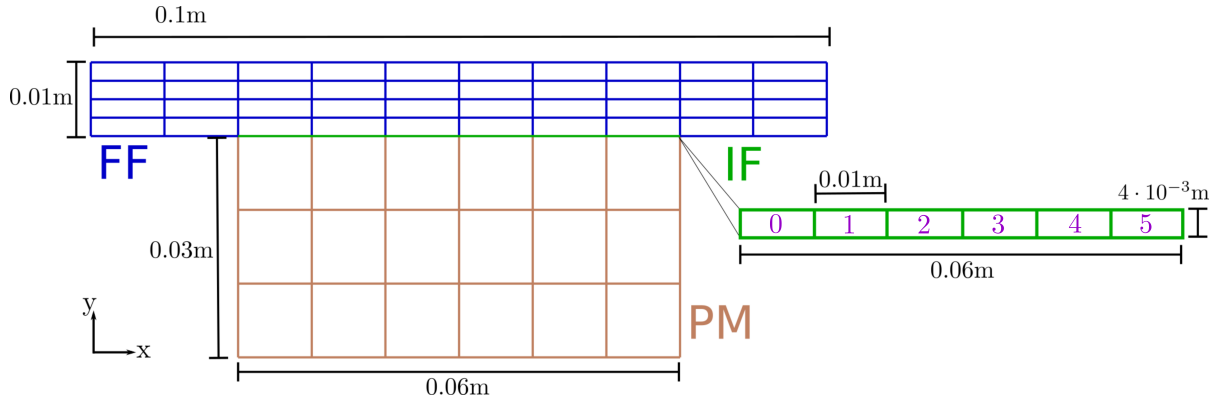


Figure 8.4: Dimensions and discretization of the model domain Ω . The purple numbers indicate the elements in the interface domain.

8.2 Formation, growth and detachment (Lower-dimensional interface)

The results of the previous section have shown that the drop volume predictions by the LDID multi-scale model correspond to realistic values. Therefore, we take more complex scenarios into account to investigate drop formation, growth and detachment.

8.2.1 Model domain set-up and parameter values

The spatial discretization as well as the respective dimensions of the model domain Ω are shown in Figure 8.4. The illustrated two-dimensional domain is extended by $l_z = 0.05$ m into the third dimension as explained in Section 6.6.3. The interface is included as a lower-dimensional domain only, i. e. a one-dimensional domain in our case. However, the corresponding two-dimensional interface domain is shown in Figure 8.4 to illustrate its size compared to the rest of the model domain. A three-dimensional schematic view of a part of the interface domain is given in Figure 8.5. All pores are assumed to be distributed homogeneously with equal distances from each other.

The initial time step size is set to $\Delta t = 5 \cdot 10^{-3}$ s and the simulation is run until $t_{\text{sim}} = 600$ s. On a one-processor machine, this results in a CPU time for the isothermal reference case of $t_{\text{CPU}} = 880$ s \approx 15min. The computing times for more complex cases as the ones presented in the following sections were only slightly higher. Therefore, the computing times are not listed explicitly for each presented case.

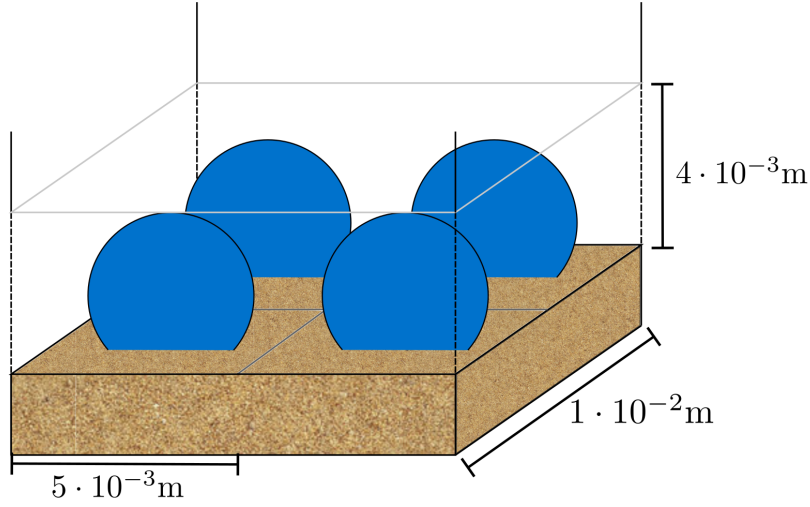


Figure 8.5: Exemplary distribution of drops in a square domain

Usually, the number of surface pores of a porous medium depends on the porosity Φ . However, growing drops might touch and merge if they are too close together due to a high number of pores. Therefore, the number of pores is set manually in the following scenarios to guarantee that the drops do not touch until they are detached.

For the reference case, a single pore-size class with a mean pore radius of $\bar{r}_{\text{pore}} = 10^{-3}\text{m}$ is assumed. The interfacial area per grid cell A_{Γ}^{cell} is given by the interface length l_{Γ} divided by the number of grid cells and multiplied by the extrusion factor ξ_{2D} :

$$A_{\Gamma}^{\text{cell}} = \frac{l_{\Gamma}}{n_{\text{cells}}^{\text{if}}} \cdot \xi_{2D} = \frac{0.06\text{m}}{6} \cdot 0.05\text{m} = 5 \cdot 10^{-4}\text{m}^2. \quad (8.2)$$

With the force balance given in Equation (5.15) and the drag coefficient defined as in Equation (5.11), the drop radius in the moment of detachment can be estimated a priori as $r_{\text{drop}}^{\text{detach}} \leq 2.5 \cdot 10^{-3}\text{m}$. The square area corresponding to a drop with this radius is $A_{\text{square}} = (2r_{\text{drop}}^{\text{detach}})^2 = 2.5 \cdot 10^{-5}\text{m}^2$. Therefore, the number of pores is set to $n_{\text{pores}} = \frac{A_{\Gamma}^{\text{cell}}}{A_{\text{square}}} = \frac{5 \cdot 10^{-4}\text{m}^2}{2.5 \cdot 10^{-5}\text{m}^2} = 20$ in the reference case to avoid drop contact before detachment. This corresponds to the sketch in Figure 8.5.

Both interface domain and porous medium are initially assumed to be gas-filled. Therefore, the mass fractions of water in gas X_g^w are set as initial conditions. Due to the liquid inflow at the lower boundary of the porous medium, a two-phase flow establishes and the saturation S_l replaces the mass fraction as a primary variable. The same switch takes place in the interface domain as soon as the drops start to grow. Figure 8.6 illustrates

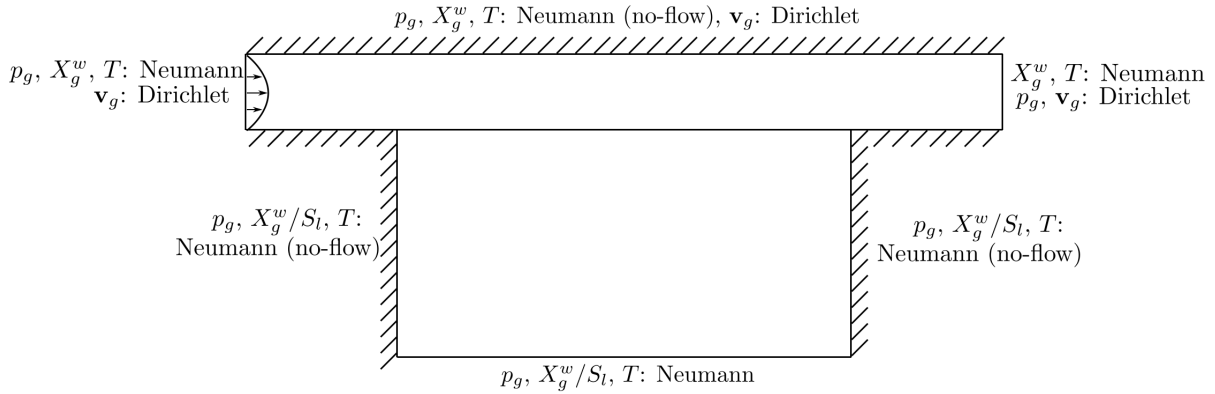


Figure 8.6: Boundary conditions for the reference case

the boundary conditions for the reference case. The initial and boundary values for the reference case are listed in Table 8.3.

8.2.2 Isothermal reference case

In the following, the main results for the isothermal reference case are presented. The results in the individual grid cells are qualitatively equal and only shifted by a few time steps due to numerical inaccuracies. Therefore, only the results of element 3 (see Figure 8.4) are shown representatively.

Drop volume: Drop formation, growth and detachment for the isothermal reference case can be observed in the drop volume evolution in Figure 8.7. It takes a few seconds until the liquid inflow at the bottom boundary of the initially gas-filled porous medium reaches the interface. Then, as soon as the pressure condition is fulfilled, the drops start to grow. At $t \approx 148\text{s}$, the first drops are detached. Due to the constant inflow from below, new drops form immediately. Since the liquid phase is still present in the porous medium below the interface, the new drops grow linearly from the beginning. The volume presented in Figure 8.7 corresponds to an individual drop. For the sink term in case of detachment, the individual drop volumes in each grid cell are added up.

Due to the small time step sizes, the individual data points cannot be distinguished from each other when plotted over larger periods of time. Therefore, continuous lines are used in the following to represent the discrete information obtained in each time step.

Free flow					
p_g	10^5	Pa			
X_g^w	0.01				
v_g	4	m/s			
T	298.15	K	Φ	0.5	
Interface			\mathbf{K}	$2.65 \cdot 10^{-10}$	m^2
p_g	10^5	Pa	θ	130	$^\circ$
X_g^w	0.01		ρ_s	2700	kg/m^3
T	298.15	K	λ_s	2.8	$\text{J}/(\text{m s K})$
Porous medium			c_s	790	$\text{J}/(\text{kg K})$
p_g	10^5	Pa			
X_g^w	0.01				
T	298.15	K			
q_{bottom}	$1 \cdot 10^{-5}$	kg/s			

Table 8.4: Material parameters of the porous medium

Table 8.3: Initial and boundary values for the reference case

Force balance: The balance of horizontal forces acting on each drop is shown in Figure 8.8. The drag force F_{drag} depends on the projected area of the drop and therefore on r_{drop}^2 , while the retention force F_{ret} is directly proportional to the drop radius r_{drop} . As soon as the forces are equal, a drop is detached.

Drop radius: The number of pores in each grid cell is set manually in the reference case to avoid that the drops touch each other before they detach. With a grid cell length of $l_x = 0.01\text{m}$ and two drops next to each other, the maximum drop radius is therefore $r_{\text{drop}}^{\text{max}} = 0.0025\text{m}$. As shown in Figure 8.9, this value is not exceeded in the current set-up. The drop height in the moment of detachment is

$$h_{\text{drop}} = r_{\text{drop}}(1 - \cos(\theta)) = 0.00233(1 - \cos(130^\circ)) = 0.00381\text{m} , \quad (8.3)$$

which fits to the chosen height of the interface domain of $h^{\text{if}} = 0.004\text{m}$.

Liquid saturation: As explained in Section 6.3, the summed up drop volumes are represented by the liquid saturation in the interface domain. The saturation over time is shown in Figure 8.10. With the grid cell length $l_x = 0.01\text{m}$ and the extrusion factor $\xi_{1D} = 2 \cdot 10^{-4}\text{m}^2$, the grid cell is extruded to a volume of $V_{\text{cell}} = 2 \cdot 10^{-6}\text{m}^3$. Figure 8.7 reveals that the drops are detached with an approximate volume of $V_{\text{drop}}^{\text{detach}} = 4.8 \cdot 10^{-8}\text{m}^3$.

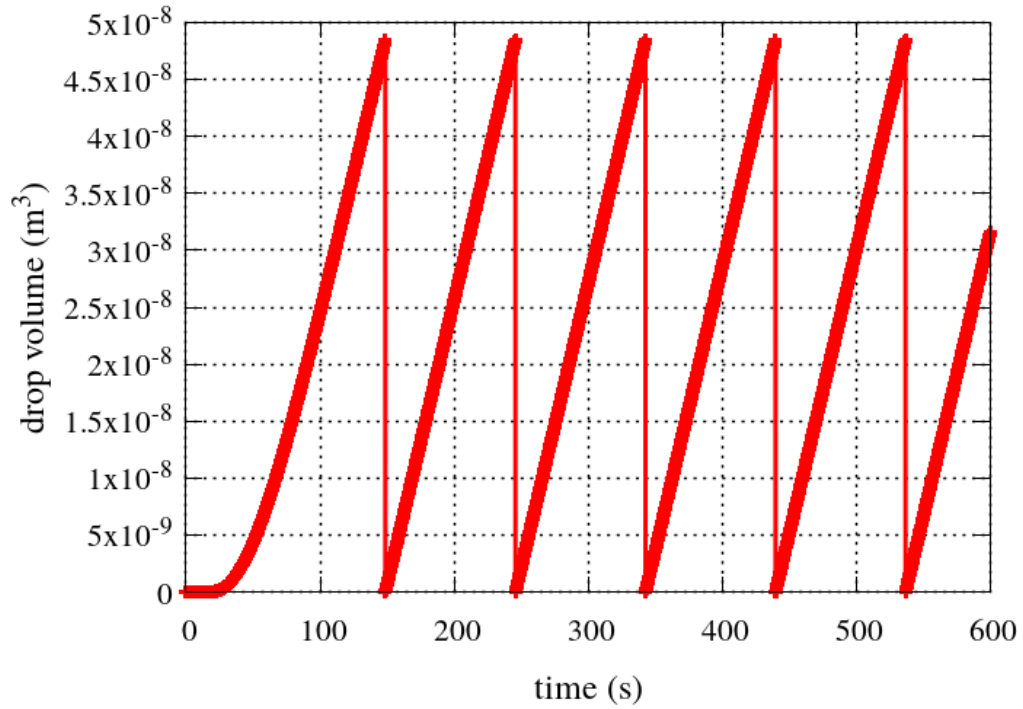


Figure 8.7: Drop volume evolution for the isothermal reference case

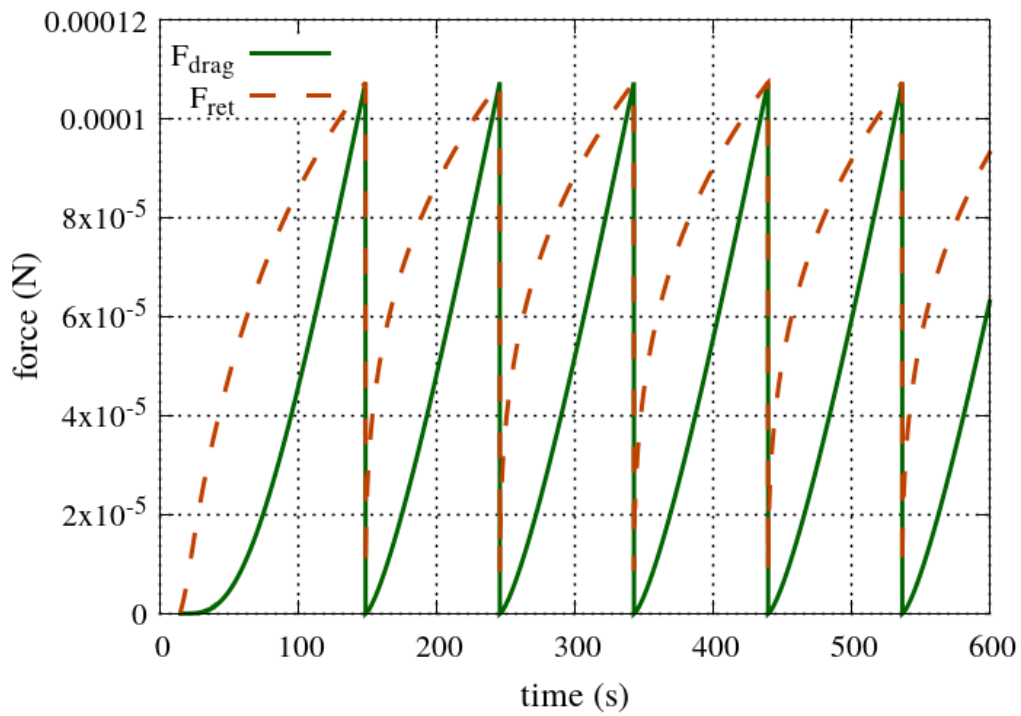


Figure 8.8: Drag and retention force for the isothermal reference case

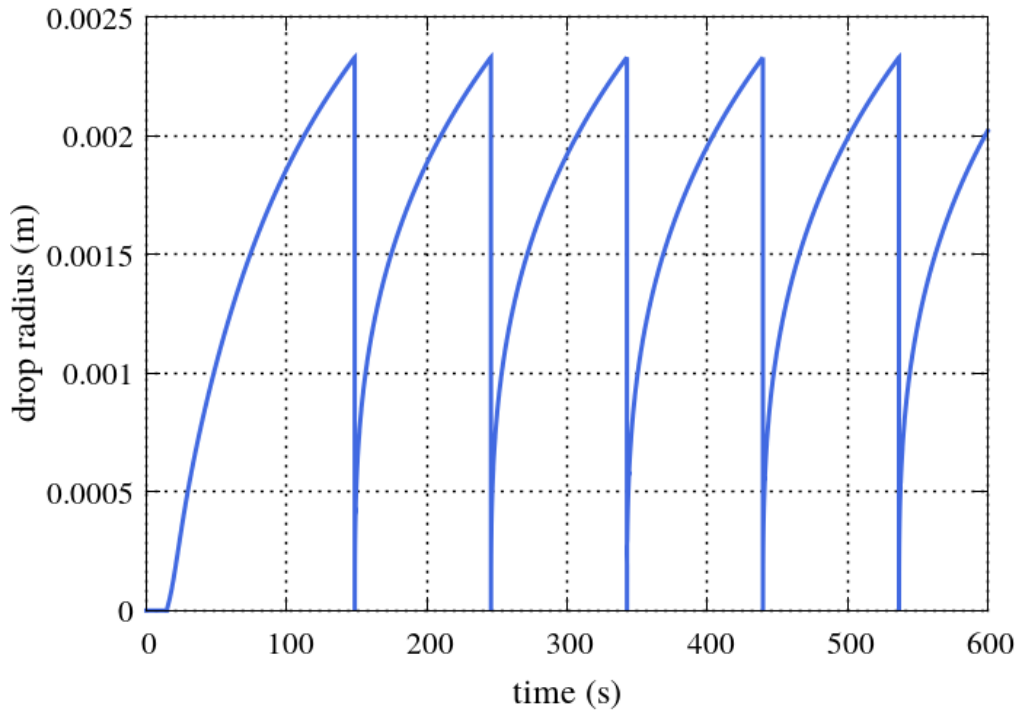


Figure 8.9: Drop radius evolution for the isothermal reference case

Therefore, the saturation right before the detachment can be computed as

$$S_l^{\text{if}} = \frac{V_{\text{drop}}^{\text{detach}} \cdot n_{\bar{r}_{\text{pore}}}}{V_{\text{cell}}} = \frac{4.8 \cdot 10^{-8} \text{m}^3 \cdot 20}{2 \cdot 10^{-6} \text{m}^3} = 0.48, \quad (8.4)$$

which fits to the value of the primary variable S_l^{if} as shown in Figure 8.10.

8.2.3 Nonisothermal reference case

In a nonisothermal setting, the drop volume is additionally influenced by the evaporation rate. Comparing the drop volume evolution for the isothermal and the nonisothermal reference case in Figure 8.11 shows that the evaporative fluxes slow down the drop growth and therefore delay the time of detachment. Higher temperatures lead to higher evaporation rates, which result in slower drop growth rates. Since energy is removed from the system when the drops detach, the temperature decreases with every detachment. Therefore, the surface tension increases slightly, which leads to a higher retention force over time. As a consequence, each drop can grow a little bit larger before being detached, compared to its predecessor.

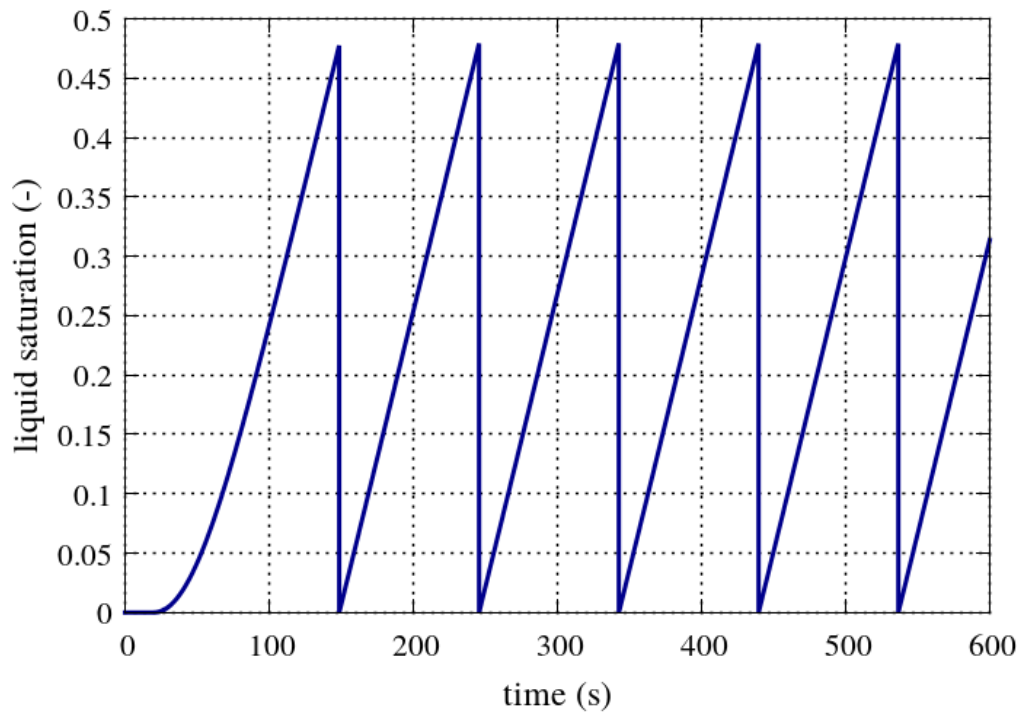


Figure 8.10: Liquid saturation evolution for the isothermal reference case

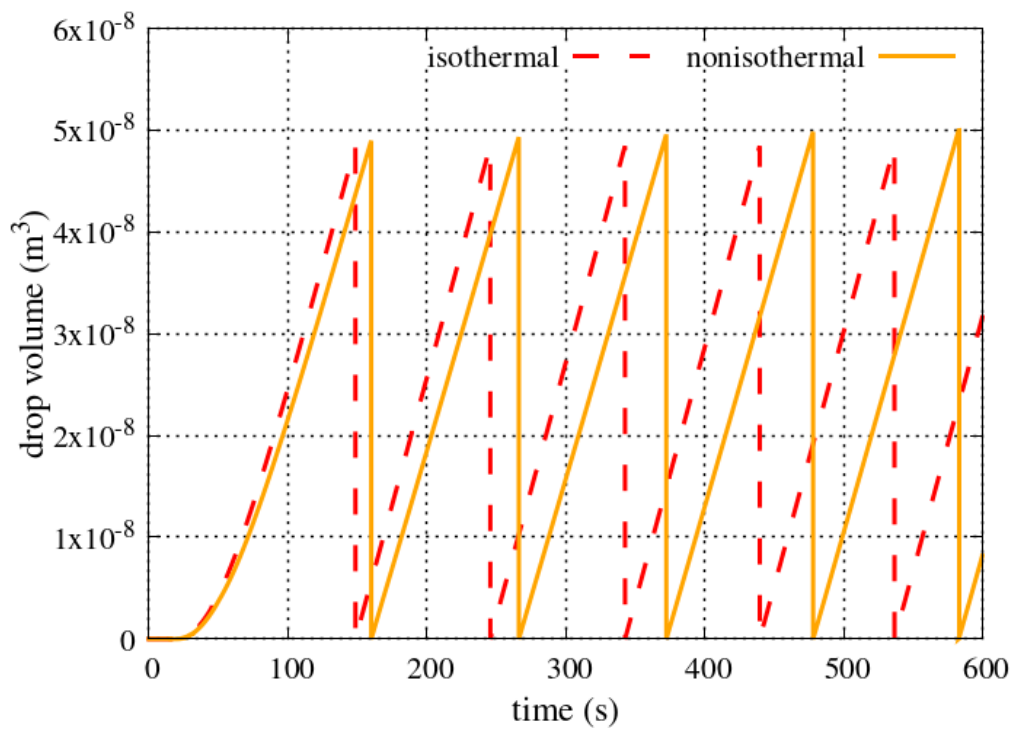


Figure 8.11: Drop volume evolution for the isothermal and nonisothermal case

8.2.4 Different pore sizes

Instead of taking every single pore radius into account, we cluster the pores into so-called pore-size classes with a mean pore radius \bar{r}_{pore} . In a more diverse porous medium than the one assumed in the reference case, it might be appropriate to define several pore-size classes.

In the following, we assume that 30% of the pores belong to a pore-size class with $\bar{r}_{\text{pore}} = 10^{-3}\text{m}$, 10% belong to a pore-size class with $\bar{r}_{\text{pore}} = 10^{-4}\text{m}$ and 60% have a mean radius of $\bar{r}_{\text{pore}} = 10^{-5}\text{m}$. This pore-size distribution is chosen randomly for testing purposes.

Drop volume: Figure 8.12 shows the drop volume evolution for three individual drops belonging to one of the three pore-size classes respectively. Due to the continuous pressure rise in the porous medium even after the first drops have formed, the drop formation condition is fulfilled for $\bar{r}_{\text{pore}} = 10^{-4}\text{m}$ a few seconds later than for $\bar{r}_{\text{pore}} = 10^{-3}\text{m}$. However, the pressure in the porous medium stays approximately constant at $p_l^{\text{pm}} = 1.01 \cdot 10^5 \text{Pa}$, which is not enough for the pores with $\bar{r}_{\text{pore}} = 10^{-5}\text{m}$ to be filled with water.

The mass flux from the porous medium is distributed among the pore-size classes according to the given percentage $f_{\bar{r}_{\text{pore}}}$. Within each pore-size class, it is further distributed equally between the $n_{\bar{r}_{\text{pore}}}$ pores. The resulting additional drop volume per pore is therefore $V_{\text{drop}}^{\text{growth}} = \frac{f_{\bar{r}_{\text{pore}}}}{n_{\bar{r}_{\text{pore}}}} \cdot V_{\text{drop}}^{\text{total}} = 0.05 \cdot V_{\text{drop}}^{\text{total}}$ for each pore. Therefore, identical growth rates can be observed, which differ only in the beginning due to the slight delay in time.

Summing up the individual drop volumes in each pore-size class yields the total drop volume evolution as shown in Figure 8.13. As mentioned before, the percentage $f_{\bar{r}_{\text{pore}}}$ determines the total volume per pore-size class.

8.2.5 Parameter study

In the following, a selection of results obtained with varying parameters is presented to determine the influence of the respective parameters.

Varying inflow rate: Figure 8.14 shows the drop volumes which result from varying inflow rates at the bottom boundary of the porous medium. A smaller inflow rate of $q = 0.5 \cdot 10^{-5} \text{kg/s}$ results in a slower growth rate compared to the reference case with

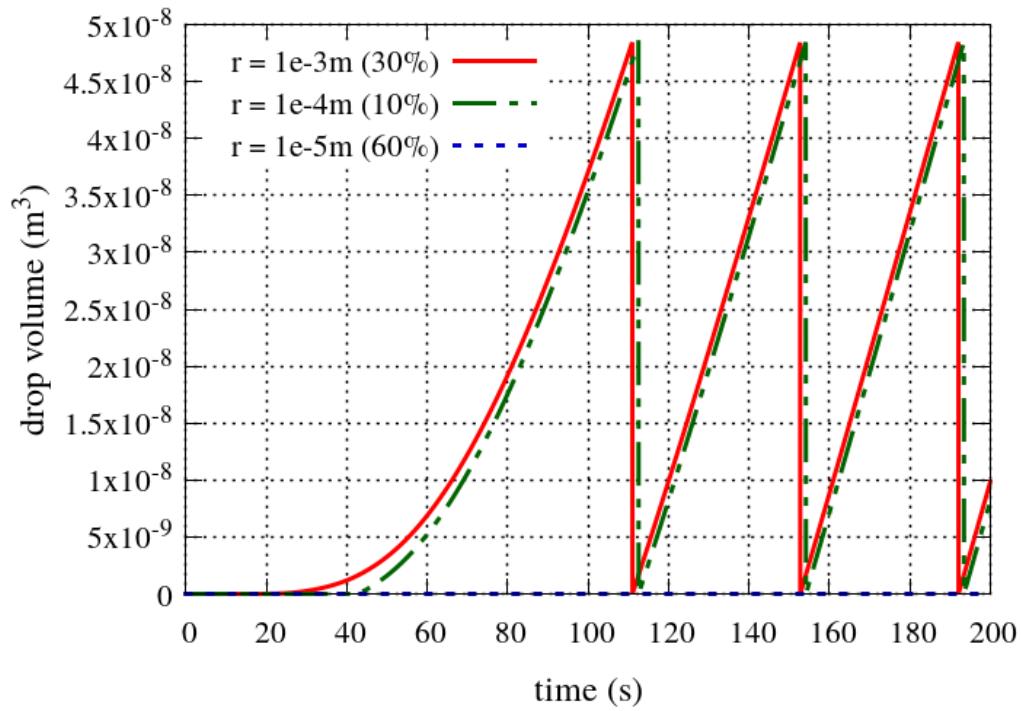


Figure 8.12: Individual drop volumes for different pore-size classes

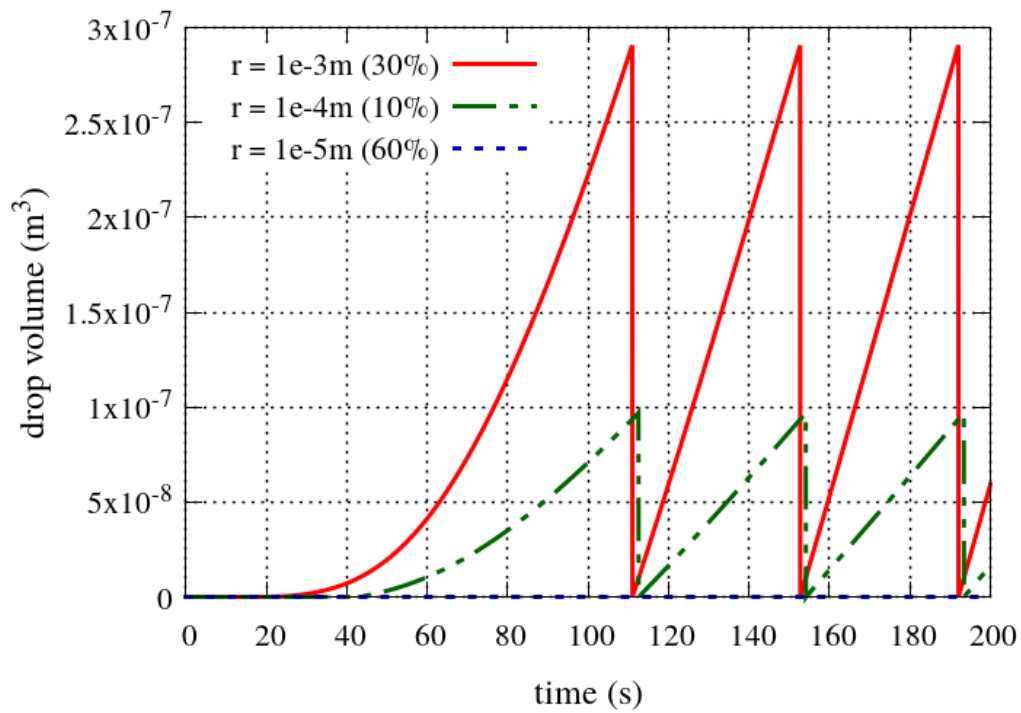


Figure 8.13: Total drop volumes for three different pore-size classes

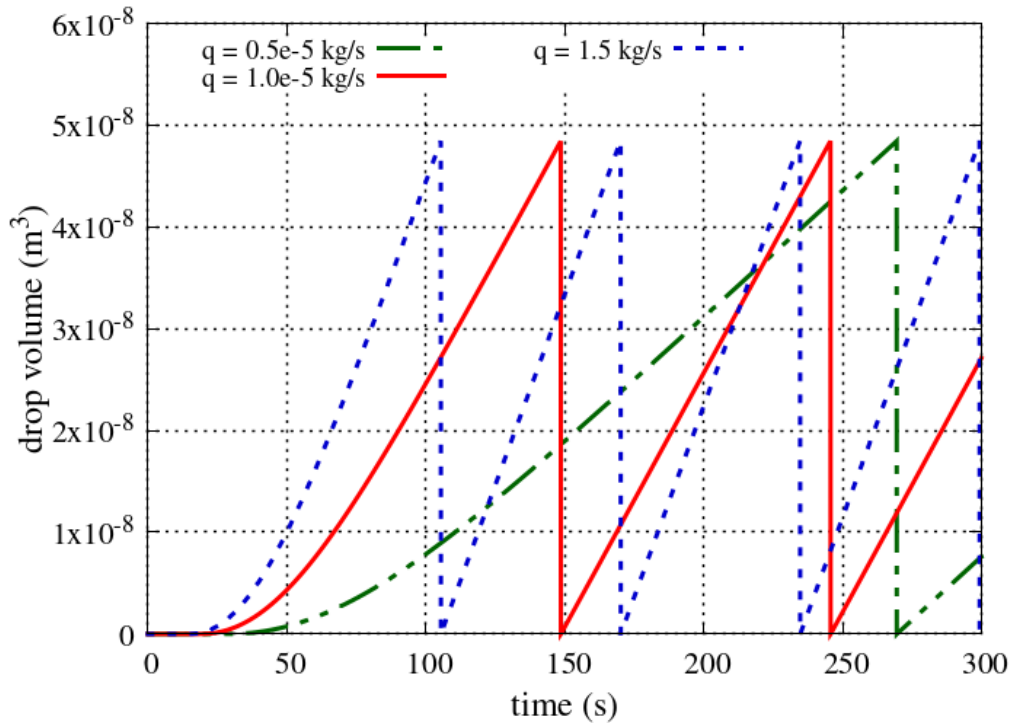


Figure 8.14: Variation of inflow rates

$q = 1 \cdot 10^{-5} \text{kg/s}$. For a higher rate of $q = 1.5 \cdot 10^{-5} \text{kg/s}$, the drops grow faster. Since the detachment criterion does not depend on the growth rate, all drops are detached at the same volume.

Varying free-flow velocity: The free-flow velocity directly influences the detachment of the drops, since the drag force depends on the squared horizontal velocity component v_x^2 . The results for higher, respectively lower, free-flow velocities than set in the reference case are presented in Figure 8.15. Note that for $v = 3.5 \text{m/s}$, the corresponding drop radius before detachment is $r_{\text{drop}}^{\text{detach}} = 0.00251 \text{m}$. This means that the drops would touch before they are detached and should no longer be treated as spherical segments. The results for touching and merging drops are investigated in the next section.

Varying temperature: Under nonisothermal conditions, evaporation from drops influences the growth rates. Figure 8.16 illustrates the influence of the temperature on the drop volume evolution. For higher temperatures, more evaporation takes place, leading to slower growth rates.

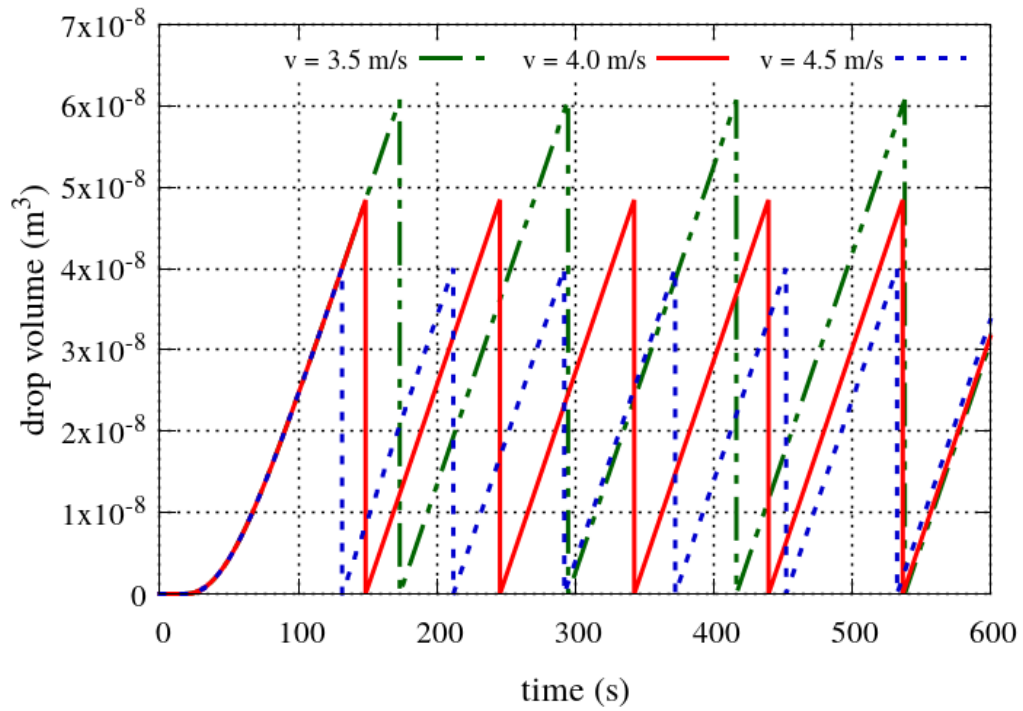


Figure 8.15: Variation of free-flow velocities

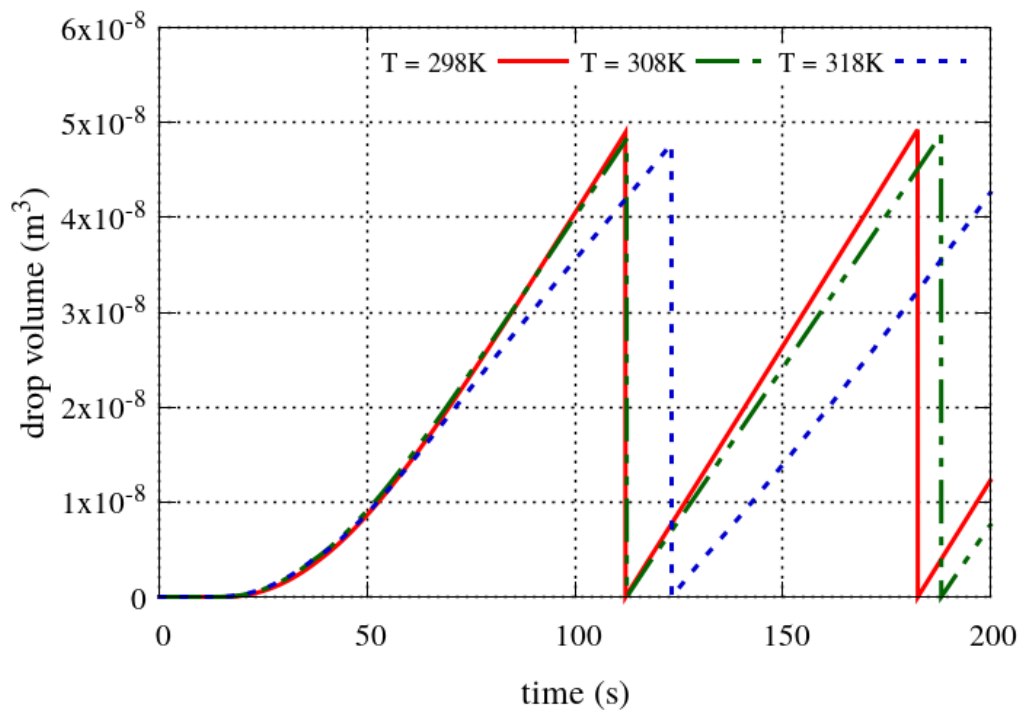


Figure 8.16: Variation of temperatures

8.2.6 Discussion

The isothermal reference case demonstrates that drop formation, growth and detachment can be modeled with the presented multi-scale coupling approach. Several drop cycles can be modeled with a stable implementation. As intended by the conceptual model, the liquid saturation as a primary variable represents the drop volumes in the interface domain. The influence of evaporation from the drop surfaces becomes apparent when taking nonisothermal conditions into account. The slower drop growth rates can be directly linked to the evaporation rates. If different pore sizes are considered, the formation condition is fulfilled subsequently, depending on the respective pore radius. However, since the liquid pressure does not rise infinitely, the formation condition is not fulfilled for every pore radius. This behavior matches the theoretical considerations and expectations. Variations of the inflow rate, free-flow velocity and overall temperature show that the drops react to such altered conditions in a reasonable way. Their qualitative behavior can be explained for all tested parameters. For a quantitative analysis, test cases with data from experiments or applications should be set up in the future.

8.3 Merging

In the previous section, the number of pores was set manually to avoid that the drops touch before they detach. In this section, the number of surface pores is set by the porosity of the porous medium. This results in a larger number of pores, with smaller distances in between. Therefore, we expect the drops to merge before they are detached.

To test this claim, a merging criterion needs to be defined. In the following, we assume all pores to be homogeneously distributed over the interface area A_Γ , as shown in Figure 8.5. Each drop covers an area of $A_{\text{drop}} = \pi r_{\text{drop}}^2$. However, the drops merge as soon as they touch, which would be the case if the square areas $A_{\text{drop}}^{\text{square}} = (2r_{\text{drop}})^2$ would cover the whole interface area A_Γ , as illustrated in Figure 8.17.

Therefore, we first compute the sum of the square areas $A_{\text{drop}}^{\text{square}}$ and compare them to A_Γ to determine the latest time when the drops touch and merge. Then, as a second criterion, the sum of the drop areas $\sum A_{\text{drop}}$ is compared to the interface area A_Γ to obtain an approximation of the earliest time of touching and merging.

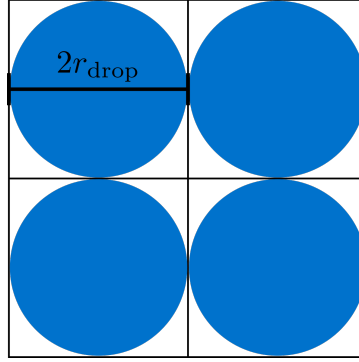
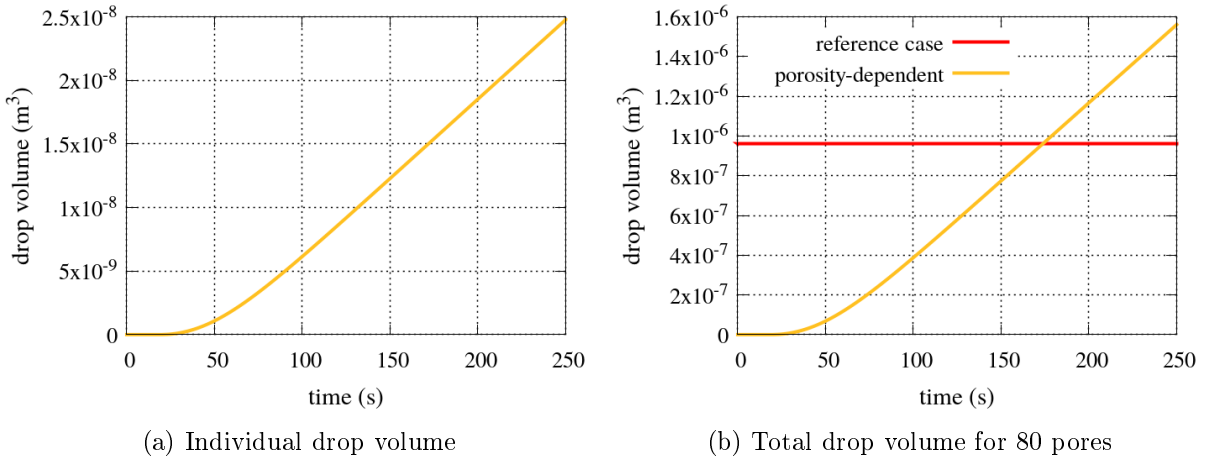


Figure 8.17: Touching of homogeneously distributed drops

Figure 8.18: Drop volume evolution for $n_{\text{pores}} = n_{\text{pores}}(\Phi)$

8.3.1 Results

The number of pores is computed as $n_{\text{pores}} = \frac{A_{\Gamma} \Phi f_{\bar{r}_{\text{pore}}}}{A_{\text{pore}}} = \frac{0.0005 \cdot 0.5 \cdot 1.0}{\pi \cdot 10^{-6}} \approx 80$. As mentioned before, the drops are assumed to be distributed homogeneously, with 4 drops in x-direction and 20 drops in z-direction. The individual drop volume over time is presented in Figure 8.18a. Since the liquid flux from the porous medium is now distributed between 80 pores, the drops grow slower compared to the reference case with 20 pores. However, the total drop volume exceeds the total drop volume at the point of detachment in the reference case $V_{\text{drop}}^{\text{detach, total}} = 20 \cdot 4.8 \cdot 10^{-8} \text{m}^3 = 9.6 \cdot 10^{-7} \text{m}^3$ already at $t = 174\text{s}$, see Figure 8.18b.

Figure 8.19a compares the areas $A_{\text{drop}}^{\text{square}}$ and A_{Γ} and reveals that $A_{\text{drop}}^{\text{square}} = A_{\Gamma}$ at $t = 109.9\text{s}$. Evaluating the second criterion yields $\sum A_{\text{drop}} = A_{\Gamma}$ at $t = 137.0\text{s}$. Therefore, the point of merging can be estimated as $109.9\text{s} \leq t_{\text{merge}} \leq 137.0\text{s}$. The liquid saturation

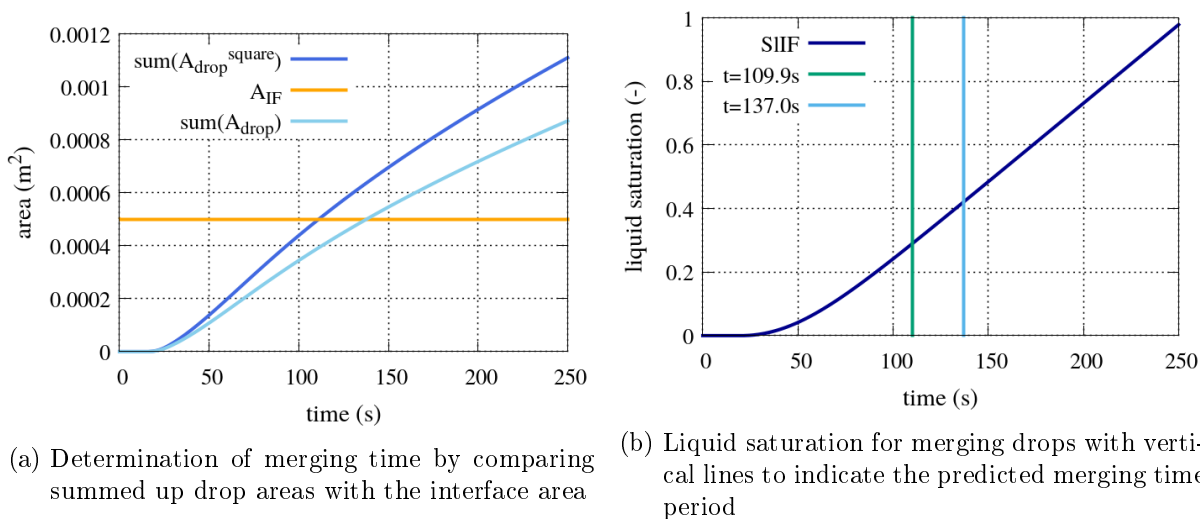


Figure 8.19: Drop-covered area and liquid saturation for $n_{\text{pores}} = n_{\text{pores}}(\Phi)$

of the interface domain is shown in Figure 8.19b and is $S_i^{\text{if}} = 0.29$ when the drops merge according to the first criterion, and $S_i^{\text{if}} = 0.42$ according to the second one.

8.3.2 Discussion

The results obtained under the assumption that the porosity determines the number of surface pores match the expectations: The drops form and grow as in the reference case, but touch before they can be detached. As soon as drops touch and merge, a new concept becomes necessary since they cannot be described as spherical shapes anymore. Therefore, lateral fluxes along the interface need to be taken into account to model film flow, as suggested in Section 6.3.

However, the criteria to determine the time when the drops merge cannot take heterogeneous distributions of the pores into account. To do so, the drops would have to be resolved individually, which is out of the scope of our model.

8.4 Film flow

The results of the previous section show that film flow should be taken into account when modeling realistic porous media. In the following, the concept for lateral fluxes along the interface is applied under isothermal as well as nonisothermal conditions. Compared to

the reference cases, the free-flow velocity \mathbf{v}_g^{ff} is set to zero to prevent the drop detachment under otherwise equal conditions. Instead, a small pressure gradient with a difference of $\Delta p_g = 0.006\text{Pa}$ is set between the left and the right boundary of the free-flow domain. For both the isothermal as well as the nonisothermal test case, a no-flow as well as an outflow boundary condition are tested on the right boundary of the interface domain.

8.4.1 Isothermal test case

For the film flow scenarios, we compare the liquid saturation in the interface domain for the two different boundary conditions. Figure 8.20a shows the saturation in each of the six interface grid cells over time for a no-flow boundary condition. The dashed line indicates the critical saturation $S_l^{\text{merge}} = 0.5$. This value is only a guess due to the lack of experimental data or detailed knowledge with respect to the distribution of the pores. Due to the small pressure gradient from left to right, a lateral flux establishes as soon as the critical saturation is exceeded in at least two neighboring elements. The saturation in the left grid cell still increases due to the continuous flux from the porous medium, but grows with a significantly smaller rate due to the outgoing fluxes across its right boundary. In the four central elements, the growth rate stays approximately constant, since the lateral fluxes across the left and right boundaries balance out. The growth itself is still caused by the liquid flux from the porous medium. The saturation in element 5 (right grid cell) shows a faster increase in the saturation as soon as lateral fluxes are possible. Due to the no-flow boundary condition on the right, the water accumulates in this cell.

To avoid an accumulation, an outflow boundary condition is set in a second simulation run. The results in Figure 8.20b show varying growth rates throughout the interface domain. However, the water can leave the right grid cell across the right boundary, which allows a continuous flux from left to right. Due to the outflow, the inflow from the porous medium and the lateral fluxes reach an equilibrium, leading to a constant saturation after $t \approx 200\text{s}$ in every grid cell.

8.4.2 Nonisothermal test case

The same boundary conditions are tested for a nonisothermal setting. Figures 8.21a and 8.21b present the respective changes in the saturation. Again, a lateral flux from left to

right establishes and influences the drop growth rates. Compared to the saturation in the isothermal case, lower saturations and therefore smaller film heights can be observed due to evaporation.

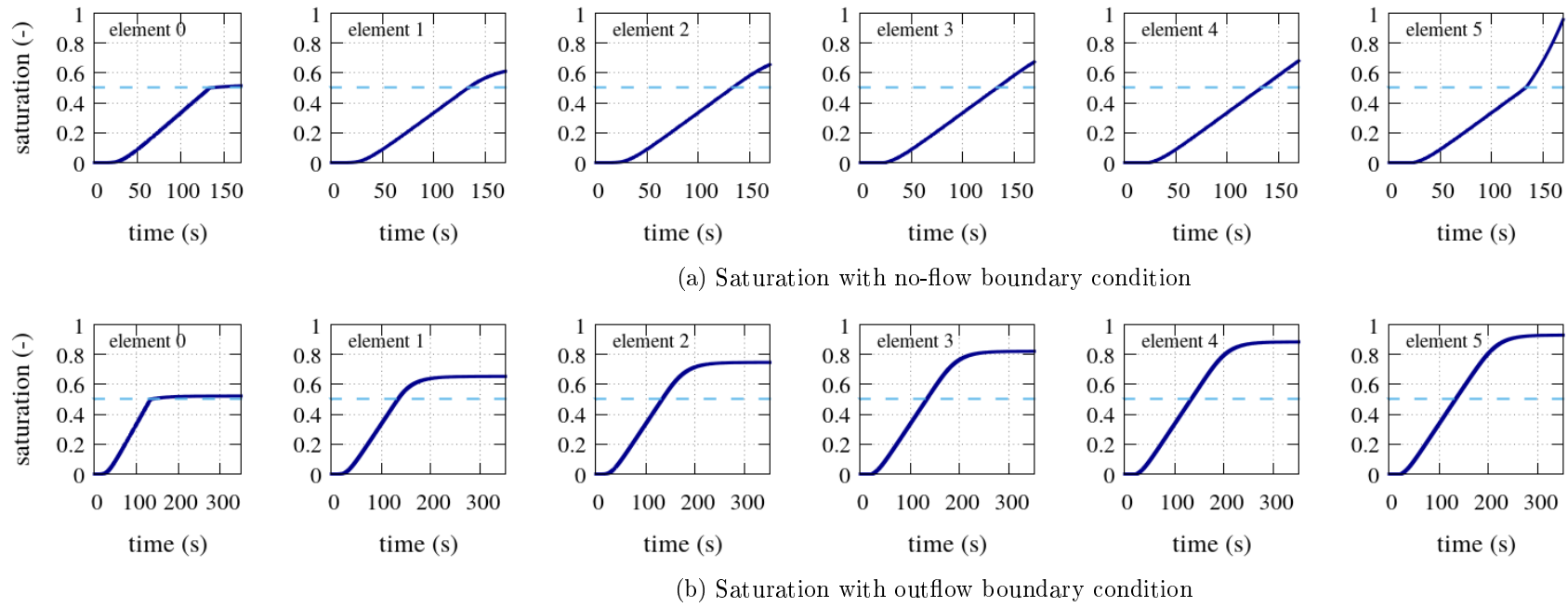
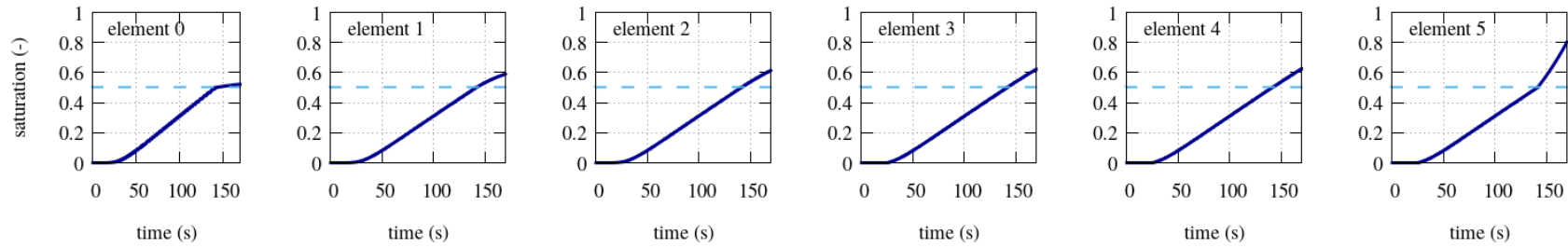
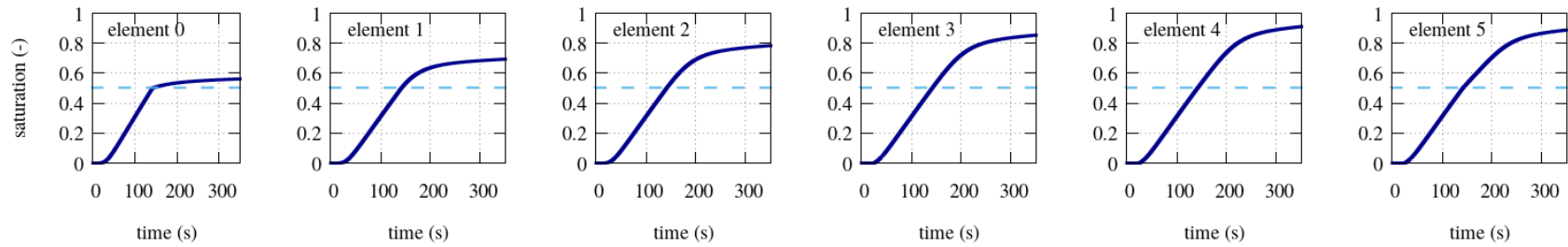


Figure 8.20: Saturation for different boundary conditions under isothermal conditions



(a) Saturation with no-flow boundary condition



(b) Saturation with outflow boundary condition

Figure 8.21: Saturation for different boundary conditions under nonisothermal conditions

8.4.3 Discussion

The concept for lateral fluxes along the interface of a coupled free-flow/porous-medium-flow system yields qualitatively appropriate results. A continuous flux from left to right is established as soon as the drops in two neighboring grid cells touch and merge. In case of a closed border, the water accumulates. For an outflow boundary, the saturation settles at a constant value, which differs for each grid cell. Since the film thickness depends on the discretization, different film heights can be observed in neighboring grid cells. For a more realistic representation of the lateral flux between two grid cells with different film heights, gravity should be taken into account. Under the influence of gravity and a corresponding liquid pressure gradient, a continuous film height along the whole interface is expected.

In addition, the value for the merging criterion should be replaced by a theoretically or empirically derived number.

The numerical model for lateral fluxes turns out to be very sensitive to the flow rates across the grid cell boundaries. Due to the relatively high permeability of $K = \frac{(h^{if})^2}{12} \approx 10^{-6} \text{m}^2$, only small horizontal pressure gradients which lead to lateral fluxes of the same order of magnitude as the flux from the porous medium can be handled by the numerical solver.

In summary, this first concept for lateral fluxes does not yet represent real flow processes, but could serve as a base for further developments and modifications to obtain a realistic film flow model.

8.5 Comparison with simple coupling concept

After looking at the interface domain and the drops themselves, we now investigate the drops' influence on the free flow and the flow in the porous medium in a nonisothermal setting.

First, we compare the results obtained with the simple coupling concept (Section 4.2) with three different set-ups of the drop coupling concept in Section 8.5.1. Then, a more detailed comparison between the simple coupling concept and the reference case with

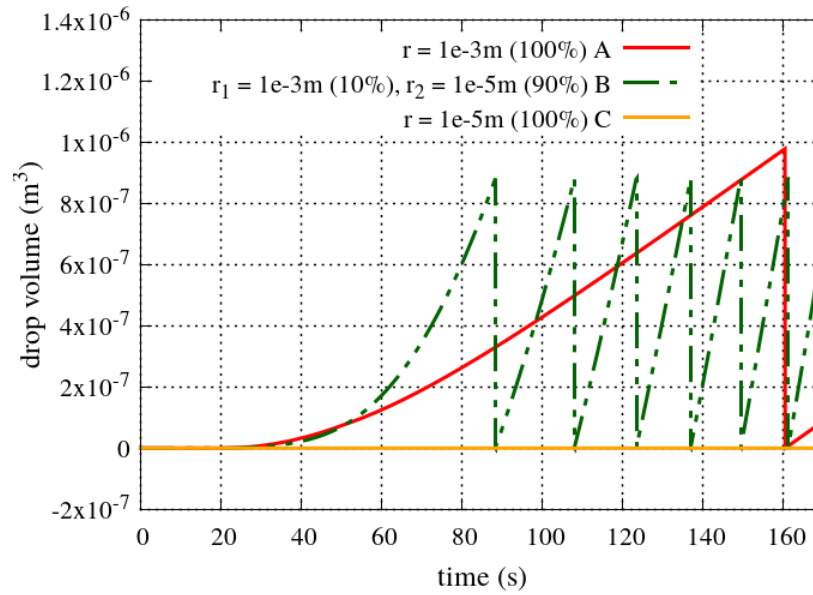


Figure 8.22: Drop volumes for different pore radii

drops (Section 8.2) is conducted in Section 8.5.2. All results are discussed and evaluated in Section 8.5.3.

8.5.1 Different numbers of drops

Three different combinations of pore radii are chosen for the first comparison:

- A: drops on all pores (100% $r_{\text{pore}} = 10^{-3}\text{m}$, all pores liquid-filled)
- B: drops on some pores (10% $r_{\text{pore}} = 10^{-3}\text{m}$, 90% $r_{\text{pore}} = 10^{-5}\text{m}$, some pores liquid-filled, some pores gas-filled),
- C: no drops (100% $r_{\text{pore}} = 10^{-5}\text{m}$, all pores gas-filled).

The resulting drop volume evolutions are shown in Figure 8.22. For the pores with $r_{\text{pore}} = 10^{-5}\text{m}$, the drop formation condition cannot be fulfilled due to the high entry pressure. Since the inflow at the lower boundary of the porous medium is the same for all cases, the whole flux feeds the drops on only 10% of the pores in case B, leading to faster growth and detachment.

Figure 8.23 shows the gas pressure and velocity in the whole model domain for the simple coupling concept as well as cases A, B and C for the drop coupling concept. Note that

the scaling factors applied to the gas velocities differ by five orders of magnitude, i.e. $\chi_{\mathbf{v}_g^{\text{ff}}} = 10^5 \cdot \chi_{\mathbf{v}_g^{\text{pm}}}$, to ensure the visibility of the velocity field in both domains. As expected, Figures 8.23a and 8.23b show identical results. If 10% of the pores are liquid-filled, gas can still flow across the interface domain. As a result, the gas pressure in the whole domain stays constant, as shown in Figure 8.23c. However, the gas velocity is reduced compared to the no-drops case. Figure 8.23d corresponds to the reference case, where all surface pores are occupied by liquid and drops have formed. Due to the blockage, the free-flow gas phase cannot enter the porous medium. Additionally, the gas pressure in the porous medium rises due to the rising amount of liquid injected at the bottom boundary. The gas velocity is of one order of magnitude less than in the other cases and therefore not visible. However, it is pointing downwards, in opposite direction to the rising liquid from the bottom boundary.

8.5.2 Reference case

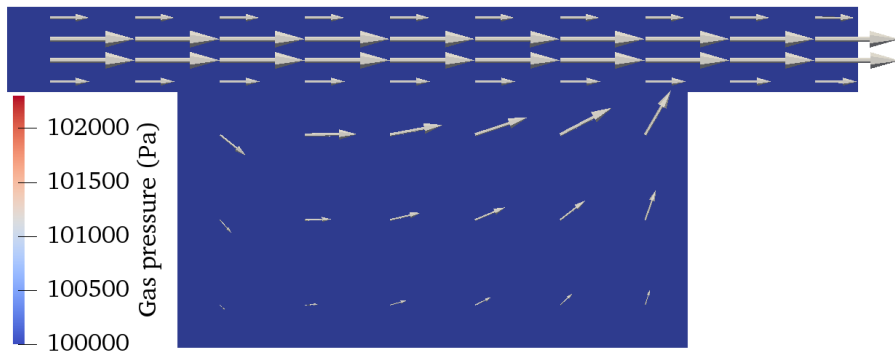
For a more detailed analysis, the nonisothermal reference case is compared with the simple coupling concept. The results in Section 8.2.3 have shown that the drops detach at approximately $t = 159\text{s}$. Therefore, the times $t_1 = 158\text{s}$ and $t_2 = 163\text{s}$ are chosen for the following comparison such that the effects before and after the detachment can be captured. Below, the free-flow and porous-medium-flow regions are analyzed separately.

Free flow

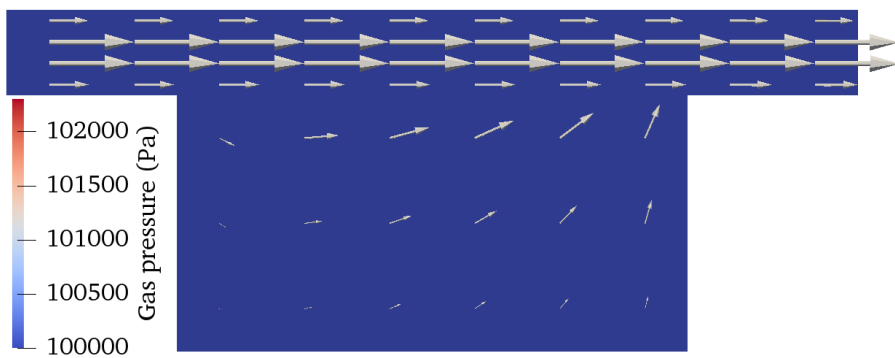
The comparison for the free-flow region is restricted to the area which is directly coupled to the interface and porous medium respectively ($0.02\text{m} \leq x^{\text{ff}} \leq 0.08\text{m}$). All values are taken at a height of $y^{\text{ff}} = 0.001\text{m}$.

Figure 8.24 shows the distribution of the water mass fraction in gas X_g^w for t_1 and t_2 . In nonisothermal settings, the water mass fraction in gas indicates the evaporation rate. Due to the presence of liquid at the interface with the drop coupling concept, higher evaporation rates than with the simple coupling concept can be observed. In addition, less evaporation takes place at t_2 , since the drops are just starting to grow again and have a smaller surface than at t_1 .

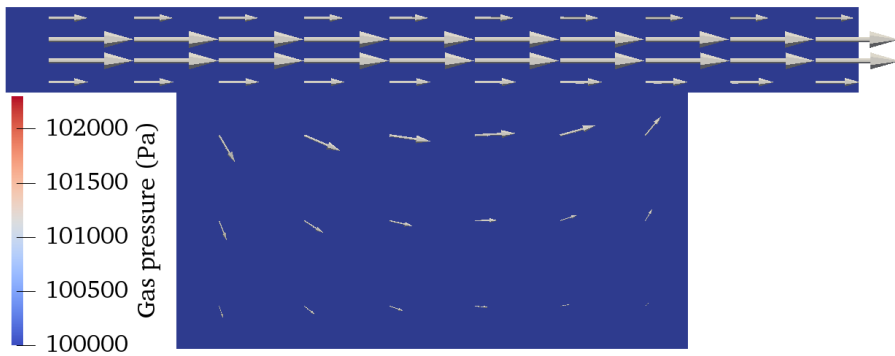
The resulting temperature T is illustrated in Figure 8.25. Higher evaporation rates can be observed when drops are taken into account, leading to a temperature drop along



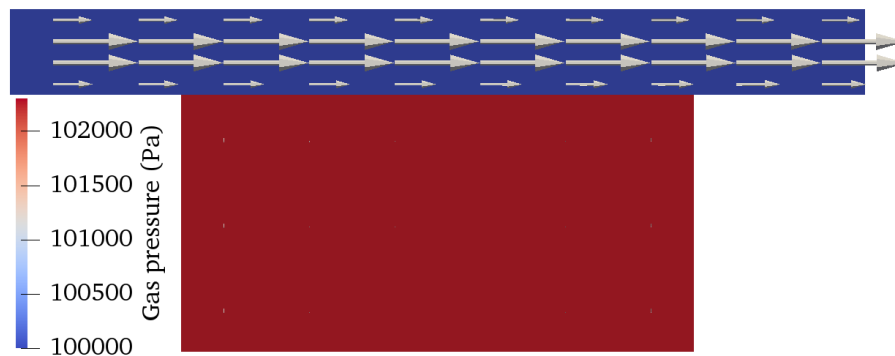
(a) Gas pressure and velocity without drops (simple concept)



(b) Gas pressure and velocity without drops (drop concept)



(c) Gas pressure and velocity with 10% drops



(d) Gas pressure and velocity with 100% drops

Figure 8.23: Gas pressure and velocity in the whole model domain at $t_1 = 158s$

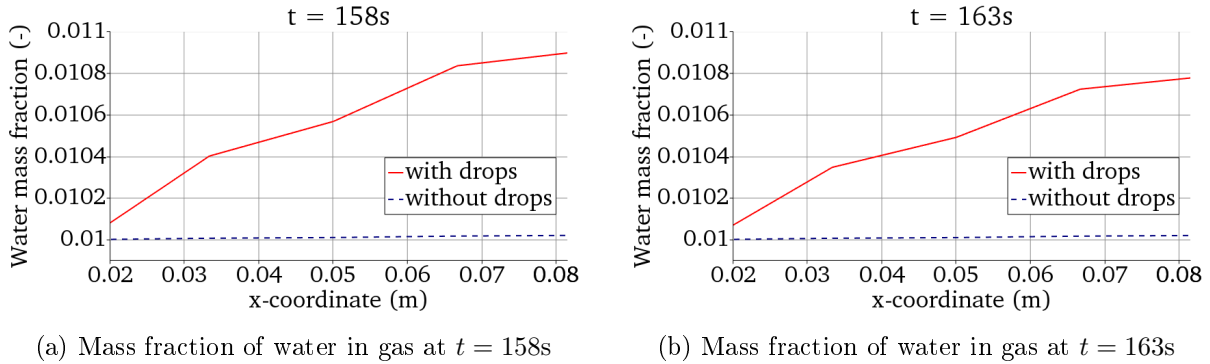


Figure 8.24: Free flow: Mass fraction of water in gas over x-axis

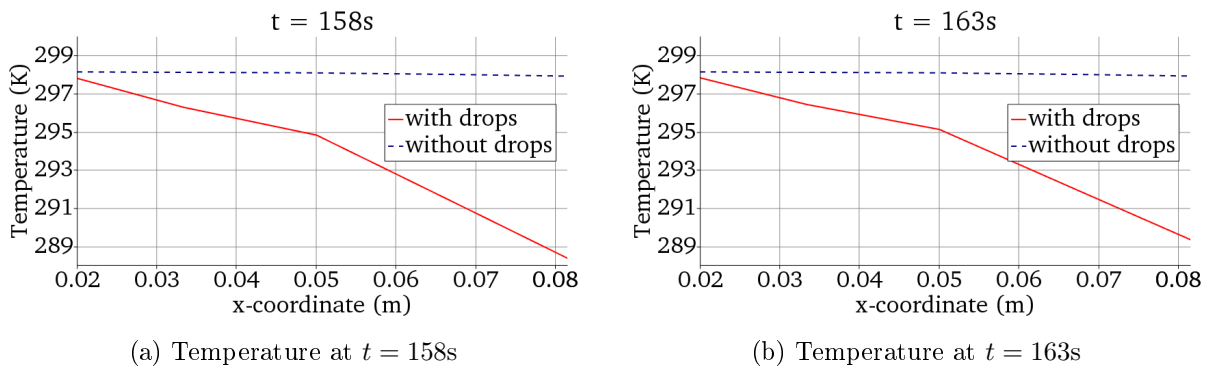


Figure 8.25: Free flow: Temperature over x-axis

the interface. Again, the temperature drop is larger at t_1 , when the drops have almost reached their maximum volume and surface area.

Porous medium

The results for the porous medium are compared along the central y-axis at $x^{\text{pm}} = 0.03\text{m}$ because of the vertical main flow direction. We mostly focus on the upper part of the porous medium in the following comparison.

Due to the constant inflow across the lower boundary, the liquid saturation rises from $S_l^{\text{init}} = 0.0$ to $S_l^{\text{pm}} = 0.15$ and $S_l^{\text{pm}} = 0.31$ respectively, as shown in Figure 8.26a. While the saturation at the upper boundary ($y^{\text{pm}} = 0.03\text{m}$) is almost constant when drops are taken into account, it increases continuously when the liquid is not allowed to leave the porous medium, see Figure 8.26b.

The saturation directly influences the capillary pressure p_c . Consequently, Figure 8.27b shows a slightly higher capillary pressure for the simple coupling concept than Figure

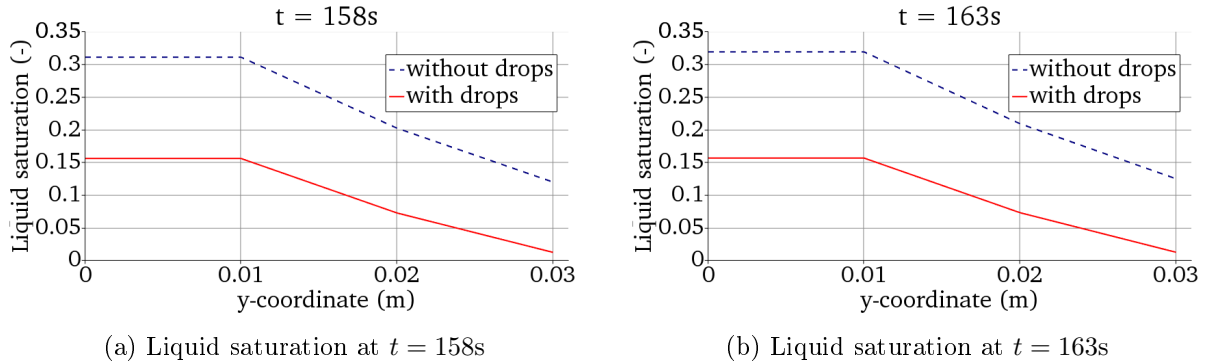


Figure 8.26: Porous medium: Liquid saturation over y-axis

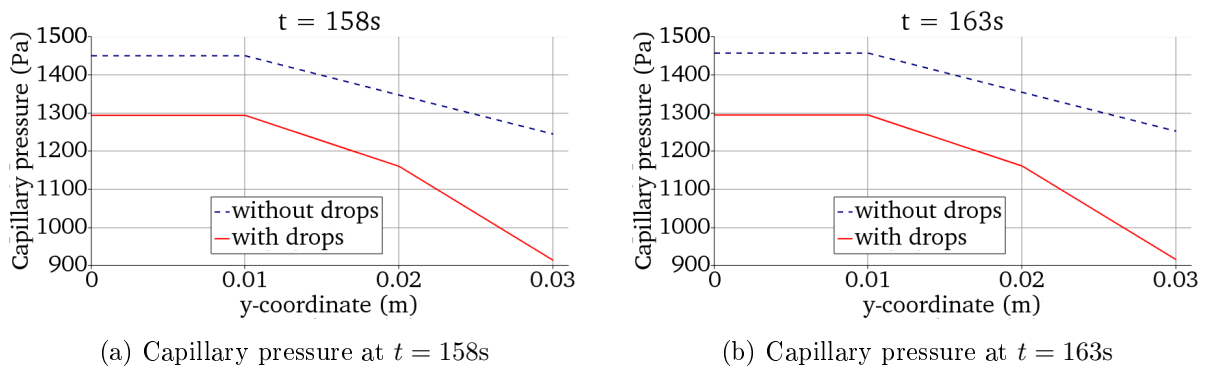


Figure 8.27: Porous medium: Capillary pressure over y-axis

8.27a.

The liquid pressure depends on the gas pressure as well as the capillary pressure via $p_l = p_c + p_g$ in a hydrophobic porous medium. As already shown in Figure 8.23d, the gas pressure in the porous medium is higher by approximately $\Delta p_g = 2 \cdot 10^3 \text{Pa}$ if all surface pores are occupied by liquid. Since the difference in the capillary pressures is only $-400 \text{Pa} \leq \Delta p_c \leq -200 \text{Pa}$, the resulting liquid pressure when drops are taken into account is higher than when they are neglected. However, it slightly decreases after the detachment, while the liquid pressure with the simple coupling concept rises continuously.

Comparing the temperatures in the porous medium as done in Figures 8.29a and 8.29b, yields a similar result as the one obtained for the free-flow region: Due to the presence of drops, a higher evaporation rate establishes at the interface when drops are taken into account, yielding lower temperatures when drops are taken into account.

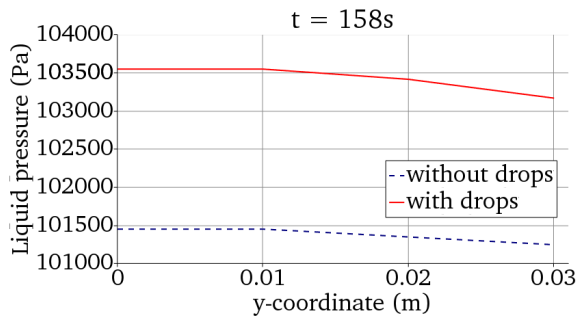
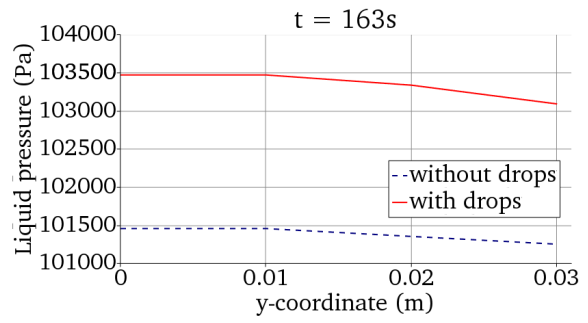
(a) Liquid pressure at $t = 158\text{s}$ (b) Liquid pressure at $t = 163\text{s}$

Figure 8.28: Porous medium: Liquid pressure over y-axis

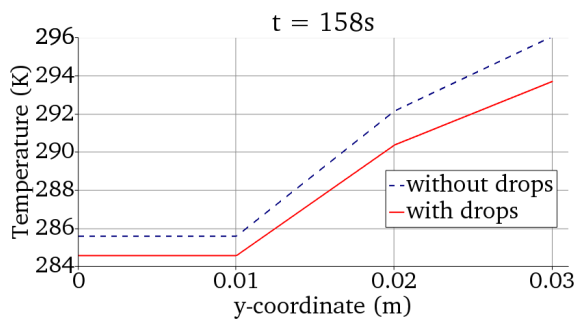
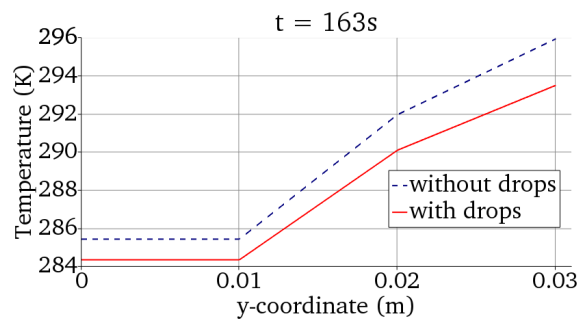
(a) Temperature at $t = 158\text{s}$ (b) Temperature at $t = 163\text{s}$

Figure 8.29: Porous medium: Temperature over y-axis

8.5.3 Discussion

In general, the results obtained with the different coupling concepts meet the expectations with respect to the physical behavior of pressure, velocity, temperature, mass fraction and saturation. If not all pores are occupied by liquid, an exchange of gas between free flow and porous medium can take place. In relatively homogeneous porous media where all pores have approximately the same radius, the whole interface would be blocked for gaseous fluxes if drops form. Therefore, the drop formation criterion should be evaluated and interfacial drops should be taken into account. In very heterogeneous porous media with pore radii of different orders of magnitude, interfacial drops might be negligible. However, for a detailed description of the interface processes between a single-phase gaseous free-flow and a two-phase flow in a hydrophobic porous medium, the presented coupling concept with drops should be applied.

8.6 Formation, growth and detachment (Phase-field model)

In the following, numerical results obtained with the coupling concept with drops in a phase-field model as introduced in Chapter 7 are shown and discussed. First, the set-up of the two respective model domains is outlined. Then, the results on the pore-scale as well as on the macro-scale are presented separately. As mentioned before, the results are also published by Ackermann et al. [2021c].

8.6.1 Set-up

The computational domains are sketched in Figure 8.30.

Pore-scale: An unstructured grid is used to compute the drops with the phase-field model. The pore has a radius of $r_{\text{pore}} = 2.5 \cdot 10^{-3}\text{m}$. Since deformation is neglected, the drops are symmetrical to the y-axis. Therefore, the computational domain for the pore-scale model contains only a vertical half of the pore and drop to save computation time.

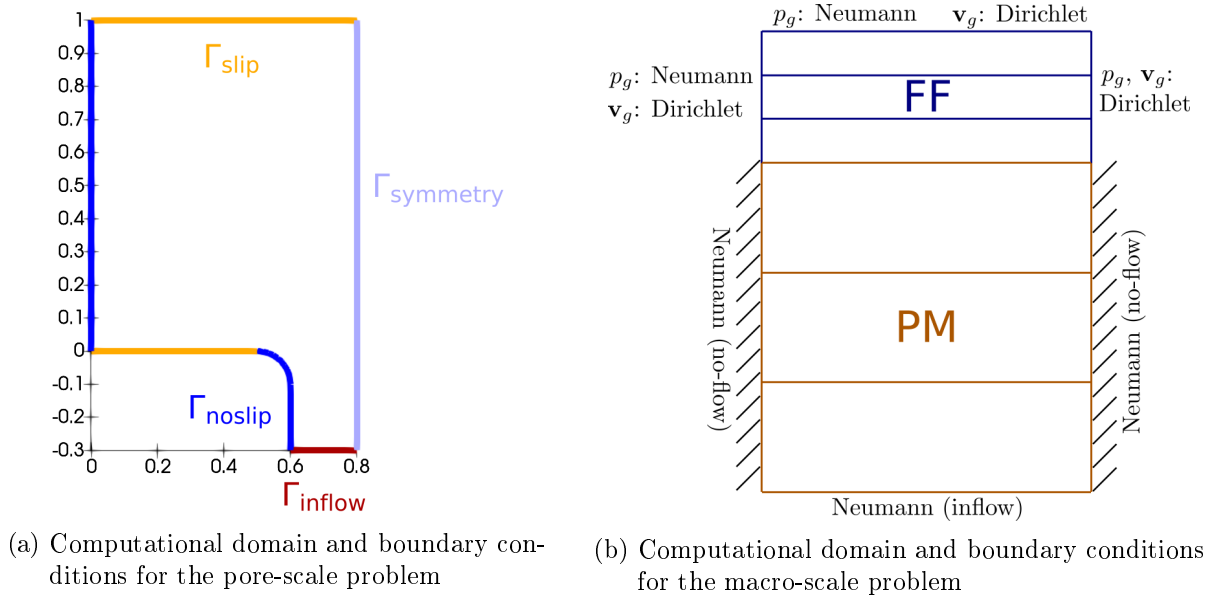


Figure 8.30: Computational domains and boundary conditions

Macro-scale: For the flow in the porous medium, a vertical one-dimensional flow is assumed. Therefore, only one grid cell is resolved in x-direction and three grid cells are set in y-direction. The inflow rate at the bottom of the porous medium is $q_{\text{bottom}} = 0.025 \text{ kg/s}$. In each grid cell, 25 pores (50%) are assumed to fill with liquid, which still allows the exchange of gas across the interface between free flow and porous medium. For the free flow, the maximum velocity of the parabolic velocity profile at the left boundary is set to $v_{\text{max}} = 5 \text{ m/s}$.

8.6.2 Phase-field model

Figure 8.31 shows the phase-field model at different times. At $t = 0 \text{ s}$, the phase-field model is initialized with a liquid-filled pore. The small disturbances at the phase interface are caused by the grid structure. Within the next seconds, the drop grows due to the liquid mass flux from the porous medium. At $t = 0.25 \text{ s}$ it reaches its maximum volume. The detachment condition is fulfilled and a new drop starts to form in the next time step.

The drop volume evolution is shown in Figure 8.32. Several cycles of drop formation, growth and detachment can be captured. The initial drop volume of approximately 0.01 m^3 does not actually represent a growing drop, but is caused by the initial conditions.

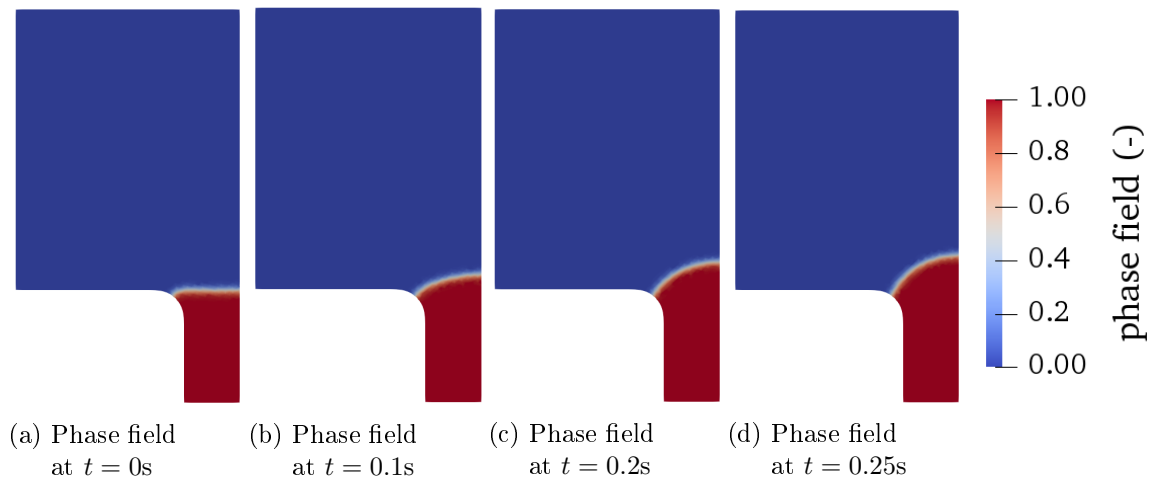


Figure 8.31: Drop formation and growth in the phase-field model

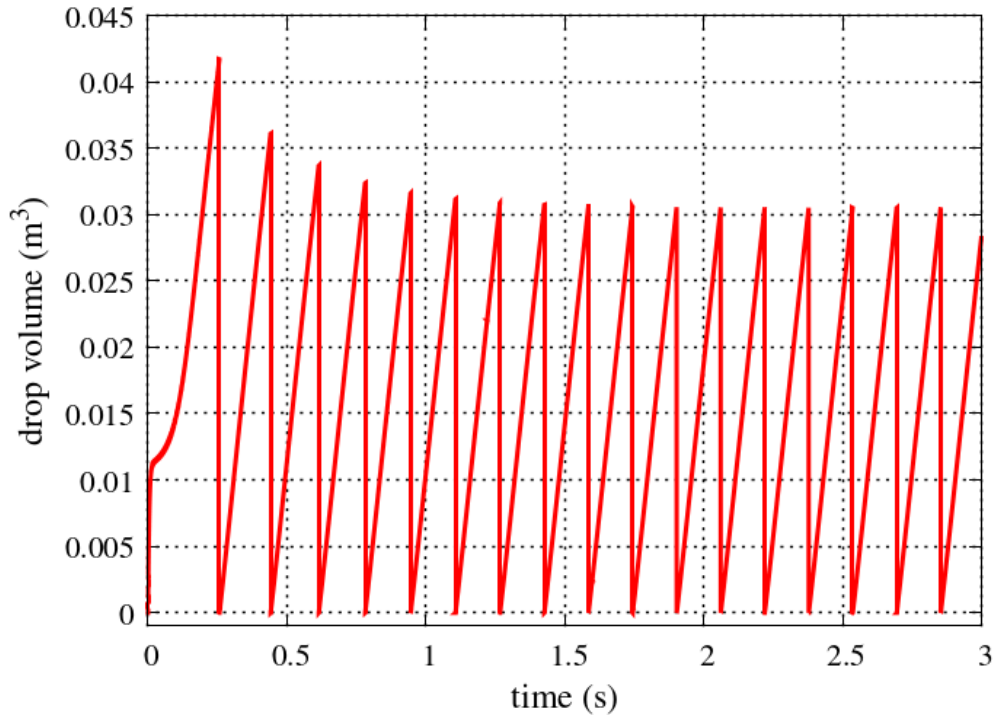


Figure 8.32: Drop volume evolution computed by the phase-field model

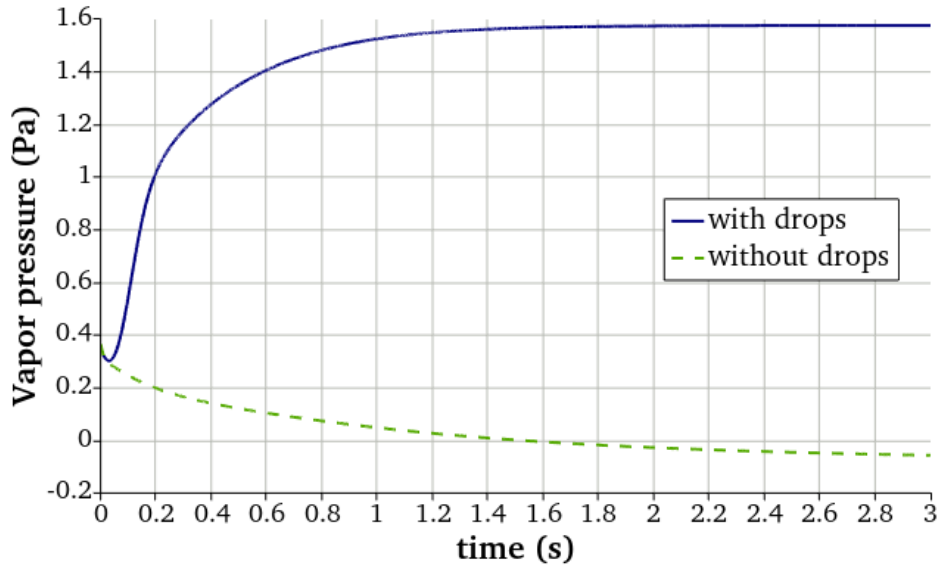


Figure 8.33: Vapor pressure in the free flow

8.6.3 Influence on macro-scale flow

To investigate the influence of the pore-scale on the macro-scale behavior, we compare the reference case (“with drops”) with the case of no inflow into the porous medium, i. e. $q_{\text{bottom}} = 0\text{kg/s}$. Without liquid mass inflow, no drops form (“without drops”). Figure 8.33 shows the free-flow vapor pressure in the lowest free-flow grid cell, which increases quickly and then stays constant at $p_g^{\text{ff}} = 1.57\text{Pa}$.

The influence on the top layer of the porous medium is shown in Figures 8.34 and 8.35. The liquid pressure rises until $t \approx 1\text{s}$, similar to the vapor pressure in the free flow. Afterwards, an equilibrium is reached and the liquid pressure stays constant. Due to the mass inflow at the lower boundary, the liquid pressure rises high enough to form drops. The liquid saturation also reaches an equilibrium, but is slightly higher than in the case without drops. However, it is quite low in both cases.

8.6.4 Discussion

The results obtained with the first version of a sequential coupling concept which combines two models on different scales are promising in a qualitative manner. Several cycles of drop formation, growth and detachment can be observed. The pressure in both

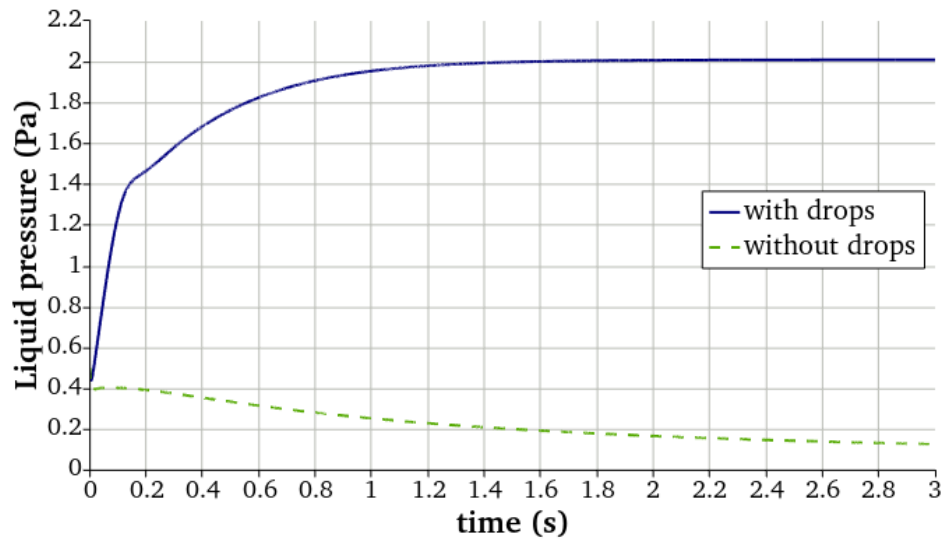


Figure 8.34: Liquid pressure in the porous medium

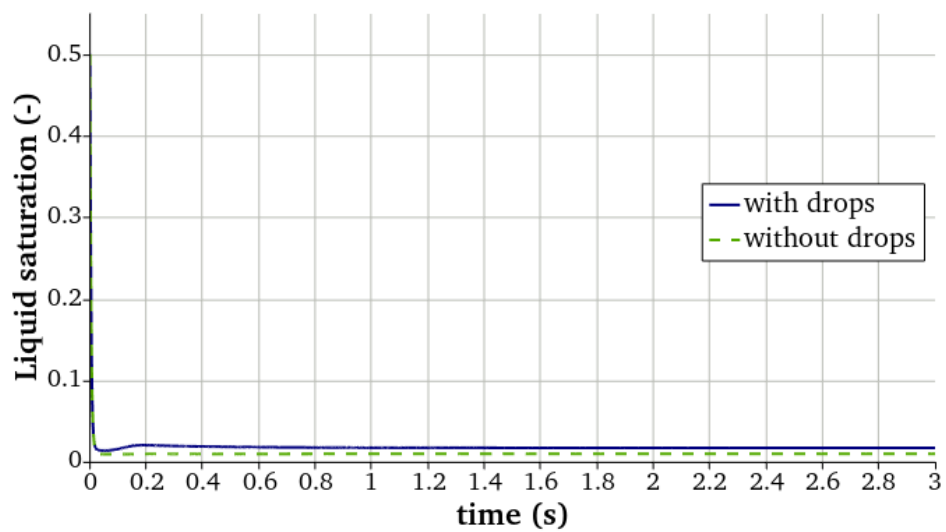


Figure 8.35: Liquid saturation in the porous medium

macro-scale domains rises due to the liquid mass inflow and the drop growth. The liquid saturation is slightly higher than in the case without mass inflow, where no drops form. The drop detachments do not influence the macro-scale variables. The qualitative analysis of the results shows that the presented coupling concept is able to transfer the information between the two scales in a reasonable manner.

However, it has to be kept in mind that an artificial fluid system with a density ratio of $\rho_l/\rho_g = 1$ is used here. This ratio cannot be achieved with any real fluids. Therefore, the multi-scale coupling concept with drops in a phase-field model domain is not suitable for the application to real-life scenarios.

In addition, the interaction between free flow and drops is neglected in this simplified version of the coupling concept. Implementing these mutual influences would allow a more detailed analysis of the interplay between the pore-scale and the macro-scale.

9 Summary

The objective of this work is to develop coupling concepts for free-flow/porous-medium-flow systems in which drops form at the interface between the two flow compartments. We focus on systems consisting of a single-phase gaseous free flow and a two-phase flow in a hydrophobic porous medium and investigate the influence of drops on the exchange of mass, momentum and energy across the common interface. The simple coupling concept developed by Mosthaf et al. [2011] assumes the direct evaporation of the liquid phase at the interface. To obtain a more detailed representation of the interface processes and determine the influence of drops, we develop two multi-scale coupling concepts. Based on the approach presented by Baber et al. [2016], we incorporate the droplet-related processes and their influence on the macro-scale flow processes into the coupling concept.

With this work, we aim at obtaining a better understanding of the influence of drops on coupled free-flow/porous-medium-flow systems as well as a simulation tool to predict the drop behavior in such systems. As a first step, conceptual models for the description of drop dynamics are derived and integrated into the existing coupling concept. Then, the respective numerical models are implemented to test the theoretical considerations with different scenarios.

In Chapters 2 and 3, the physical processes and conceptual models to describe free flow and flow in porous media are presented. Chapter 4 sums up the simple coupling concept, where the interface is devoid of thermodynamic properties and drops are neglected. Then, an overview of drop dynamics is given in Chapter 5 to determine which processes might actually influence the exchange of mass, momentum and energy between the two flow compartments of the coupled system. Based on these considerations, the following two multi-scale coupling concepts are developed:

Coupling concept with lower-dimensional interface domain

For the first coupling concept (Chapter 6), an additional interface domain is embedded in between the free-flow and porous-medium compartments. Within this interface domain, drop formation, growth and detachment are determined based on the conditions in the free flow and the porous medium and the resulting liquid and evaporative fluxes. Since the drop volumes are considered, the interface can now store mass and energy. The drops' influence on the mass and heat fluxes between the two flow compartments is taken into account by formulating appropriate coupling conditions between the respective subdomains. Instead of resolving the individual drops, we average the pore sizes and evaluate the droplet-related processes for a few pore radii only. Since the interface domain is assumed to be approximately the height of the drops, it is reduced by one dimension compared to the other two subdomains. In addition to growth and detachment, merging of drops and film flow along the interface are taken into account.

For the numerical model, the existing implementation of the simple coupling concept is extended to a three-domain concept and adapted accordingly to account for the drops. The numerical implementation is tested with the help of experimental data for the formation and growth of a single drop. Then, we set up several test cases where multiple drops are considered and examine the results with respect to various aspects. The influence on the macro-scale flow processes is determined by comparing the respective results with the results obtained with the simple coupling concept.

Coupling concept with phase-field model domain

For the second coupling concept (Chapter 7), a phase-field model is applied to represent the drops on the pore-scale. The free flow and flow in a porous medium are modeled on the macro-scale analogously to the simple coupling concept. The flow processes on the pore- and the macro-scale are computed sequentially. The exchange between the two scales is achieved by setting appropriate boundary conditions based on data computed by the respective other model. The numerical implementation is tested with a simple scenario. Due to restrictions of the phase-field model implementation, only an artificial fluid can be modeled. Therefore, we limit our investigations to a qualitative analysis of the coupling concept.

9.1 Conclusions

Coupling concept with lower-dimensional interface domain

The comparison with experimental data for the formation and growth of a single drop shows a high correspondence for the drop volume evolution. Therefore, we assume that these processes can be predicted accurately enough to obtain an overview of the drops' influence on more complex systems, where multiple drops exist simultaneously. The results obtained with the two test cases for drop formation, growth and detachment seem to be appropriate both quantitatively and qualitatively. However, no experimental data is available currently to validate this presumption. Similar conclusions can be drawn for merging drops and film flow: The results obtained with the extended model which considers lateral fluxes along the interface seem reasonable based on the underlying assumptions. However, neglecting gravity and using a coarse discretization leads to jumps in the film height. Therefore, lateral mass fluxes cannot be predicted in a realistic way with the current model concept.

Finally, the comparison between the coupling concepts with and without drops shows significant differences in case all surface pores are filled with liquid. The blockage for gas exchange between free flow and porous medium changes the pressure distribution and velocity field, especially in the porous medium. Furthermore, even partly liquid-filled surface pores already have an influence on the exchange between the two flow compartments. Especially in porous media with almost homogeneous pore sizes, the formation of drops should be considered in the coupling concept: In such cases, all surface pores would simultaneously fill with liquid, as soon as the threshold pressure is reached. However, for porous media with very heterogeneous pore sizes which range over several orders of magnitude, drop formation might be negligible.

Coupling concept with phase-field model domain

With the phase-field model coupling concept, a reasonable temporal evolution of the drop volumes can be observed. Additionally, the reaction of the macro-scale flow processes on detached drops seems appropriate. However, due to the restriction to an artificial fluid, the concept cannot be applied to predict realistic cases yet.

9.2 Outlook

Coupling concept with lower-dimensional interface domain

For a more realistic model, the influence of drops on the free-flow velocity field should be taken into account. First investigations with droplet-shaped solid walls were conducted at the Department of Hydromechanics and Modelling of Hydrosystems (University of Stuttgart) with the help of a refined staggered grid discretization. As soon as the refinement can be done adaptively depending on the current solution, this new staggered grid implementation would allow to investigate the influence of the growing drops dynamically.

The conceptual model for merging drops and film flow could be refined and improved. A more precise merging criterion should be developed. In addition, the theoretical considerations could be compared with experiments to obtain more realistic estimations.

Instead of clustering the drops in only a few pore-size classes, they could be resolved individually by representing the interface domain with a pore-network model. A respective model concept is currently developed at the Department of Hydromechanics and Modelling of Hydrosystems (University of Stuttgart).

Coupling concept with phase-field model domain

Concerning the multi-scale coupling concept with the phase-field model, more information should be exchanged between the flow compartments to obtain a fully coupled system.

However, to obtain realistic results, the phase-field model itself needs to be able to numerically treat density ratios of 1:1000, which is not possible with the current concept and implementation.

Bibliography

- S. Ackermann, C. Bringedal, and R. Helmig. Multi-scale three-domain approach for coupling free flow and flow in porous media including droplet-related interface processes. *Journal of Computational Physics*, 429:109993, 2021a. doi: <https://doi.org/10.1016/j.jcp.2020.109993>.
- S. Ackermann, S. Fest-Santini, M. Veyskarami, and R. Helmig. Experimental validation of a multi-scale coupling concept for drop formation and growth with X-ray images. *submitted to The International Journal of Multiphysics*, 2021b.
- S. Ackermann, L. Ostrowski, R. Helmig, and C. Rohde. A multi-scale approach for drop detachment in a coupled free-flow/porous-medium-flow system. *submitted to International Journal of Heat and Mass Transfer*, 2021c.
- M. Alnæs, J. Blechta, J. Hake, A. Johansson, B. Kehlet, A. Logg, C. Richardson, J. Ring, M. E. Rognes, and G. N. Wells. The FEniCS project version 1.5. *Archive of Numerical Software*, 3(100), 2015.
- D. M. Anderson, G. B. McFadden, and A. A. Wheeler. Diffuse-interface methods in fluid mechanics. *Annual Review of Fluid Mechanics*, 30(1):139–165, 1998. doi: [10.1146/annurev.fluid.30.1.139](https://doi.org/10.1146/annurev.fluid.30.1.139).
- S. R. Annapragada, J. Y. Murthy, and S. V. Garimella. Prediction of droplet dynamics on an incline. *International Journal of Heat and Mass Transfer*, 55:1466–1474, 2012. doi: [10.1016/j.ijheatmasstransfer.2011.10.028](https://doi.org/10.1016/j.ijheatmasstransfer.2011.10.028).
- P. D. Antoniadis and M. V. Papalexandris. Numerical study of unsteady, thermally-stratified shear flows in superposed porous and pure-fluid domains. *International Journal of Heat and Mass Transfer*, 96:643–659, 2016. doi: [10.1016/j.ijheatmasstransfer.2016.01.056](https://doi.org/10.1016/j.ijheatmasstransfer.2016.01.056).

- K. Baber. *Coupling free flow and flow in porous media in biological and technical applications: From a simple to a complex interface description*. PhD thesis, University of Stuttgart, Institute for Modelling Hydraulic and Environmental Systems, 2014.
- K. Baber, B. Flemisch, and R. Helmig. Modeling drop dynamics at the interface between free and porous-medium flow using the mortar method. *International Journal of Heat and Mass Transfer*, 99:660–671, 2016. doi: 10.1016/j.ijheatmasstransfer.2016.04.014.
- M. Baggio and B. Weigand. Numerical simulation of a drop impact on a superhydrophobic surface with a wire. *Physics of Fluids*, 31:112107, 2019. doi: 10.1063/1.5123593.
- F. Basirat, P. Sharma, F. Fagerlund, and A. Niemi. Experimental and modeling investigation of CO₂ flow and transport in a coupled domain of porous media and free flow. *International Journal of Greenhouse Gas Control*, 42:461–470, 2015. doi: 10.1016/j.ijggc.2015.08.024.
- P. Bastian, M. Blatt, A. Dedner, C. Engwer, R. Klöfkorn, M. Ohlberger, and O. Sander. A generic grid interface for parallel and adaptive scientific computing. Part I: Abstract framework. *Computing*, 82:103–119, 2008. doi: 10.1007/s00607-008-0003-x.
- J. Bear. *Dynamics of fluids in porous media*. Courier Corporation, 2013.
- G. S. Beavers and D. D. Joseph. Boundary conditions at a naturally permeable wall. *Journal of Fluid Mechanics*, 30:197–207, 1967. doi: 10.1017/s0022112067001375.
- T. Berning, M. Odgaard, and S. K. Kær. A computational analysis of multiphase flow through PEMFC cathode porous media using the multifluid approach. *Journal of The Electrochemical Society*, 156:B1301–B1311, 2009. doi: 10.1149/1.3206691.
- R. B. Bird, W. E. Stewart, and E. N. Lightfoot. *Transport phenomena* (revised second ed.) John Wiley & sons. *New York*, 2007.
- M. Blatt and P. Bastian. The iterative solver template library. In B. Kagström, E. Elmroth, J. Dongarra, and J. Wasniewski, editors, *Applied Parallel Computing – State of the Art in Scientific Computing*, pages 666–675, Berlin/Heidelberg, 2007. Springer. doi: 10.1007/978-3-540-75755-9_82.
- M. Blatt, A. Burchardt, A. Dedner, C. Engwer, J. Fahlke, B. Flemisch, C. Gersbacher, C. Gräser, F. Gruber, C. Grüninger, D. Kempf, R. Klöfkorn, T. Malkmus, S. Müthing, M. Nolte, M. Piatkowski, and O. Sander. The Distributed and Unified Numerics

-
- Environment, Version 2.4. *Archive of Numerical Software*, 4:13–29, 2016. doi: 10.11588/ans.2016.100.26526.
- T. Blesgen. A generalization of the Navier-Stokes equations to two-phase flows. *Journal of Physics D: Applied Physics*, 32:1119, 1999.
- E. Bonaccorso, R. Pericet-Camera, and H.-J. Butt. *Drops and Bubbles in Contact with Solid Surfaces*, chapter Microdrops evaporating from deformable or soluble polymer surfaces, pages 105–128. CRC Press, 2013. doi: 10.1201/b13247.
- C. Bourges-Monnier and M. E. R. Shanahan. Influence of evaporation on contact angle. *Langmuir*, 11:2820–2829, 1995. doi: 10.1021/la00007a076.
- H. C. Brinkman. A calculation of the viscous force exerted by a flowing fluid on a dense swarm of particles. *Flow, Turbulence and Combustion*, 1:27–34, 1949. doi: 10.1007/bf02120313.
- R. Brooks and T. Corey. Hydraulic properties of porous media. *Hydrology Papers, Colorado State University*, 24:37, 1964.
- H.-J. Butt, D. S. Golovko, and E. Bonaccorso. On the derivation of Young’s equation for sessile drops: Nonequilibrium effects due to evaporation. *Journal of Physical Chemistry*, 111:5277–5283, 2007. doi: 10.1021/jp065348g.
- J. W. Cahn and J. E. Hilliard. Free energy of a nonuniform system. I. Interfacial free energy. *The Journal of Chemical Physics*, 28:258–267, 1958. doi: 10.1063/1.1744102.
- V. P. Carey. Liquid-vapor phase-change phenomena: An introduction to the thermophoresis of vaporisation and condensation processes in heat transfer equipment. *Corp: Washington, DC*, 1992.
- A. B. D. Cassie and S. Baxter. Wettability of porous surfaces. *Transactions of the Faraday society*, 40:546–551, 1944. doi: 10.1039/tf9444000546.
- J. Chen, S. Sun, and X.-P. Wang. A numerical method for a model of two-phase flow in a coupled free flow and porous media system. *Journal of Computational Physics*, 268: 1–16, 2014. doi: 10.1016/j.jcp.2014.02.043.
- K. S. Chen. Modeling water-droplet detachment from GDL/channel interface in PEM fuel cells. In *ASME 2008 6th International Conference on Fuel Cell Science, Engineering*

- and Technology*, pages 797–803. American Society of Mechanical Engineers Digital Collection, 2008.
- K. S. Chen, M. A. Hickner, and D. R. Noble. Simplified models for predicting the onset of liquid water droplet instability at the gas diffusion layer/gas flow channel interface. *International Journal of Energy Research*, 29:1113–1132, 2005.
- P. Chidyagwai and B. Rivière. A two-grid method for coupled free flow with porous media flow. *Advances in Water Resources*, 34:1113–1123, 2011. doi: 10.1016/j.advwatres.2011.04.010.
- S. C. Cho, Y. Wang, and K. S. Chen. Droplet dynamics in a polymer electrolyte fuel cell gas flow channel: Forces, deformation and detachment. I: Theoretical and numerical analyses. *Journal of Power Sources*, 206:119–128, 2012. doi: 10.1016/j.jpowsour.2012.01.057.
- H. Class. *Theorie und numerische Modellierung nichtisothermer Mehrphasenprozesse in NAPL-kontaminierten porösen Medien*. PhD thesis, Universität Stuttgart, Institut für Wasserbau, 2001.
- H. Class, R. Helmig, and P. Bastian. Numerical simulation of non-isothermal multiphase multicomponent processes in porous media.: 1. An efficient solution technique. *Advances in Water Resources*, 25:533 – 550, 2002. doi: [https://doi.org/10.1016/S0309-1708\(02\)00014-3](https://doi.org/10.1016/S0309-1708(02)00014-3).
- R. Clift, J. R. Grace, and M. E. Weber. *Bubbles, drops, and particles*. Academic Press, New York, 1978.
- J. Cooper and R. Dooley. Revised release on the IAPWS industrial formulation 1997 for the thermodynamic properties of water and steam. *The International Association for the Properties of Water and Steam*, 1:48, 2007.
- K. Daucik and R. Dooley. Release on the IAPWS formulation 2011 for the thermal conductivity of ordinary water substance. *The International Association for the Properties of Water and Steam*, 2011.
- T. A. Davis. A column pre-ordering strategy for the unsymmetric-pattern multifrontal method. *ACM Transactions on Mathematical Software (TOMS)*, 30:165–195, 2004. doi: 10.1145/992200.992205.

-
- M. Discacciati and A. Quarteroni. Navier-Stokes/Darcy coupling: Modeling, analysis, and numerical approximation. *Revista Matemática Complutense*, 22:315–426, 2009. doi: 10.5209/rev_rema.2009.v22.n2.16263.
- W. Dreyer, J. Giesselmann, and C. Kraus. A compressible mixture model with phase transition. *Physica D: Nonlinear Phenomena*, 273:1–13, 2014. doi: 10.1016/j.physd.2014.01.006.
- H. Y. Erbil, G. McHale, and M. I. Newton. Drop evaporation on solid surfaces: Constant contact angle mode. *Langmuir*, 18:2636–2641, 2002. doi: 10.1021/la011470p.
- T. Fetzer, C. Grüniger, B. Flemisch, and R. Helmig. On the conditions for coupling free flow and porous-medium flow in a finite volume framework. In Springer-Verlag, editor, *Finite Volumes for Complex Applications 8*, 2017.
- X. Frank and P. Perre. Droplet spreading on a porous surface: A lattice Boltzmann study. *Physics of Fluids*, 24(4):042101, 2012. doi: 10.1063/1.3701996.
- F. Fu, P. Li, K. Wang, and R. Wu. Numerical simulation of sessile droplet spreading and penetration on porous substrates. *Langmuir*, 35:2917–2924, 2019. doi: 10.1021/acs.langmuir.8b03472.
- K. Galvin. A conceptually simple derivation of the Kelvin equation. *Chemical engineering science*, 60:4659–4660, 2005.
- D. Gläser, R. Helmig, B. Flemisch, and H. Class. A discrete fracture model for two-phase flow in fractured porous media. *Advances in Water Resources*, 110:335–348, 2017. doi: 10.1016/j.advwatres.2017.10.031.
- B. Goyeau, D. Lhuillier, D. Gobin, and M. G. Velarde. Momentum transport at a fluid-porous interface. *International Journal of Heat and Mass Transfer*, 46:4071–4081, 2003. doi: 10.1016/s0017-9310(03)00241-2.
- V. Gurau and J. A. Mann. Effect on interfacial phenomena at the gas diffusion layer-channel interface on the water evolution in a PEMFC. *Journal of the Electrochemical Society*, 157:B512–B521, 2010. doi: 10.1149/1.3294708.
- V. Gurau, T. A. Zawodzinski, and J. A. Mann. Two-phase transport in PEM fuel cell cathodes. *Journal of Fuel Cell Science and Technology*, 5:021009, 2008. doi: 10.1115/1.2821597.

- F. H. Harlow and J. E. Welch. Numerical calculation of time-dependent viscous incompressible flow of fluid with free surface. *Physics of Fluids*, 8:2182–2189, 1965. doi: 10.1063/1.1761178.
- S. M. Hassanizadeh and W. G. Gray. Thermodynamic basis of capillary pressure in porous media. *Water Resources Research*, 29:3389–3405, 1993. doi: 10.1029/93wr01495.
- Z. Heinemann, C. Brand, M. Munka, Y. Chen, et al. Modeling reservoir geometry with irregular grids. In *SPE Symposium on Reservoir Simulation*. Society of Petroleum Engineers, 1989.
- R. Helmig. *Multiphase flow and transport processes in the subsurface: a contribution to the modeling of hydrosystems*. Springer-Verlag, 1997.
- B. R. Hollis. Real-gas flow properties for NASA Langley Research Center aerothermodynamic facilities complex wind tunnels. Technical report, 1996.
- V. Joekar-Niasar. *Capillarity Effects in Porous Media*. PhD thesis, Utrecht University, 2010.
- V. Joekar-Niasar, S. M. Hassanizadeh, and H. K. Dahle. Non-equilibrium effects in capillarity and interfacial area in two-phase flow: Dynamic pore-network modelling. *Journal of Fluid Mechanics*, 655:38–71, 2010. doi: 10.1017/s0022112010000704.
- W. M. Kays, M. E. Crawford, and B. Weigand. *Convective heat and mass transfer*. McGraw-Hill Higher Education, 4th edition, 2005. ISBN 9780071238298.
- T. Koch, D. Gläser, K. Weishaupt, S. Ackermann, M. Beck, B. Becker, S. Burbulla, H. Class, E. Coltman, S. Emmert, et al. Dumux 3—an open-source simulator for solving flow and transport problems in porous media with a focus on model coupling. *Computers & Mathematics with Applications*, 2020. doi: 10.1016/j.camwa.2020.02.012.
- E. C. Kumbur, K. V. Sharp, and M. M. Mench. Liquid droplet behavior and instability in a polymer electrolyte fuel cell flow channel. *Journal of Power Sources*, 161:333–345, 2006.
- P. Linstrom and W. Mallard, editors. *NIST Chemistry WebBook, NIST Standard Reference Database Number 69*. National Institute of Standards and Technology, 2018. doi: <https://doi.org/10.18434/T4D303>.

-
- R. Masson, L. Trenty, and Y. Zhang. Coupling compositional liquid gas Darcy and free gas flows at porous and free-flow domains interface. *Journal of Computational Physics*, 321:708–728, 2016. doi: 10.1016/j.jcp.2016.06.003.
- K. Mosthaf, K. Baber, B. Flemisch, R. Helmig, A. Leijnse, I. Rybak, and B. Wohlmuth. A coupling concept for two-phase compositional porous-medium and single-phase compositional free flow. *Water Resources Research*, 47:W10522, 2011. doi: 10.1029/2011wr010685.
- R. Nicolaides and X. Wu. Analysis and convergence of the MAC scheme. II. Navier-Stokes equations. *Mathematics of Computation of the American Mathematical Society*, 65:29–44, 1996. doi: 10.1090/s0025-5718-96-00665-5.
- R. A. Nicolaides. Analysis and convergence of the MAC scheme. I. The linear problem. *SIAM Journal on Numerical Analysis*, 29:1579–1591, 1992. doi: 10.1137/0729091.
- D. Niu and G. H. Tang. Static and dynamic behavior of water droplet on solid surfaces with pillar-type nanostructures from molecular dynamics simulation. *International Journal of Heat and Mass Transfer*, 79:647–654, 2014. doi: 10.1016/j.ijheatmasstransfer.2014.08.047.
- J. A. Ochoa-Tapia and S. Whitaker. Momentum transfer at the boundary between a porous medium and a homogeneous fluid - I. Theoretical development. *International Journal of Heat and Mass Transfer*, 38:2635–2646, 1995. doi: 10.1016/0017-9310(94)00346-w.
- L. Ostrowski, F. C. Massa, and C. Rohde. A phase field approach to compressible droplet impingement. In G. Lamanna, S. Tonini, G. E. Cossali, and B. Weigand, editors, *Droplet Interactions and Spray Processes*, pages 113–126. Springer International Publishing, 2020.
- T. Petrova and R. Dooley. Revised release on surface tension of ordinary water substance. *Proceedings of the International Association for the Properties of Water and Steam, Moscow, Russia*, pages 23–27, 2014.
- R. Picknett and R. Bexon. The evaporation of sessile or pendant drops in still air. *Journal of Colloid and Interface Science*, 61(2):336–350, 1977.

- C. Qin, D. Rensink, S. M. Hassanizadeh, and S. Fell. Direct simulation of liquid water dynamics in the gas channel of a polymer electrolyte fuel cell. *Journal of the Electrochemical Society*, 159:B434–B443, 2012. doi: 10.1149/2.004205jes.
- C. Qin, S. M. Hassanizadeh, and L. M. Van Oosterhout. Pore-network modeling of water and vapor transport in the micro porous layer and gas diffusion layer of a polymer electrolyte fuel cell. *Computation*, 4:21, 2016. doi: 10.3390/computation4020021.
- R. C. Reid, J. M. Prausnitz, and B. E. Poling. *The properties of gases and liquids*. 1987.
- D. Rivière and I. Yotov. Locally conservative coupling of Stokes and Darcy flows. *SIAM Journal on Numerical Analysis*, 42:1959–1977, 2005. doi: 10.1137/s0036142903427640.
- I. Rybak, J. Magiera, R. Helmig, and C. Rohde. Multirate time integration for coupled saturated/unsaturated porous medium and free flow systems. *Computational Geosciences*, 19:299–309, 2015. doi: 10.1007/s10596-015-9469-8.
- P. G. Saffman. On the boundary condition at the surface of a porous medium. *Studies in Applied Mathematics*, 50:93–101, 1971. doi: 10.1002/sapm197150293.
- M. Santini, M. Guilizzoni, and S. Fest-Santini. X-ray computed microtomography for drop shape analysis and contact angle measurement. *Journal of colloid and interface science*, 409:204–210, 2013. doi: 10.1016/j.jcis.2013.06.036.
- H. Schlichting and K. Gersten. *Grenzschicht-theorie*. Springer-Verlag, 2006.
- U. Shavit. Special issue on "Transport phenomena at the interface between fluid and porous domains". *Transport in Porous Media*, 78:327–330, 2009. doi: 10.1007/s11242-009-9414-1.
- H. Song, Y. Lee, S. Jin, H.-Y. Kim, and J. Y. Yoo. Prediction of sessile drop evaporation considering surface wettability. *Microelectronic Engineering*, 88:3249–3255, 2011. doi: 10.1016/j.mee.2011.07.015.
- A. Theodorakakos, T. Ous, M. Gavaises, J. M. Nouri, N. Nikolopoulos, and H. Yanagihara. Dynamics of water droplets detached from porous surfaces of relevance to PEM fuel cells. *Journal of Colloid and Interface Science*, 300:673–687, 2006. doi: 10.1016/j.jcis.2006.04.021.

-
- F. J. Valdés-Parada, B. Goyeau, and J. A. Ochoa-Tapia. Diffusive mass transfer between a microporous medium and a homogeneous fluid: Jump boundary conditions. *Chemical Engineering Science*, 61:1692–1704, 2006. doi: 10.1016/j.ces.2005.10.005.
- M. T. van Genuchten. A closed-form equation for predicting the hydraulic conductivity of unsaturated soils 1. *Soil science society of America journal*, 44:892–898, 1980. doi: 10.2136/sssaj1980.03615995004400050002x.
- N. B. Vargaftik. Tables on the thermophysical properties of liquids and gases in normal and dissociated states. 1975.
- L. Wang and J. Sun. Lattice Boltzmann modeling for the coalescence between a free droplet in gases and a sessile droplet on wettable substrate with contact angle hysteresis. *Proceedings of the Institution of Mechanical Engineers, Part C: Journal of Mechanical Engineering Science*, 232:431–444, 2018. doi: 10.1177/0954406217729717.
- J. C. Ward. Turbulent flow in porous media. *Journal of the Hydraulics Division*, 90(5): 1–12, 1964. doi: 10.1061/JYCEAJ.0001096.
- K. Weishaupt, V. Joekar-Niasar, and R. Helmig. An efficient coupling of free flow and porous media flow using the pore-network modeling approach. *Journal of Computational Physics: X*, 1:100011, 2019. doi: 10.1016/j.jcpx.2019.100011.
- R. N. Wenzel. Resistance of solid surfaces to wetting by water. *Industrial & Engineering Chemistry*, 28:988–994, 1936. doi: 10.1021/ie50320a024.
- F. M. White. *Fluid Mechanics*. McGraw-Hill Inc, 1968.
- J. Wilms. *Evaporation of Multicomponent Droplets*. PhD thesis, University of Stuttgart, 2005.
- M. Wolff, Y. Cao, B. Flemisch, R. Helmig, and B. Wohlmuth. Multi-point flux approximation L-method in 3D: numerical convergence and application to two-phase flow through porous media. *Radon Ser. Comput. Appl. Math., De Gruyter*, 12:39–80, 2013.
- T. Young. III. An essay on the cohesion of fluids. *Philosophical Transactions of the Royal Society of London*, (95):65–87, 1805. doi: 10.1098/rstl.1805.0005.
- F. Y. Zhang, X. G. Yang, and C. Y. Wang. Liquid water removal from a polymer electrolyte fuel cell. *Journal of The Electrochemical Society*, 153:A225–A232, 2006. doi: 10.1149/1.2138675.

Acknowledgments

"Every drop in the ocean counts." Yoko Ono.

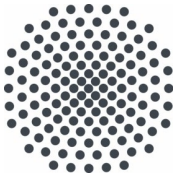
Of the many people who supported and motivated me throughout the last years, I would first like to thank my boss and supervisor, Rainer Helmig. Thank you for the fruitful discussions, your scientific advice, great patience and contagious enthusiasm.

I want to thank my colleagues at LH2 for the friendly atmosphere and the mutual support. For the after-work activities, special thanks to the persistent runners and pub-goers. A big thanks to Bernd and everyone else for putting a lot of time and effort into improving DuMu^x continuously. In addition, thanks to the DROFIT members for the interesting discussions in Stuttgart and Bergamo. Thank you Lukas for the productive work during the summer school and beyond.

I thank Prof. Bernhard Weigand and Prof. Maurizio Santini for being my co-examiners, and Dr.-Ing. Stephanie Fest-Santini for conducting the experiments. The interesting discussions I had with all of you really helped me to understand drops and their behavior.

I would like to thank the Deutsche Forschungsgemeinschaft for funding my work via the International Research Training Group "Droplet Interaction Technologies" (DROFIT) and the SFB 1313 "Interface-Driven Multi-Field Processes in Porous Media – Flow, Transport and Deformation".

A special thanks to my family and friends for always supporting me, especially during the last years. Thank you Sven for your extensive support and never-ending patience, and for all the delicious meals you prepared to keep me energized :) Last but not least, I would like to thank the tiny human being in my belly for the motivational kicks and pushes over the past few months. I can't wait to meet you.



Institut für Wasser- und Umweltsystemmodellierung Universität Stuttgart

Pfaffenwaldring 61
70569 Stuttgart (Vaihingen)
Telefon (0711) 685 - 60156
Telefax (0711) 685 - 51073
E-Mail: iws@iws.uni-stuttgart.de
<http://www.iws.uni-stuttgart.de>

Direktoren

Prof. Dr. rer. nat. Dr.-Ing. András Bárdossy
Prof. Dr.-Ing. Rainer Helmig
Prof. Dr.-Ing. Wolfgang Nowak
Prof. Dr.-Ing. Silke Wieprecht

Vorstand (Stand 1.5.2019)

Prof. Dr. rer. nat. Dr.-Ing. A. Bárdossy
Prof. Dr.-Ing. R. Helmig
Prof. Dr.-Ing. W. Nowak
Prof. Dr.-Ing. S. Wieprecht
Prof. Dr. J.A. Sander Huisman
Jürgen Braun, PhD
apl. Prof. Dr.-Ing. H. Class
PD Dr.-Ing. Claus Haslauer
Stefan Haun, PhD
PD Dr.-Ing. habil. Sergey Oladyshkin
Dr. rer. nat. J. Seidel
Dr.-Ing. K. Terheiden

Emeriti

Prof. Dr.-Ing. habil. Dr.-Ing. E.h. Jürgen Giesecke
Prof. Dr.h.c. Dr.-Ing. E.h. Helmut Kobus, PhD

Lehrstuhl für Wasserbau und Wassermengenwirtschaft

Leiterin: Prof. Dr.-Ing. Silke Wieprecht
Stellv.: Dr.-Ing. Kristina Terheiden
Versuchsanstalt für Wasserbau
Leiter: Stefan Haun, PhD

Lehrstuhl für Hydromechanik und Hydrosystemmodellierung

Leiter: Prof. Dr.-Ing. Rainer Helmig
Stellv.: apl. Prof. Dr.-Ing. Holger Class

Lehrstuhl für Hydrologie und Geohydrologie

Leiter: Prof. Dr. rer. nat. Dr.-Ing. András Bárdossy
Stellv.: Dr. rer. nat. Jochen Seidel
Hydrogeophysik der Vadosen Zone
(mit Forschungszentrum Jülich)
Leiter: Prof. Dr. J.A. Sander Huisman

Lehrstuhl für Stochastische Simulation und Sicherheitsforschung für Hydrosysteme

Leiter: Prof. Dr.-Ing. Wolfgang Nowak
Stellv.: PD Dr.-Ing. habil. Sergey Oladyshkin

VEGAS, Versuchseinrichtung zur Grundwasser- und Altlastensanierung

Leiter: Jürgen Braun, PhD
PD Dr.-Ing. Claus Haslauer

Verzeichnis der Mitteilungshefte

- 1 Röhnisch, Arthur: *Die Bemühungen um eine Wasserbauliche Versuchsanstalt an der Technischen Hochschule Stuttgart*, und Fattah Abouleid, Abdel: *Beitrag zur Berechnung einer in lockeren Sand gerammten, zweifach verankerten Spundwand*, 1963
- 2 Marotz, Günter: *Beitrag zur Frage der Standfestigkeit von dichten Asphaltbelägen im Großwasserbau*, 1964
- 3 Gurr, Siegfried: *Beitrag zur Berechnung zusammengesetzter ebener Flächentragwerke unter besonderer Berücksichtigung ebener Stauwände, mit Hilfe von Randwert- und Lastwertmatrizen*, 1965
- 4 Plica, Peter: *Ein Beitrag zur Anwendung von Schalenkonstruktionen im Stahlwasserbau*, und Petrikat, Kurt: *Möglichkeiten und Grenzen des wasserbaulichen Versuchswesens*, 1966

- 5 Plate, Erich: *Beitrag zur Bestimmung der Windgeschwindigkeitsverteilung in der durch eine Wand gestörten bodennahen Luftschicht*, und
Röhnisch, Arthur; Marotz, Günter: *Neue Baustoffe und Bauausführungen für den Schutz der Böschungen und der Sohle von Kanälen, Flüssen und Häfen; Gestehungskosten und jeweilige Vorteile*, sowie
Unny, T.E.: *Schwingungsuntersuchungen am Kegelstrahlschieber*, 1967
- 6 Seiler, Erich: *Die Ermittlung des Anlagenwertes der bundeseigenen Binnenschiffahrtsstraßen und Talsperren und des Anteils der Binnenschifffahrt an diesem Wert*, 1967
- 7 *Sonderheft anlässlich des 65. Geburtstages von Prof. Arthur Röhnisch mit Beiträgen von*
Benk, Dieter; Breitling, J.; Gurr, Siegfried; Haberhauer, Robert; Honekamp, Hermann; Kuz, Klaus Dieter; Marotz, Günter; Mayer-Vorfelder, Hans-Jörg; Miller, Rudolf; Plate, Erich J.; Radomski, Helge; Schwarz, Helmut; Vollmer, Ernst; Wildenhahn, Eberhard; 1967
- 8 Jumikis, Alfred: *Beitrag zur experimentellen Untersuchung des Wassernachschubs in einem gefrierenden Boden und die Beurteilung der Ergebnisse*, 1968
- 9 Marotz, Günter: *Technische Grundlagen einer Wasserspeicherung im natürlichen Untergrund*, 1968
- 10 Radomski, Helge: *Untersuchungen über den Einfluß der Querschnittsform wellenförmiger Spundwände auf die statischen und rammtechnischen Eigenschaften*, 1968
- 11 Schwarz, Helmut: *Die Grenztragfähigkeit des Baugrundes bei Einwirkung vertikal gezogener Ankerplatten als zweidimensionales Bruchproblem*, 1969
- 12 Erbel, Klaus: *Ein Beitrag zur Untersuchung der Metamorphose von Mittelgebirgsschneedecken unter besonderer Berücksichtigung eines Verfahrens zur Bestimmung der thermischen Schneequalität*, 1969
- 13 Westhaus, Karl-Heinz: *Der Strukturwandel in der Binnenschifffahrt und sein Einfluß auf den Ausbau der Binnenschiffskanäle*, 1969
- 14 Mayer-Vorfelder, Hans-Jörg: *Ein Beitrag zur Berechnung des Erdwiderstandes unter Ansatz der logarithmischen Spirale als Gleitflächenfunktion*, 1970
- 15 Schulz, Manfred: *Berechnung des räumlichen Erddruckes auf die Wandung kreiszylindrischer Körper*, 1970
- 16 Mobasseri, Manoutschehr: *Die Rippenstützmauer. Konstruktion und Grenzen ihrer Standicherheit*, 1970
- 17 Benk, Dieter: *Ein Beitrag zum Betrieb und zur Bemessung von Hochwasserrückhaltebecken*, 1970
- 18 Gàl, Attila: *Bestimmung der mitschwingenden Wassermasse bei überströmten Fischbauchklappen mit kreiszylindrischem Staublech*, 1971, vergriffen
- 19 Kuz, Klaus Dieter: *Ein Beitrag zur Frage des Einsetzens von Kavitationserscheinungen in einer Düsenströmung bei Berücksichtigung der im Wasser gelösten Gase*, 1971, vergriffen
- 20 Schaak, Hartmut: *Verteilleitungen von Wasserkraftanlagen*, 1971
- 21 *Sonderheft zur Eröffnung der neuen Versuchsanstalt des Instituts für Wasserbau der Universität Stuttgart mit Beiträgen von*
Brombach, Hansjörg; Dirksen, Wolfram; Gàl, Attila; Gerlach, Reinhard; Giesecke, Jürgen; Holthoff, Franz-Josef; Kuz, Klaus Dieter; Marotz, Günter; Minor, Hans-Erwin; Petrikat, Kurt; Röhnisch, Arthur; Rueff, Helge; Schwarz, Helmut; Vollmer, Ernst; Wildenhahn, Eberhard; 1972
- 22 Wang, Chung-su: *Ein Beitrag zur Berechnung der Schwingungen an Kegelstrahlschiebern*, 1972
- 23 Mayer-Vorfelder, Hans-Jörg: *Erdwiderstandsbeiwerte nach dem Ohde-Variationsverfahren*, 1972
- 24 Minor, Hans-Erwin: *Beitrag zur Bestimmung der Schwingungsanfachungsfunktionen überströmter Stauklappen*, 1972, vergriffen
- 25 Brombach, Hansjörg: *Untersuchung strömungsmechanischer Elemente (Fluidik) und die Möglichkeit der Anwendung von Wirbelkammerelementen im Wasserbau*, 1972, vergriffen
- 26 Wildenhahn, Eberhard: *Beitrag zur Berechnung von Horizontalfilterbrunnen*, 1972

- 27 Steinlein, Helmut: *Die Eliminierung der Schwebstoffe aus Flußwasser zum Zweck der unterirdischen Wasserspeicherung, gezeigt am Beispiel der Iller*, 1972
- 28 Holthoff, Franz Josef: *Die Überwindung großer Hubhöhen in der Binnenschifffahrt durch Schwimmerhebwerke*, 1973
- 29 Röder, Karl: *Einwirkungen aus Baugrundbewegungen auf trog- und kastenförmige Konstruktionen des Wasser- und Tunnelbaues*, 1973
- 30 Kretschmer, Heinz: *Die Bemessung von Bogenstau mauern in Abhängigkeit von der Talform*, 1973
- 31 Honekamp, Hermann: *Beitrag zur Berechnung der Montage von Unterwasserpipelines*, 1973
- 32 Giesecke, Jürgen: *Die Wirbelkammertriode als neuartiges Steuerorgan im Wasserbau*, und Brombach, Hansjörg: *Entwicklung, Bauformen, Wirkungsweise und Steuereigenschaften von Wirbelkammerverstärkern*, 1974
- 33 Rueff, Helge: *Untersuchung der schwingungserregenden Kräfte an zwei hintereinander angeordneten Tiefschützen unter besonderer Berücksichtigung von Kavitation*, 1974
- 34 Röhnisch, Arthur: *Einpreßversuche mit Zementmörtel für Spannbeton - Vergleich der Ergebnisse von Modellversuchen mit Ausführungen in Hüllwellrohren*, 1975
- 35 *Sonderheft anlässlich des 65. Geburtstages von Prof. Dr.-Ing. Kurt Petrikat mit Beiträgen von:* Brombach, Hansjörg; Erbel, Klaus; Flinspach, Dieter; Fischer jr., Richard; Gál, Attila; Gerlach, Reinhard; Giesecke, Jürgen; Haberhauer, Robert; Hafner Edzard; Hausenblas, Bernhard; Horlacher, Hans-Burkhard; Hutarew, Andreas; Knoll, Manfred; Krummet, Ralph; Marotz, Günter; Merkle, Theodor; Miller, Christoph; Minor, Hans-Erwin; Neumayer, Hans; Rao, Syamala; Rath, Paul; Rueff, Helge; Ruppert, Jürgen; Schwarz, Wolfgang; Topal-Gökceli, Mehmet; Vollmer, Ernst; Wang, Chung-su; Weber, Hans-Georg; 1975
- 36 Berger, Jochum: *Beitrag zur Berechnung des Spannungszustandes in rotationssymmetrisch belasteten Kugelschalen veränderlicher Wandstärke unter Gas- und Flüssigkeitsdruck durch Integration schwach singulärer Differentialgleichungen*, 1975
- 37 Dirksen, Wolfram: *Berechnung instationärer Abflußvorgänge in gestauten Gerinnen mittels Differenzenverfahren und die Anwendung auf Hochwasserrückhaltebecken*, 1976
- 38 Horlacher, Hans-Burkhard: *Berechnung instationärer Temperatur- und Wärmespannungsfelder in langen mehrschichtigen Hohlzylindern*, 1976
- 39 Hafner, Edzard: *Untersuchung der hydrodynamischen Kräfte auf Baukörper im Tiefwasserbereich des Meeres*, 1977, ISBN 3-921694-39-6
- 40 Ruppert, Jürgen: *Über den Axialwirbelkammerverstärker für den Einsatz im Wasserbau*, 1977, ISBN 3-921694-40-X
- 41 Hutarew, Andreas: *Beitrag zur Beeinflussbarkeit des Sauerstoffgehalts in Fließgewässern an Abstürzen und Wehren*, 1977, ISBN 3-921694-41-8, vergriffen
- 42 Miller, Christoph: *Ein Beitrag zur Bestimmung der schwingungserregenden Kräfte an unterströmten Wehren*, 1977, ISBN 3-921694-42-6
- 43 Schwarz, Wolfgang: *Druckstoßberechnung unter Berücksichtigung der Radial- und Längsverschiebungen der Rohrwandung*, 1978, ISBN 3-921694-43-4
- 44 Kinzelbach, Wolfgang: *Numerische Untersuchungen über den optimalen Einsatz variabler Kühlsysteme einer Kraftwerkskette am Beispiel Oberrhein*, 1978, ISBN 3-921694-44-2
- 45 Barczewski, Baldur: *Neue Meßmethoden für Wasser-Luftgemische und deren Anwendung auf zweiphasige Auftriebsstrahlen*, 1979, ISBN 3-921694-45-0
- 46 Neumayer, Hans: *Untersuchung der Strömungsvorgänge in radialen Wirbelkammerverstärkern*, 1979, ISBN 3-921694-46-9
- 47 Elalfy, Youssef-Elhassan: *Untersuchung der Strömungsvorgänge in Wirbelkammerdioden und -drosseln*, 1979, ISBN 3-921694-47-7
- 48 Brombach, Hansjörg: *Automatisierung der Bewirtschaftung von Wasserspeichern*, 1981, ISBN 3-921694-48-5
- 49 Geldner, Peter: *Deterministische und stochastische Methoden zur Bestimmung der Selbstdichtung von Gewässern*, 1981, ISBN 3-921694-49-3, vergriffen

- 50 Mehlhorn, Hans: *Temperaturveränderungen im Grundwasser durch Brauchwassereinleitungen*, 1982, ISBN 3-921694-50-7, vergriffen
- 51 Hafner, Edzard: *Rohrleitungen und Behälter im Meer*, 1983, ISBN 3-921694-51-5
- 52 Rinnert, Bernd: *Hydrodynamische Dispersion in porösen Medien: Einfluß von Dichteunterschieden auf die Vertikalvermischung in horizontaler Strömung*, 1983, ISBN 3-921694-52-3, vergriffen
- 53 Lindner, Wulf: *Steuerung von Grundwasserentnahmen unter Einhaltung ökologischer Kriterien*, 1983, ISBN 3-921694-53-1, vergriffen
- 54 Herr, Michael; Herzer, Jörg; Kinzelbach, Wolfgang; Kobus, Helmut; Rinnert, Bernd: *Methoden zur rechnerischen Erfassung und hydraulischen Sanierung von Grundwasserkontaminationen*, 1983, ISBN 3-921694-54-X
- 55 Schmitt, Paul: *Wege zur Automatisierung der Niederschlagsermittlung*, 1984, ISBN 3-921694-55-8, vergriffen
- 56 Müller, Peter: *Transport und selektive Sedimentation von Schwebstoffen bei gestautem Abfluß*, 1985, ISBN 3-921694-56-6
- 57 El-Qawasmeh, Fuad: *Möglichkeiten und Grenzen der Tropfbewässerung unter besonderer Berücksichtigung der Verstopfungsanfälligkeit der Tropfelemente*, 1985, ISBN 3-921694-57-4, vergriffen
- 58 Kirchenbaur, Klaus: *Mikroprozessorgesteuerte Erfassung instationärer Druckfelder am Beispiel seegangsbelasteter Baukörper*, 1985, ISBN 3-921694-58-2
- 59 Kobus, Helmut (Hrsg.): *Modellierung des großräumigen Wärme- und Schadstofftransports im Grundwasser*, Tätigkeitsbericht 1984/85 (DFG-Forschergruppe an den Universitäten Hohenheim, Karlsruhe und Stuttgart), 1985, ISBN 3-921694-59-0, vergriffen
- 60 Spitz, Karlheinz: *Dispersion in porösen Medien: Einfluß von Inhomogenitäten und Dichteunterschieden*, 1985, ISBN 3-921694-60-4, vergriffen
- 61 Kobus, Helmut: *An Introduction to Air-Water Flows in Hydraulics*, 1985, ISBN 3-921694-61-2
- 62 Kaleris, Vassilios: *Erfassung des Austausches von Oberflächen- und Grundwasser in horizontalebene Grundwassermodellen*, 1986, ISBN 3-921694-62-0
- 63 Herr, Michael: *Grundlagen der hydraulischen Sanierung verunreinigter Porengrundwasserleiter*, 1987, ISBN 3-921694-63-9
- 64 Marx, Walter: *Berechnung von Temperatur und Spannung in Massenbeton infolge Hydratation*, 1987, ISBN 3-921694-64-7
- 65 Koschitzky, Hans-Peter: *Dimensionierungskonzept für Sohlbelüfter in Schußrinnen zur Vermeidung von Kavitationsschäden*, 1987, ISBN 3-921694-65-5
- 66 Kobus, Helmut (Hrsg.): *Modellierung des großräumigen Wärme- und Schadstofftransports im Grundwasser*, Tätigkeitsbericht 1986/87 (DFG-Forschergruppe an den Universitäten Hohenheim, Karlsruhe und Stuttgart) 1987, ISBN 3-921694-66-3
- 67 Söll, Thomas: *Berechnungsverfahren zur Abschätzung anthropogener Temperaturanomalien im Grundwasser*, 1988, ISBN 3-921694-67-1
- 68 Dittrich, Andreas; Westrich, Bernd: *Bodenseeufererosion, Bestandsaufnahme und Bewertung*, 1988, ISBN 3-921694-68-X, vergriffen
- 69 Huwe, Bernd; van der Ploeg, Rienk R.: *Modelle zur Simulation des Stickstoffhaushaltes von Standorten mit unterschiedlicher landwirtschaftlicher Nutzung*, 1988, ISBN 3-921694-69-8, vergriffen
- 70 Stephan, Karl: *Integration elliptischer Funktionen*, 1988, ISBN 3-921694-70-1
- 71 Kobus, Helmut; Zilliox, Lothaire (Hrsg.): *Nitratbelastung des Grundwassers, Auswirkungen der Landwirtschaft auf die Grundwasser- und Rohwasserbeschaffenheit und Maßnahmen zum Schutz des Grundwassers*. Vorträge des deutsch-französischen Kolloquiums am 6. Oktober 1988, Universitäten Stuttgart und Louis Pasteur Strasbourg (Vorträge in deutsch oder französisch, Kurzfassungen zweisprachig), 1988, ISBN 3-921694-71-X

- 72 Soyeaux, Renald: *Unterströmung von Stauanlagen auf klüftigem Untergrund unter Berücksichtigung laminarer und turbulenter Fließzustände*, 1991, ISBN 3-921694-72-8
- 73 Kohane, Roberto: *Berechnungsmethoden für Hochwasserabfluß in Fließgewässern mit überströmten Vorländern*, 1991, ISBN 3-921694-73-6
- 74 Hassinger, Reinhard: *Beitrag zur Hydraulik und Bemessung von Blocksteinrampen in flexibler Bauweise*, 1991, ISBN 3-921694-74-4, vergriffen
- 75 Schäfer, Gerhard: *Einfluß von Schichtenstrukturen und lokalen Einlagerungen auf die Längsdispersion in Porengrundwasserleitern*, 1991, ISBN 3-921694-75-2
- 76 Giesecke, Jürgen: *Vorträge, Wasserwirtschaft in stark besiedelten Regionen; Umweltforschung mit Schwerpunkt Wasserwirtschaft*, 1991, ISBN 3-921694-76-0
- 77 Huwe, Bernd: *Deterministische und stochastische Ansätze zur Modellierung des Stickstoffhaushalts landwirtschaftlich genutzter Flächen auf unterschiedlichem Skalenniveau*, 1992, ISBN 3-921694-77-9, vergriffen
- 78 Rommel, Michael: *Verwendung von Kluffdaten zur realitätsnahen Generierung von Kluffnetzen mit anschließender laminar-turbulenter Strömungsberechnung*, 1993, ISBN 3-92 1694-78-7
- 79 Marschall, Paul: *Die Ermittlung lokaler Stofffrachten im Grundwasser mit Hilfe von Einbohrloch-Meßverfahren*, 1993, ISBN 3-921694-79-5, vergriffen
- 80 Ptak, Thomas: *Stofftransport in heterogenen Porenaquiferen: Felduntersuchungen und stochastische Modellierung*, 1993, ISBN 3-921694-80-9, vergriffen
- 81 Haakh, Frieder: *Transientes Strömungsverhalten in Wirbelkammern*, 1993, ISBN 3-921694-81-7
- 82 Kobus, Helmut; Cirpka, Olaf; Barczewski, Baldur; Koschitzky, Hans-Peter: *Versuchseinrichtung zur Grundwasser- und Altlastensanierung VEGAS, Konzeption und Programmrahmen*, 1993, ISBN 3-921694-82-5
- 83 Zang, Weidong: *Optimaler Echtzeit-Betrieb eines Speichers mit aktueller Abflußregenerierung*, 1994, ISBN 3-921694-83-3, vergriffen
- 84 Franke, Hans-Jörg: *Stochastische Modellierung eines flächenhaften Stoffeintrages und Transports in Grundwasser am Beispiel der Pflanzenschutzmittelproblematik*, 1995, ISBN 3-921694-84-1
- 85 Lang, Ulrich: *Simulation regionaler Strömungs- und Transportvorgänge in Karstaquiferen mit Hilfe des Doppelkontinuum-Ansatzes: Methodenentwicklung und Parameteridentifikation*, 1995, ISBN 3-921694-85-X, vergriffen
- 86 Helmig, Rainer: *Einführung in die Numerischen Methoden der Hydromechanik*, 1996, ISBN 3-921694-86-8, vergriffen
- 87 Cirpka, Olaf: *CONTRACT: A Numerical Tool for Contaminant Transport and Chemical Transformations - Theory and Program Documentation -*, 1996, ISBN 3-921694-87-6
- 88 Haberlandt, Uwe: *Stochastische Synthese und Regionalisierung des Niederschlages für Schmutzfrachtberechnungen*, 1996, ISBN 3-921694-88-4
- 89 Croisé, Jean: *Extraktion von flüchtigen Chemikalien aus natürlichen Lockergesteinen mittels erzwungener Luftströmung*, 1996, ISBN 3-921694-89-2, vergriffen
- 90 Jorde, Klaus: *Ökologisch begründete, dynamische Mindestwasserregelungen bei Ausleitungskraftwerken*, 1997, ISBN 3-921694-90-6, vergriffen
- 91 Helmig, Rainer: *Gekoppelte Strömungs- und Transportprozesse im Untergrund - Ein Beitrag zur Hydrosystemmodellierung-*, 1998, ISBN 3-921694-91-4, vergriffen
- 92 Emmert, Martin: *Numerische Modellierung nichtisothermer Gas-Wasser Systeme in porösen Medien*, 1997, ISBN 3-921694-92-2
- 93 Kern, Ulrich: *Transport von Schweb- und Schadstoffen in staugeregelten Fließgewässern am Beispiel des Neckars*, 1997, ISBN 3-921694-93-0, vergriffen
- 94 Förster, Georg: *Druckstoßdämpfung durch große Luftblasen in Hochpunkten von Rohrleitungen* 1997, ISBN 3-921694-94-9

- 95 Cirpka, Olaf: *Numerische Methoden zur Simulation des reaktiven Mehrkomponententransports im Grundwasser*, 1997, ISBN 3-921694-95-7, vergriffen
- 96 Färber, Arne: *Wärmetransport in der ungesättigten Bodenzone: Entwicklung einer thermischen In-situ-Sanierungstechnologie*, 1997, ISBN 3-921694-96-5
- 97 Betz, Christoph: *Wasserdampfdestillation von Schadstoffen im porösen Medium: Entwicklung einer thermischen In-situ-Sanierungstechnologie*, 1998, SBN 3-921694-97-3
- 98 Xu, Yichun: *Numerical Modeling of Suspended Sediment Transport in Rivers*, 1998, ISBN 3-921694-98-1, vergriffen
- 99 Wüst, Wolfgang: *Geochemische Untersuchungen zur Sanierung CKW-kontaminierter Aquifere mit Fe(0)-Reaktionswänden*, 2000, ISBN 3-933761-02-2
- 100 Sheta, Hussam: *Simulation von Mehrphasenvorgängen in porösen Medien unter Einbeziehung von Hysterese-Effekten*, 2000, ISBN 3-933761-03-4
- 101 Ayros, Edwin: *Regionalisierung extremer Abflüsse auf der Grundlage statistischer Verfahren*, 2000, ISBN 3-933761-04-2, vergriffen
- 102 Huber, Ralf: *Compositional Multiphase Flow and Transport in Heterogeneous Porous Media*, 2000, ISBN 3-933761-05-0
- 103 Braun, Christopherus: *Ein Upscaling-Verfahren für Mehrphasenströmungen in porösen Medien*, 2000, ISBN 3-933761-06-9
- 104 Hofmann, Bernd: *Entwicklung eines rechnergestützten Managementsystems zur Beurteilung von Grundwasserschadensfällen*, 2000, ISBN 3-933761-07-7
- 105 Class, Holger: *Theorie und numerische Modellierung nichtisothermer Mehrphasenprozesse in NAPL-kontaminierten porösen Medien*, 2001, ISBN 3-933761-08-5
- 106 Schmidt, Reinhard: *Wasserdampf- und Heißluftinjektion zur thermischen Sanierung kontaminierter Standorte*, 2001, ISBN 3-933761-09-3
- 107 Josef, Reinhold: *Schadstoffextraktion mit hydraulischen Sanierungsverfahren unter Anwendung von grenzflächenaktiven Stoffen*, 2001, ISBN 3-933761-10-7
- 108 Schneider, Matthias: *Habitat- und Abflussmodellierung für Fließgewässer mit unscharfen Berechnungsansätzen*, 2001, ISBN 3-933761-11-5
- 109 Rathgeb, Andreas: *Hydrodynamische Bemessungsgrundlagen für Lockerdeckwerke an überströmbaren Erddämmen*, 2001, ISBN 3-933761-12-3
- 110 Lang, Stefan: *Parallele numerische Simulation instationärer Probleme mit adaptiven Methoden auf unstrukturierten Gittern*, 2001, ISBN 3-933761-13-1
- 111 Appt, Jochen; Stumpp Simone: *Die Bodensee-Messkampagne 2001, IWS/CWR Lake Constance Measurement Program 2001*, 2002, ISBN 3-933761-14-X
- 112 Heimerl, Stephan: *Systematische Beurteilung von Wasserkraftprojekten*, 2002, ISBN 3-933761-15-8, vergriffen
- 113 Iqbal, Amin: *On the Management and Salinity Control of Drip Irrigation*, 2002, ISBN 3-933761-16-6
- 114 Silberhorn-Hemminger, Annette: *Modellierung von Kluftaquifersystemen: Geostatistische Analyse und deterministisch-stochastische Kluftgenerierung*, 2002, ISBN 3-933761-17-4
- 115 Winkler, Angela: *Prozesse des Wärme- und Stofftransports bei der In-situ-Sanierung mit festen Wärmequellen*, 2003, ISBN 3-933761-18-2
- 116 Marx, Walter: *Wasserkraft, Bewässerung, Umwelt - Planungs- und Bewertungsschwerpunkte der Wasserbewirtschaftung*, 2003, ISBN 3-933761-19-0
- 117 Hinkelmann, Reinhard: *Efficient Numerical Methods and Information-Processing Techniques in Environment Water*, 2003, ISBN 3-933761-20-4
- 118 Samaniego-Eguiguren, Luis Eduardo: *Hydrological Consequences of Land Use / Land Cover and Climatic Changes in Mesoscale Catchments*, 2003, ISBN 3-933761-21-2
- 119 Neunhäuserer, Lina: *Diskretisierungsansätze zur Modellierung von Strömungs- und Transportprozessen in geklüftet-porösen Medien*, 2003, ISBN 3-933761-22-0
- 120 Paul, Maren: *Simulation of Two-Phase Flow in Heterogeneous Poros Media with Adaptive Methods*, 2003, ISBN 3-933761-23-9

- 121 Ehret, Uwe: *Rainfall and Flood Nowcasting in Small Catchments using Weather Radar*, 2003, ISBN 3-933761-24-7
- 122 Haag, Ingo: *Der Sauerstoffhaushalt staugeregelter Flüsse am Beispiel des Neckars - Analysen, Experimente, Simulationen -*, 2003, ISBN 3-933761-25-5
- 123 Appt, Jochen: *Analysis of Basin-Scale Internal Waves in Upper Lake Constance*, 2003, ISBN 3-933761-26-3
- 124 Hrsg.: Schrenk, Volker; Batereau, Katrin; Barczewski, Baldur; Weber, Karolin und Koschitzky, Hans-Peter: *Symposium Ressource Fläche und VEGAS - Statuskolloquium 2003, 30. September und 1. Oktober 2003*, 2003, ISBN 3-933761-27-1
- 125 Omar Khalil Ouda: *Optimisation of Agricultural Water Use: A Decision Support System for the Gaza Strip*, 2003, ISBN 3-933761-28-0
- 126 Batereau, Katrin: *Sensorbasierte Bodenluftmessung zur Vor-Ort-Erkundung von Schadensherden im Untergrund*, 2004, ISBN 3-933761-29-8
- 127 Witt, Oliver: *Erosionsstabilität von Gewässersedimenten mit Auswirkung auf den Stofftransport bei Hochwasser am Beispiel ausgewählter Stauhaltungen des Oberrheins*, 2004, ISBN 3-933761-30-1
- 128 Jakobs, Hartmut: *Simulation nicht-isothermer Gas-Wasser-Prozesse in komplexen Kluft-Matrix-Systemen*, 2004, ISBN 3-933761-31-X
- 129 Li, Chen-Chien: *Deterministisch-stochastisches Berechnungskonzept zur Beurteilung der Auswirkungen erosiver Hochwasserereignisse in Flusstauhaltungen*, 2004, ISBN 3-933761-32-8
- 130 Reichenberger, Volker; Helmig, Rainer; Jakobs, Hartmut; Bastian, Peter; Niessner, Jennifer: *Complex Gas-Water Processes in Discrete Fracture-Matrix Systems: Up-scaling, Mass-Conservative Discretization and Efficient Multilevel Solution*, 2004, ISBN 3-933761-33-6
- 131 Hrsg.: Barczewski, Baldur; Koschitzky, Hans-Peter; Weber, Karolin; Wege, Ralf: *VEGAS - Statuskolloquium 2004*, Tagungsband zur Veranstaltung am 05. Oktober 2004 an der Universität Stuttgart, Campus Stuttgart-Vaihingen, 2004, ISBN 3-933761-34-4
- 132 Asie, Kemal Jabir: *Finite Volume Models for Multiphase Multicomponent Flow through Porous Media*. 2005, ISBN 3-933761-35-2
- 133 Jacoub, George: *Development of a 2-D Numerical Module for Particulate Contaminant Transport in Flood Retention Reservoirs and Impounded Rivers*, 2004, ISBN 3-933761-36-0
- 134 Nowak, Wolfgang: *Geostatistical Methods for the Identification of Flow and Transport Parameters in the Subsurface*, 2005, ISBN 3-933761-37-9
- 135 Süß, Mia: *Analysis of the influence of structures and boundaries on flow and transport processes in fractured porous media*, 2005, ISBN 3-933761-38-7
- 136 Jose, Surabhin Chackiath: *Experimental Investigations on Longitudinal Dispersive Mixing in Heterogeneous Aquifers*, 2005, ISBN: 3-933761-39-5
- 137 Filiz, Fulya: *Linking Large-Scale Meteorological Conditions to Floods in Mesoscale Catchments*, 2005, ISBN 3-933761-40-9
- 138 Qin, Minghao: *Wirklichkeitsnahe und recheneffiziente Ermittlung von Temperatur und Spannungen bei großen RCC-Staumauern*, 2005, ISBN 3-933761-41-7
- 139 Kobayashi, Kenichiro: *Optimization Methods for Multiphase Systems in the Subsurface - Application to Methane Migration in Coal Mining Areas*, 2005, ISBN 3-933761-42-5
- 140 Rahman, Md. Arifur: *Experimental Investigations on Transverse Dispersive Mixing in Heterogeneous Porous Media*, 2005, ISBN 3-933761-43-3
- 141 Schrenk, Volker: *Ökobilanzen zur Bewertung von Altlastensanierungsmaßnahmen*, 2005, ISBN 3-933761-44-1
- 142 Hundecha, Hirpa Yeshewatesfa: *Regionalization of Parameters of a Conceptual Rainfall-Runoff Model*, 2005, ISBN: 3-933761-45-X
- 143 Wege, Ralf: *Untersuchungs- und Überwachungsmethoden für die Beurteilung natürlicher Selbstreinigungsprozesse im Grundwasser*, 2005, ISBN 3-933761-46-8

- 144 Breiting, Thomas: *Techniken und Methoden der Hydroinformatik - Modellierung von komplexen Hydrosystemen im Untergrund*, 2006, ISBN 3-933761-47-6
- 145 Hrsg.: Braun, Jürgen; Koschitzky, Hans-Peter; Müller, Martin: *Ressource Untergrund: 10 Jahre VEGAS: Forschung und Technologieentwicklung zum Schutz von Grundwasser und Boden*, Tagungsband zur Veranstaltung am 28. und 29. September 2005 an der Universität Stuttgart, Campus Stuttgart-Vaihingen, 2005, ISBN 3-933761-48-4
- 146 Rojanschi, Vlad: *Abflusskonzentration in mesoskaligen Einzugsgebieten unter Berücksichtigung des Sickerraumes*, 2006, ISBN 3-933761-49-2
- 147 Winkler, Nina Simone: *Optimierung der Steuerung von Hochwasserrückhaltebeckensystemen*, 2006, ISBN 3-933761-50-6
- 148 Wolf, Jens: *Räumlich differenzierte Modellierung der Grundwasserströmung alluvialer Aquifere für mesoskalige Einzugsgebiete*, 2006, ISBN: 3-933761-51-4
- 149 Kohler, Beate: *Externe Effekte der Laufwasserkraftnutzung*, 2006, ISBN 3-933761-52-2
- 150 Hrsg.: Braun, Jürgen; Koschitzky, Hans-Peter; Stuhmann, Matthias: *VEGAS-Statuskolloquium 2006*, Tagungsband zur Veranstaltung am 28. September 2006 an der Universität Stuttgart, Campus Stuttgart-Vaihingen, 2006, ISBN 3-933761-53-0
- 151 Niessner, Jennifer: *Multi-Scale Modeling of Multi-Phase - Multi-Component Processes in Heterogeneous Porous Media*, 2006, ISBN 3-933761-54-9
- 152 Fischer, Markus: *Beanspruchung eingeeerdeter Rohrleitungen infolge Austrocknung bindiger Böden*, 2006, ISBN 3-933761-55-7
- 153 Schneck, Alexander: *Optimierung der Grundwasserbewirtschaftung unter Berücksichtigung der Belange der Wasserversorgung, der Landwirtschaft und des Naturschutzes*, 2006, ISBN 3-933761-56-5
- 154 Das, Tapash: *The Impact of Spatial Variability of Precipitation on the Predictive Uncertainty of Hydrological Models*, 2006, ISBN 3-33761-57-3
- 155 Bielinski, Andreas: *Numerical Simulation of CO₂ sequestration in geological formations*, 2007, ISBN 3-933761-58-1
- 156 Mödinger, Jens: *Entwicklung eines Bewertungs- und Entscheidungsunterstützungssystems für eine nachhaltige regionale Grundwasserbewirtschaftung*, 2006, ISBN 3-933761-60-3
- 157 Manthey, Sabine: *Two-phase flow processes with dynamic effects in porous media - parameter estimation and simulation*, 2007, ISBN 3-933761-61-1
- 158 Pozos Estrada, Oscar: *Investigation on the Effects of Entrained Air in Pipelines*, 2007, ISBN 3-933761-62-X
- 159 Ochs, Steffen Oliver: *Steam injection into saturated porous media – process analysis including experimental and numerical investigations*, 2007, ISBN 3-933761-63-8
- 160 Marx, Andreas: *Einsatz gekoppelter Modelle und Wetterradar zur Abschätzung von Niederschlagsintensitäten und zur Abflussvorhersage*, 2007, ISBN 3-933761-64-6
- 161 Hartmann, Gabriele Maria: *Investigation of Evapotranspiration Concepts in Hydrological Modelling for Climate Change Impact Assessment*, 2007, ISBN 3-933761-65-4
- 162 Kebede Gurmessa, Tesfaye: *Numerical Investigation on Flow and Transport Characteristics to Improve Long-Term Simulation of Reservoir Sedimentation*, 2007, ISBN 3-933761-66-2
- 163 Trifković, Aleksandar: *Multi-objective and Risk-based Modelling Methodology for Planning, Design and Operation of Water Supply Systems*, 2007, ISBN 3-933761-67-0
- 164 Göttinger, Jens: *Distributed Conceptual Hydrological Modelling - Simulation of Climate, Land Use Change Impact and Uncertainty Analysis*, 2007, ISBN 3-933761-68-9
- 165 Hrsg.: Braun, Jürgen; Koschitzky, Hans-Peter; Stuhmann, Matthias: *VEGAS – Kolloquium 2007*, Tagungsband zur Veranstaltung am 26. September 2007 an der Universität Stuttgart, Campus Stuttgart-Vaihingen, 2007, ISBN 3-933761-69-7
- 166 Freeman, Beau: *Modernization Criteria Assessment for Water Resources Planning; Klamath Irrigation Project, U.S.*, 2008, ISBN 3-933761-70-0

- 167 Dreher, Thomas: *Selektive Sedimentation von Feinstschwebstoffen in Wechselwirkung mit wandnahen turbulenten Strömungsbedingungen*, 2008, ISBN 3-933761-71-9
- 168 Yang, Wei: *Discrete-Continuous Downscaling Model for Generating Daily Precipitation Time Series*, 2008, ISBN 3-933761-72-7
- 169 Kopecki, Ianina: *Calculational Approach to FST-Hemispheres for Multiparametrical Benthos Habitat Modelling*, 2008, ISBN 3-933761-73-5
- 170 Brommundt, Jürgen: *Stochastische Generierung räumlich zusammenhängender Niederschlagszeitreihen*, 2008, ISBN 3-933761-74-3
- 171 Papafotiou, Alexandros: *Numerical Investigations of the Role of Hysteresis in Heterogeneous Two-Phase Flow Systems*, 2008, ISBN 3-933761-75-1
- 172 He, Yi: *Application of a Non-Parametric Classification Scheme to Catchment Hydrology*, 2008, ISBN 978-3-933761-76-7
- 173 Wagner, Sven: *Water Balance in a Poorly Gauged Basin in West Africa Using Atmospheric Modelling and Remote Sensing Information*, 2008, ISBN 978-3-933761-77-4
- 174 Hrsg.: Braun, Jürgen; Koschitzky, Hans-Peter; Stuhmann, Matthias; Schrenk, Volker: *VEGAS-Kolloquium 2008 Ressource Fläche III*, Tagungsband zur Veranstaltung am 01. Oktober 2008 an der Universität Stuttgart, Campus Stuttgart-Vaihingen, 2008, ISBN 978-3-933761-78-1
- 175 Patil, Sachin: *Regionalization of an Event Based Nash Cascade Model for Flood Predictions in Ungauged Basins*, 2008, ISBN 978-3-933761-79-8
- 176 Assteerawatt, Anongnart: *Flow and Transport Modelling of Fractured Aquifers based on a Geostatistical Approach*, 2008, ISBN 978-3-933761-80-4
- 177 Karnahl, Joachim Alexander: *2D numerische Modellierung von multifractionalem Schwebstoff- und Schadstofftransport in Flüssen*, 2008, ISBN 978-3-933761-81-1
- 178 Hiester, Uwe: *Technologieentwicklung zur In-situ-Sanierung der ungesättigten Bodenzone mit festen Wärmequellen*, 2009, ISBN 978-3-933761-82-8
- 179 Laux, Patrick: *Statistical Modeling of Precipitation for Agricultural Planning in the Volta Basin of West Africa*, 2009, ISBN 978-3-933761-83-5
- 180 Ehsan, Saqib: *Evaluation of Life Safety Risks Related to Severe Flooding*, 2009, ISBN 978-3-933761-84-2
- 181 Prohaska, Sandra: *Development and Application of a 1D Multi-Strip Fine Sediment Transport Model for Regulated Rivers*, 2009, ISBN 978-3-933761-85-9
- 182 Kopp, Andreas: *Evaluation of CO₂ Injection Processes in Geological Formations for Site Screening*, 2009, ISBN 978-3-933761-86-6
- 183 Ebigbo, Anozie: *Modelling of biofilm growth and its influence on CO₂ and water (two-phase) flow in porous media*, 2009, ISBN 978-3-933761-87-3
- 184 Freiboth, Sandra: *A phenomenological model for the numerical simulation of multiphase multicomponent processes considering structural alterations of porous media*, 2009, ISBN 978-3-933761-88-0
- 185 Zöllner, Frank: *Implementierung und Anwendung netzfreier Methoden im Konstruktiven Wasserbau und in der Hydromechanik*, 2009, ISBN 978-3-933761-89-7
- 186 Vasin, Milos: *Influence of the soil structure and property contrast on flow and transport in the unsaturated zone*, 2010, ISBN 978-3-933761-90-3
- 187 Li, Jing: *Application of Copulas as a New Geostatistical Tool*, 2010, ISBN 978-3-933761-91-0
- 188 AghaKouchak, Amir: *Simulation of Remotely Sensed Rainfall Fields Using Copulas*, 2010, ISBN 978-3-933761-92-7
- 189 Thapa, Pawan Kumar: *Physically-based spatially distributed rainfall runoff modelling for soil erosion estimation*, 2010, ISBN 978-3-933761-93-4
- 190 Wurms, Sven: *Numerische Modellierung der Sedimentationsprozesse in Retentionsanlagen zur Steuerung von Stoffströmen bei extremen Hochwasserabflussereignissen*, 2011, ISBN 978-3-933761-94-1

- 191 Merkel, Uwe: *Unsicherheitsanalyse hydraulischer Einwirkungen auf Hochwasserschutzdeiche und Steigerung der Leistungsfähigkeit durch adaptive Strömungsmodellierung*, 2011, ISBN 978-3-933761-95-8
- 192 Fritz, Jochen: *A Decoupled Model for Compositional Non-Isothermal Multiphase Flow in Porous Media and Multiphysics Approaches for Two-Phase Flow*, 2010, ISBN 978-3-933761-96-5
- 193 Weber, Karolin (Hrsg.): *12. Treffen junger WissenschaftlerInnen an Wasserbauinstituten*, 2010, ISBN 978-3-933761-97-2
- 194 Bliedernicht, Jan-Geert: *Probability Forecasts of Daily Areal Precipitation for Small River Basins*, 2011, ISBN 978-3-933761-98-9
- 195 Hrsg.: Koschitzky, Hans-Peter; Braun, Jürgen: *VEGAS-Kolloquium 2010 In-situ-Sanierung - Stand und Entwicklung Nano und ISCO -*, Tagungsband zur Veranstaltung am 07. Oktober 2010 an der Universität Stuttgart, Campus Stuttgart-Vaihingen, 2010, ISBN 978-3-933761-99-6
- 196 Gafurov, Abror: *Water Balance Modeling Using Remote Sensing Information - Focus on Central Asia*, 2010, ISBN 978-3-942036-00-9
- 197 Mackenberg, Sylvia: *Die Quellstärke in der Sickerwasserprognose: Möglichkeiten und Grenzen von Labor- und Freilanduntersuchungen*, 2010, ISBN 978-3-942036-01-6
- 198 Singh, Shailesh Kumar: *Robust Parameter Estimation in Gauged and Ungauged Basins*, 2010, ISBN 978-3-942036-02-3
- 199 Doğan, Mehmet Onur: *Coupling of porous media flow with pipe flow*, 2011, ISBN 978-3-942036-03-0
- 200 Liu, Min: *Study of Topographic Effects on Hydrological Patterns and the Implication on Hydrological Modeling and Data Interpolation*, 2011, ISBN 978-3-942036-04-7
- 201 Geleta, Habtamu Itafa: *Watershed Sediment Yield Modeling for Data Scarce Areas*, 2011, ISBN 978-3-942036-05-4
- 202 Franke, Jörg: *Einfluss der Überwachung auf die Versagenswahrscheinlichkeit von Staustufen*, 2011, ISBN 978-3-942036-06-1
- 203 Bakimchandra, Oinam: *Integrated Fuzzy-GIS approach for assessing regional soil erosion risks*, 2011, ISBN 978-3-942036-07-8
- 204 Alam, Muhammad Mahboob: *Statistical Downscaling of Extremes of Precipitation in Mesoscale Catchments from Different RCMs and Their Effects on Local Hydrology*, 2011, ISBN 978-3-942036-08-5
- 205 Hrsg.: Koschitzky, Hans-Peter; Braun, Jürgen: *VEGAS-Kolloquium 2011 Flache Geothermie - Perspektiven und Risiken*, Tagungsband zur Veranstaltung am 06. Oktober 2011 an der Universität Stuttgart, Campus Stuttgart-Vaihingen, 2011, ISBN 978-3-933761-09-2
- 206 Haslauer, Claus: *Analysis of Real-World Spatial Dependence of Subsurface Hydraulic Properties Using Copulas with a Focus on Solute Transport Behaviour*, 2011, ISBN 978-3-942036-10-8
- 207 Dung, Nguyen Viet: *Multi-objective automatic calibration of hydrodynamic models – development of the concept and an application in the Mekong Delta*, 2011, ISBN 978-3-942036-11-5
- 208 Hung, Nguyen Nghia: *Sediment dynamics in the floodplain of the Mekong Delta, Vietnam*, 2011, ISBN 978-3-942036-12-2
- 209 Kuhlmann, Anna: *Influence of soil structure and root water uptake on flow in the unsaturated zone*, 2012, ISBN 978-3-942036-13-9
- 210 Tuhtan, Jeffrey Andrew: *Including the Second Law Inequality in Aquatic Ecodynamics: A Modeling Approach for Alpine Rivers Impacted by Hydropeaking*, 2012, ISBN 978-3-942036-14-6
- 211 Tolossa, Habtamu: *Sediment Transport Computation Using a Data-Driven Adaptive Neuro-Fuzzy Modelling Approach*, 2012, ISBN 978-3-942036-15-3
- 212 Tatomir, Alexandru-Bodgan: *From Discrete to Continuum Concepts of Flow in Fractured Porous Media*, 2012, ISBN 978-3-942036-16-0

- 213 Erbertseder, Karin: *A Multi-Scale Model for Describing Cancer-Therapeutic Transport in the Human Lung*, 2012, ISBN 978-3-942036-17-7
- 214 Noack, Markus: *Modelling Approach for Interstitial Sediment Dynamics and Reproduction of Gravel Spawning Fish*, 2012, ISBN 978-3-942036-18-4
- 215 De Boer, Cjestrir Volkert: *Transport of Nano Sized Zero Valent Iron Colloids during Injection into the Subsurface*, 2012, ISBN 978-3-942036-19-1
- 216 Pfaff, Thomas: *Processing and Analysis of Weather Radar Data for Use in Hydrology*, 2013, ISBN 978-3-942036-20-7
- 217 Lebreuz, Hans-Henning: *Addressing the Input Uncertainty for Hydrological Modeling by a New Geostatistical Method*, 2013, ISBN 978-3-942036-21-4
- 218 Darcis, Melanie Yvonne: *Coupling Models of Different Complexity for the Simulation of CO₂ Storage in Deep Saline Aquifers*, 2013, ISBN 978-3-942036-22-1
- 219 Beck, Ferdinand: *Generation of Spatially Correlated Synthetic Rainfall Time Series in High Temporal Resolution - A Data Driven Approach*, 2013, ISBN 978-3-942036-23-8
- 220 Guthke, Philipp: *Non-multi-Gaussian spatial structures: Process-driven natural genesis, manifestation, modeling approaches, and influences on dependent processes*, 2013, ISBN 978-3-942036-24-5
- 221 Walter, Lena: *Uncertainty studies and risk assessment for CO₂ storage in geological formations*, 2013, ISBN 978-3-942036-25-2
- 222 Wolff, Markus: *Multi-scale modeling of two-phase flow in porous media including capillary pressure effects*, 2013, ISBN 978-3-942036-26-9
- 223 Mosthaf, Klaus Roland: *Modeling and analysis of coupled porous-medium and free flow with application to evaporation processes*, 2014, ISBN 978-3-942036-27-6
- 224 Leube, Philipp Christoph: *Methods for Physically-Based Model Reduction in Time: Analysis, Comparison of Methods and Application*, 2013, ISBN 978-3-942036-28-3
- 225 Rodríguez Fernández, Jhan Ignacio: *High Order Interactions among environmental variables: Diagnostics and initial steps towards modeling*, 2013, ISBN 978-3-942036-29-0
- 226 Eder, Maria Magdalena: *Climate Sensitivity of a Large Lake*, 2013, ISBN 978-3-942036-30-6
- 227 Greiner, Philipp: *Alkoholinjektion zur In-situ-Sanierung von CKW Schadensherden in Grundwasserleitern: Charakterisierung der relevanten Prozesse auf unterschiedlichen Skalen*, 2014, ISBN 978-3-942036-31-3
- 228 Lauser, Andreas: *Theory and Numerical Applications of Compositional Multi-Phase Flow in Porous Media*, 2014, ISBN 978-3-942036-32-0
- 229 Enzenhöfer, Rainer: *Risk Quantification and Management in Water Production and Supply Systems*, 2014, ISBN 978-3-942036-33-7
- 230 Faigle, Benjamin: *Adaptive modelling of compositional multi-phase flow with capillary pressure*, 2014, ISBN 978-3-942036-34-4
- 231 Oladyshkin, Sergey: *Efficient modeling of environmental systems in the face of complexity and uncertainty*, 2014, ISBN 978-3-942036-35-1
- 232 Sugimoto, Takayuki: *Copula based Stochastic Analysis of Discharge Time Series*, 2014, ISBN 978-3-942036-36-8
- 233 Koch, Jonas: *Simulation, Identification and Characterization of Contaminant Source Architectures in the Subsurface*, 2014, ISBN 978-3-942036-37-5
- 234 Zhang, Jin: *Investigations on Urban River Regulation and Ecological Rehabilitation Measures, Case of Shenzhen in China*, 2014, ISBN 978-3-942036-38-2
- 235 Siebel, Rüdiger: *Experimentelle Untersuchungen zur hydrodynamischen Belastung und Standsicherheit von Deckwerken an überströmbaren Erddämmen*, 2014, ISBN 978-3-942036-39-9
- 236 Baber, Katherina: *Coupling free flow and flow in porous media in biological and technical applications: From a simple to a complex interface description*, 2014, ISBN 978-3-942036-40-5

- 237 Nuske, Klaus Philipp: *Beyond Local Equilibrium — Relaxing local equilibrium assumptions in multiphase flow in porous media*, 2014, ISBN 978-3-942036-41-2
- 238 Geiges, Andreas: *Efficient concepts for optimal experimental design in nonlinear environmental systems*, 2014, ISBN 978-3-942036-42-9
- 239 Schwenck, Nicolas: *An XFEM-Based Model for Fluid Flow in Fractured Porous Media*, 2014, ISBN 978-3-942036-43-6
- 240 Chamorro Chávez, Alejandro: *Stochastic and hydrological modelling for climate change prediction in the Lima region, Peru*, 2015, ISBN 978-3-942036-44-3
- 241 Yulizar: *Investigation of Changes in Hydro-Meteorological Time Series Using a Depth-Based Approach*, 2015, ISBN 978-3-942036-45-0
- 242 Kretschmer, Nicole: *Impacts of the existing water allocation scheme on the Limarí watershed – Chile, an integrative approach*, 2015, ISBN 978-3-942036-46-7
- 243 Kramer, Matthias: *Luftbedarf von Freistrahlturbinen im Gegendruckbetrieb*, 2015, ISBN 978-3-942036-47-4
- 244 Hommel, Johannes: *Modeling biogeochemical and mass transport processes in the sub-surface: Investigation of microbially induced calcite precipitation*, 2016, ISBN 978-3-942036-48-1
- 245 Germer, Kai: *Wasserinfiltration in die ungesättigte Zone eines makroporösen Hanges und deren Einfluss auf die Hangstabilität*, 2016, ISBN 978-3-942036-49-8
- 246 Hörning, Sebastian: *Process-oriented modeling of spatial random fields using copulas*, 2016, ISBN 978-3-942036-50-4
- 247 Jambhekar, Vishal: *Numerical modeling and analysis of evaporative salinization in a coupled free-flow porous-media system*, 2016, ISBN 978-3-942036-51-1
- 248 Huang, Yingchun: *Study on the spatial and temporal transferability of conceptual hydrological models*, 2016, ISBN 978-3-942036-52-8
- 249 Kleinknecht, Simon Matthias: *Migration and retention of a heavy NAPL vapor and remediation of the unsaturated zone*, 2016, ISBN 978-3-942036-53-5
- 250 Kwakye, Stephen Oppong: *Study on the effects of climate change on the hydrology of the West African sub-region*, 2016, ISBN 978-3-942036-54-2
- 251 Kissinger, Alexander: *Basin-Scale Site Screening and Investigation of Possible Impacts of CO₂ Storage on Subsurface Hydrosystems*, 2016, ISBN 978-3-942036-55-9
- 252 Müller, Thomas: *Generation of a Realistic Temporal Structure of Synthetic Precipitation Time Series for Sewer Applications*, 2017, ISBN 978-3-942036-56-6
- 253 Grüninger, Christoph: *Numerical Coupling of Navier-Stokes and Darcy Flow for Soil-Water Evaporation*, 2017, ISBN 978-3-942036-57-3
- 254 Suroso: *Asymmetric Dependence Based Spatial Copula Models: Empirical Investigations and Consequences on Precipitation Fields*, 2017, ISBN 978-3-942036-58-0
- 255 Müller, Thomas; Mosthaf, Tobias; Gunzenhauser, Sarah; Seidel, Jochen; Bárdossy, András: *Grundlagenbericht Niederschlags-Simulator (NiedSim3)*, 2017, ISBN 978-3-942036-59-7
- 256 Mosthaf, Tobias: *New Concepts for Regionalizing Temporal Distributions of Precipitation and for its Application in Spatial Rainfall Simulation*, 2017, ISBN 978-3-942036-60-3
- 257 Fenrich, Eva Katrin: *Entwicklung eines ökologisch-ökonomischen Vernetzungsmodells für Wasserkraftanlagen und Mehrzweckspeicher*, 2018, ISBN 978-3-942036-61-0
- 258 Schmidt, Holger: *Microbial stabilization of lotic fine sediments*, 2018, ISBN 978-3-942036-62-7
- 259 Fetzer, Thomas: *Coupled Free and Porous-Medium Flow Processes Affected by Turbulence and Roughness – Models, Concepts and Analysis*, 2018, ISBN 978-3-942036-63-4
- 260 Schröder, Hans Christoph: *Large-scale High Head Pico Hydropower Potential Assessment*, 2018, ISBN 978-3-942036-64-1
- 261 Bode, Felix: *Early-Warning Monitoring Systems for Improved Drinking Water Resource Protection*, 2018, ISBN 978-3-942036-65-8

- 262 Gebler, Tobias: *Statistische Auswertung von simulierten Talsperrenüberwachungsdaten zur Identifikation von Schadensprozessen an Gewichtsstaumauern*, 2018, ISBN 978-3-942036-66-5
- 263 Harten, Matthias von: *Analyse des Zuppinger-Wasserrades – Hydraulische Optimierungen unter Berücksichtigung ökologischer Aspekte*, 2018, ISBN 978-3-942036-67-2
- 264 Yan, Jieru: *Nonlinear estimation of short time precipitation using weather radar and surface observations*, 2018, ISBN 978-3-942036-68-9
- 265 Beck, Martin: *Conceptual approaches for the analysis of coupled hydraulic and geomechanical processes*, 2019, ISBN 978-3-942036-69-6
- 266 Haas, Jannik: *Optimal planning of hydropower and energy storage technologies for fully renewable power systems*, 2019, ISBN 978-3-942036-70-2
- 267 Schneider, Martin: *Nonlinear Finite Volume Schemes for Complex Flow Processes and Challenging Grids*, 2019, ISBN 978-3-942036-71-9
- 268 Most, Sebastian Christopher: *Analysis and Simulation of Anomalous Transport in Porous Media*, 2019, ISBN 978-3-942036-72-6
- 269 Buchta, Rocco: *Entwicklung eines Ziel- und Bewertungssystems zur Schaffung nachhaltiger naturnaher Strukturen in großen sandgeprägten Flüssen des norddeutschen Tieflandes*, 2019, ISBN 978-3-942036-73-3
- 270 Thom, Moritz: *Towards a Better Understanding of the Biostabilization Mechanisms of Sediment Beds*, 2019, ISBN 978-3-942036-74-0
- 271 Stolz, Daniel: *Die Nullspannungstemperatur in Gewichtsstaumauern unter Berücksichtigung der Festigkeitsentwicklung des Betons*, 2019, ISBN 978-3-942036-75-7
- 272 Rodriguez Pretelin, Abelardo: *Integrating transient flow conditions into groundwater well protection*, 2020, ISBN: 978-3-942036-76-4
- 273 Weishaupt, Kilian: *Model Concepts for Coupling Free Flow with Porous Medium Flow at the Pore-Network Scale: From Single-Phase Flow to Compositional Non-Isothermal Two-Phase Flow*, 2020, ISBN: 978-3-942036-77-1
- 274 Koch, Timo: *Mixed-dimension models for flow and transport processes in porous media with embedded tubular network systems*, 2020, ISBN: 978-3-942036-78-8
- 275 Gläser, Dennis: *Discrete fracture modeling of multi-phase flow and deformation in fractured poroelastic media*, 2020, ISBN: 978-3-942036-79-5
- 276 Seitz, Lydia: *Development of new methods to apply a multi-parameter approach – A first step towards the determination of colmation*, 2020, ISBN: 978-3-942036-80-1
- 277 Ebrahim Bakhshipour, Amin: *Optimizing hybrid decentralized systems for sustainable urban drainage infrastructures planning*, 2021, ISBN: 978-3-942036-81-8
- 278 Seitz, Gabriele: *Modeling Fixed-Bed Reactors for Thermochemical Heat Storage with the Reaction System $\text{CaO}/\text{Ca}(\text{OH})_2$* , 2021, ISBN: 978-3-942036-82-5
- 279 Emmert, Simon: *Developing and Calibrating a Numerical Model for Microbially Enhanced Coal-Bed Methane Production*, 2021, ISBN: 978-3-942036-83-2
- 280 Heck, Katharina Klara: *Modelling and analysis of multicomponent transport at the interface between free- and porous-medium flow - influenced by radiation and roughness*, 2021, ISBN: 978-3-942036-84-9
- 281 Ackermann, Sina: *A multi-scale approach for drop/porous-medium interaction*, 2021, ISBN: 978-3-942036-85-6